Magdalena Sallinger, BSc

Slope stability analysis by means of strength reduction technique

MASTER'S THESIS

to achieve the university degree of

Diplom-Ingenieurin

Master's degree programme: Civil Engineering Sciences, Geotechnics and Hydraulics

submitted to

Graz University of Technology

Supervisor

Ass.Prof. Dipl.-Ing. Dr.techn., Franz Tschuchnigg

Institute of Soil Mechanics and Foundation Engineering

Graz, June 2017

Eidesstattliche Erklärung

Ich erkläre an Eides statt, dass ich die vorliegende Arbeit selbstständig verfasst, andere als die angegebenen Quellen/Hilfsmittel nicht benutzt, und die den benutzten Quellen wörtlich und inhaltlich entnommenen Stellen als solche kenntlich gemacht habe.

Graz, am …… ……

(Unterschrift)

Statutory declaration

I declare that I have authored this thesis independently, that I have not used other than the declared sources / resources, and that I have explicitly marked all material which has been quoted either literally or by content from the used sources.

Graz, …… ……

(signature)

Danksagung

An dieser Stelle möchte ich ganz besonders Ass.Prof. Dipl.-Ing. Dr.techn. Franz Tschuchnigg für die außerordentliche Betreuung danken. Dessen Begeisterung für die Thematik, als auch die aufschlussreichen Besprechungen motivierte mich stets aufs Neue. Ein Dank gilt auch Prof. Dr.-Ing. Thomas Benz, mit dessen Unterstützung eine vollständige Bearbeitung der Aufgabenstellung erst möglich wurde.

Bedanken möchte ich mich auch bei meinen Kollegen im „Kammerl“, die immer ein offenes Ohr hatten und für abwechslungsreiche Stunden sorgten. Herzlich danken möchte ich auch allen Freunden aus dem Zeichensaal – speziell bei Elli und July. Durch euch wurde das Studium zu einer unvergesslichen Zeit.

Vor allen Dingen möchte ich mich bei meinen Eltern und meiner Schwester bedanken. Danke, dass ihr mich in diesen Jahren so unterstützt habt. Abschließend möchte ich mich noch bei meinem Freund Robert, für die Korrektur und die aufbauenden Worte während dieser Zeit, bedanken. Es ist unglaublich schön jemanden wie dich an seiner Seite zu haben.

Kurzfassung

In der Geotechnik ist die Anwendung des Bruchkriteriums nach Mohr-Coulomb zur Untersuchung der Böschungsstabilität fest etabliert. Jedoch vernachlässigt dieses die mittlere Hauptnormalspannung und führt unter Umständen zu einer konservativen Lösung hinsichtlich des Sicherheitsfaktors. Diese Arbeit untersucht zum einen den Effekt des Bruchkriteriums nach Matsuoka-Nakai auf den Sicherheitsfaktor. Zum anderen werden der Spannungspfade der unterschiedlichen Bruchkriterien im dreidimensionalen Hauptspannungsraum miteinander verglichen. Es wurden mehrere Modelle in einer Displacement-Finite-Element-Analyse untersucht. Das Ergebnis des Sicherheitsfaktors wie auch der Spannungspfad unterscheidet sich signifikant zwischen diesen Bruchkriterien.

Abstract

Slope stability analyses in geotechnical engineering are generally based on a Mohr-Coulomb failure criterion. However, this model neglects the intermediate principal stress and leads in some circumstances to conservative results related to the factor of safety. This thesis on the one hand investigates the failure criterion according to Matsuoka-Nakai and its effect on the factor of safety by means of strength reduction. And on the other hand compares the stress paths obtained with the different failure criteria. A number of different models are studied using displacement finite-element analyses. The resulted factors of safety, as well as the obtained stress paths, differ significantly between the investigated failure criteria.

Table of contents

List of figures

List of tables

List of symbols and abbreviations

Capital letters

B	[-]	Skempton coefficient
C	[-]	triaxial compression point
E	[-]	triaxial extension point
E	[kN]	load due to the surrounding soil
E'	[kN/m²]	Young´s modulus
E_{50}^{ref}	[kN/m²]	reference secant stiffness in triaxial test
E_{oed}	[kN/m²]	Oedometer modulus
E_{oed}^{ref}	[kN/m²]	reference tangent stiffness for primary oedometer loading
E_{ur}^{ref}	[kN/m²]	reference un- / reloading stiffness
G	[kN]	gravity load of the soil
G	[kN/m²]	shear modulus
G_0^{ref}	[kN/m²]	reference un- / reloading stiffness
G_0/G_{ur}	[-]	ratio of shear moduli
$G_{\perp}$	[kN]	stabilizing force of the gravity load
$G_{//}$	[kN]	destabilizing force of the gravity load
H	[m]	height
I_1, I_2, I_3	[kN/m²]	effective stress invariants
J_1, J_2, J_3	[kN/m²]	deviatoric stress invariants
K_0	[-]	earth pressure coefficient at rest
K_0^{nc}	[-]	coefficient of lateral earth pressure for normally consolidated stress state
K_{MN}	[-]	material coefficient
L	[m]	length
M1	[-]	material set 1
M2	[-]	material set 2
M_{sf}	[-]	incremental multiplier
N	[kN]	normal force
Q	[kN]	reaction force
R	[kN]	resistance force
R_f	[-]	failure ratio
T	[kN]	horizontal force

Small letters

b	[-]	parameter of stress state
c'	[kN/m²]	effective cohesion
c'_c	[kN/m²]	cohesion at triaxial compression
c'_e	[kN/m²]	cohesion at triaxial extension
c_{input}	[kN/m²]	input value of cohesion
c_{limit}	[kN/m²]	cohesion at failure or limiting cohesion
e_c	[-]	critical void ratio
f	[-]	yield function
g	[-]	plastic potential
m	[-]	power for stress-level dependency of stiffness
p'	[kN/m²]	principal isotropic effective stress
p_{max}	[kN/m²]	maximum principal isotropic effective stress
p_{ref}	[kN/m²]	reference stress of stiffness
p_v	[kN/m²]	vertical stress on the sliding surface
q'	[kN/m²]	principal deviatoric effective stress
q_{MC}	[kN/m²]	deviatoric stress at the Mohr-Coulomb yield surface
q_{MN}	[kN/m²]	deviatoric stress at the Matsuoka-Nakai yield surface
r_e	[-]	relative element size factor
s	[kN/m²]	diameter of Mohr circle
t	[kN/m²]	radius of Mohr circle

Greek letters

β	[°]	slope inclination
γ	[%]	shear strain
$\gamma_{0.7}$	[%]	Treshold shear strain
γ_{xy}	[%]	Cartesian shear strain
Δl	[m]	distance
Δl_{MC}	[m]	distance in Mohr-Coulomb computation
Δl_{MN}	[m]	distance in Matsuoka-Nakai computation
Δq	[%]	normalised principal deviatoric stress deviation
ε_1	[%]	axial strain
ε_2	[%]	lateral strain
ε_3	[%]	lateral strain
$\dot{\varepsilon}_d^{pl}$	[s^{-1}]	plastic deviatoric strain rate
ε_{tol}	[%]	tolerated error

$\dot{\varepsilon}_v^{pl}$	[s^{-1}]	plastic volumetric strain rate
ε_{xx}, ε_{yy}, ε_{zz}	[%]	Cartesian strain rates
θ	[°]	lode angle
ν	[-]	Poisson´s ratio
ν_{ur}	[-]	Poisson´s ratio for un- / reloading
$\sum M_{sf}$	[-]	factor of safety
σ_0'	[kN/m²]	effective bonding stress
σ_1'	[kN/m²]	major effective principal stress
σ_2'	[kN/m²]	intermediate effective principal stress
σ_3'	[kN/m²]	minor effective principal stress
σ_f'	[kN/m²]	effective normal stress at failure
σ_m'	[kN/m²]	effective mean stress
σ_n'	[kN/m²]	effective normal stress
σ_t	[kN/m²]	tensile strength
σ_{xx}, σ_{yy}, σ_{zz}	[kN/m²]	Cartesian stress
τ_f'	[kN/m²]	effective shear strength
τ_{max}	[kN/m²]	maximum shear stress
ϕ	[°]	Coulomb friction angle
φ'	[°]	effective friction angle
φ_c'	[°]	effective friction angle at triaxial compression
φ_{cv}	[°]	friction angle at constant volume or critical friction angle
φ^{ds}	[°]	direct shear angle of friction
φ_e'	[°]	effective friction angle at triaxial extension
φ_f, φ_{limit}	[°]	friction angle at failure or limiting angle of friction
φ_{input}	[°]	input value of friction angle
φ_{mc}'	[°]	effective equivalent Mohr-Coulomb friction angle
φ_p	[°]	peak friction angle
φ^{ps}	[°]	plane strain angle of friction
φ_{res}	[°]	residual friction angle
φ^{tr}	[°]	friction angle at triaxial compression
ψ'	[°]	effective dilatancy angle
ψ_{input}	[°]	input value of dilatancy angle
ψ_{limit}	[°]	dilatancy angle at failure or limiting angle of dilatancy

Abbreviations

CD	Consolidated Drained
CU	Consolidated Undrained
DEM	Discrete Element Method
DSB	Direct Shear Box test
DSS	Direct Simple Shear test
E-MN	Extended Matsuoka-Nakai failure criterion
FEA	Finite Element Analysis
FoS	Factor of Safety
GHS	Generalised Hardening Soil model
GR	Gravity loading
HS	Hardening Soil model
HSS	Hardening Soil with Small-strain stiffness
LE	Linear Elastic model
LEM	Limit Equilibrium Method
M	Material model
MC	Mohr-Coulomb failure criterion
MN	Matsuoka-Nakai failure criterion
SMP	Spatially Mobilised Plane
SP	Stress Point
SRFEA	Strength Reduction Finite Element Analysis
STD	Standard implementation
UU	Unconsolidated Undrained

1 Introduction

In geotechnical engineering a precise prediction about slope stability and the related factor of safety is essential. A common practice to obtain the ultimate limit state is the so called *limit equilibrium method* (LEM) by means of the method of slices. There the factor of safety is obtained with the ratio between resisting forces and driving forces.

The method of slices applied on a cohesionless infinite slope is a quite simple and mechanically clear method. However, it is shown in [1] and [2], that sometimes this method overpredicts the FoS in slope stability analysis.

An approach which considers dilatancy effects (in combination with a Mohr-Coulomb failure criterion) is proposed by [3]. However, this approach leads to conservative results related to the FoS, due to the neglect of the intermediate effective principal stress σ_2'. For this reason, an advanced failure criterion according to Matsuoka-Nakai is introduced by [4].

In previous studies [5] those approaches are based on the assumption of cohesionless infinite slopes. It is of interest to investigate the factor of safety once a homogeneous finite slope is considered. The present thesis studies the effect of two separate failure criteria on the slope stability analysis by means of strength reduction. But also on the development of the stress path. Therefore the finite-element code Plaxis [6] is used for all calculations.

The divergences in the slope inclination at failure are compared using analytical results and a displacement finite-element analysis. Furthermore, the stress paths of slope stability analyses are generated in a three-dimensional principal effective stress space. The findings should clarify the development of stresses during the calculation and should reveal the importance of an appropriate failure criterion.

The following chapter introduces briefly some theories related to failure criteria. There, the *effective stresses* σ' are labelled accordingly. But, due to the fact that in the subsequent chapters no water table is defined, this labelling has been deliberately abandoned. Hence, the *effective stresses* σ' are equal to the *total stresses* σ.

2 Linear elastic-perfectly plastic models

Conventional analyses isolate serviceability from ultimate limit state, where the former relates to stiffness parameters and the latter refers to strength parameters. When dealing with advanced numerical methods the soil is described by means of a constitutive model. This constitutive model is also called material model and provides the required connection between stresses and strains.

An elastic-perfectly plastic constitutive model simplifies the stress-strain behaviour. Real soil characteristics such as hardening and softening are neglected and replaced by two straight lines, reflecting the elastic and plastic region (see Fig. 1). The transition from elastic to plastic behaviour is characterised by the yield function *f*, this differs depending on the material model. An ideal soil (linear elastic-perfectly plastic) shows a linear elastic behaviour until the yield stress is reached. This means a reversible behaviour for unloading. In the elastic region the yield function is given by $f < 0$. If $f = 0$, irreversible plastic deformation occur at a constant stress value which describes a perfectly plastic material. In other words, $f = 0$ defines the stress point hitting the yield surface. At this point a plastic stress state is reached and no further stress increment can be maintained. Consequently, stress redistribution takes place. The direction of the plastic strain increment at this point is controlled by the flow rule as explained later on. It should be mentioned, that a stress state outside the yield surface is not admissible and therefore f > 0 does not exist.

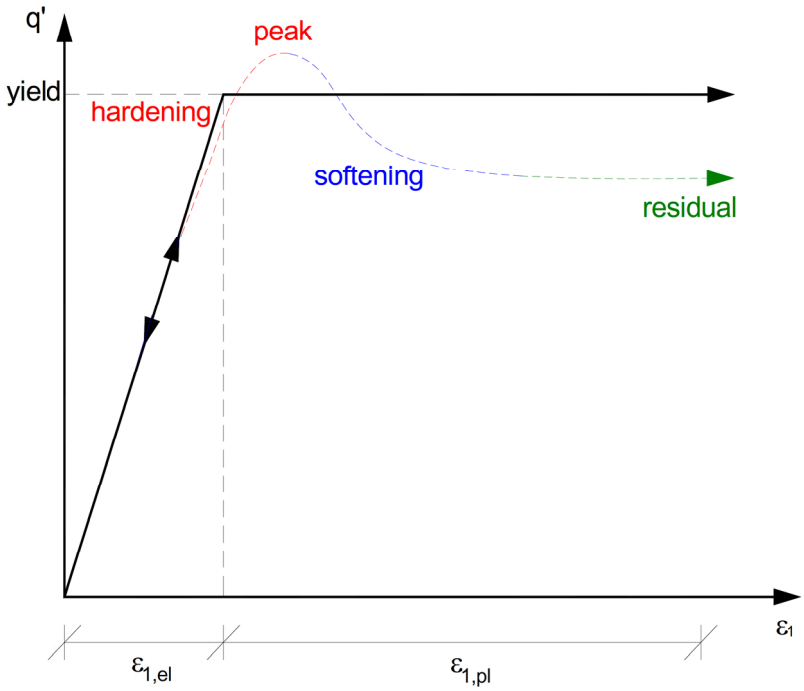

Fig. 1 Linear elastic-perfectly plastic material

2.1 Flow rule

According to the plasticity theory introduced by Hill [7] the direction of plastic strain increment corresponds to the first derivative of the yield function. Consequently, the flow rule is assumed to be associated where the plastic strain increment is perpendicular to the yield function. In other words, an associated flow rule uses a *dilatancy angle* ψ' equal to the *friction angle* φ'. It is shown in literature [8], that this leads to an overestimation of the plastic volumetric strain rate. For granular normally consolidated soil at shallow stress points the dilatancy angle tends to be very small. In principle, the dilatancy angle strongly depends on soil density and friction angle. With increasing depth and therefore increasing density the dilatancy angle decreases. A detailed discussion about dilatancy angle and its effect on slope stability is covered in chapter **Fehler! Verweisquelle konnte nicht gefunden werden.**.

Due to the fact that $\varphi' \neq \psi'$, a *plastic potential g* is introduced. This governs the effect of the dilatancy, which in turn influences the direction of the plastic strain increment. Consequently a non-associated flow rule is given by $g \neq f$.

The approach of flow rule require in general coaxiality between principal stress and strain rate [9]. The plastic strain rate vector can be divided in a *plastic deviatoric strain rate* $\dot{\varepsilon}_d^{pl}$ and a *plastic volumetric strain rate* $\dot{\varepsilon}_v^{pl}$. Fig. 2 shows the difference between associated and non-associated flow rule. Note the overrated *plastic volumetric strain rate* $\dot{\varepsilon}_v^{pl}$ for associated flow rule (left).

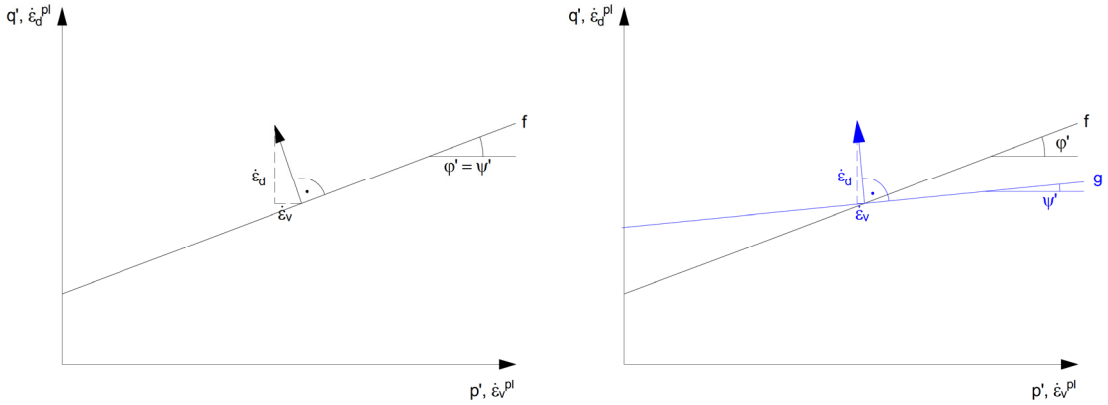

Fig. 2 Flow rule (left: associated; right: non-associated)

A variety of failure criteria have been developed but only two of them were used in this thesis for the numerical stability analysis. The well-known Mohr-Coulomb model and the Matsuoka-Nakai model.

2.2 Mohr-Coulomb (MC)

The following content is based on [10], [11] , [12] and [13].

The most frequently applied failure criterion for soils is the well-known Mohr-Coulomb model (MC). It stands out from all other conventional failure criteria due to its simple and clear application. An easy handling is also provided through the low number of parameters.

- *Young´s modulus E'* and *Poisson´s ratio* ν are responsible for soil elasticity.
- Friction angle φ', dilatancy angle ψ' and cohesion c' are responsible for soil plasticity.

The Coulomb failure criterion characterizes the state of yielding and can be written as followed:

$$\tau_f' = \sigma_f' \cdot \tan\varphi' + c' \qquad (1)$$

If the Coulomb failure criterion is expressed in principal effective stresses associated with the Mohr´s circle of stress the reformulated Mohr-Coulomb failure criterion can be obtained:

$$(\sigma_1' - \sigma_3') = (\sigma_1' + \sigma_3') \sin\varphi' + 2c' \cos\varphi' \qquad (2)$$

Failure occurs as soon as the Mohr´s circle hits the Coulomb failure line (see Fig. 3) There, the relation $\sigma_1' > \sigma_2' > \sigma_3'$ is valid. In opposition to the usual mechanical sign convention in geotechnical engineering compression often is signed positive and extension negative as it is applied in this work too.

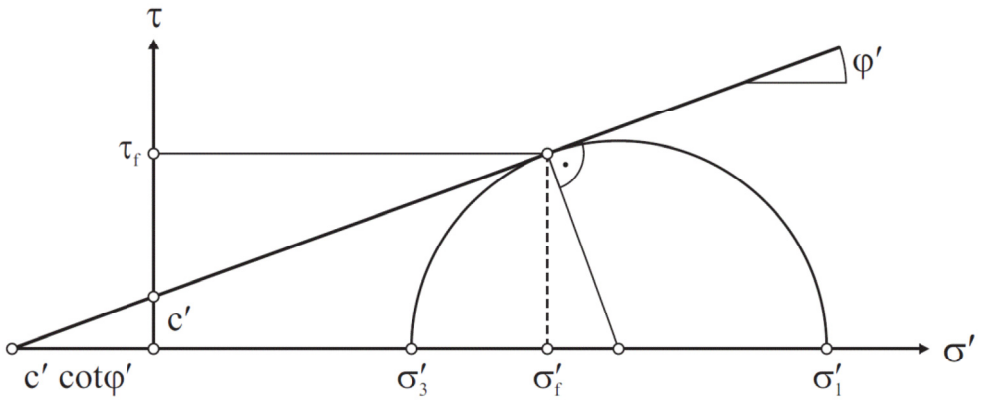

Fig. 3 Coulomb failure criterion and Mohr-Coulomb failure criterion in σ'-τ'-plane [11]

Equation (2) neglects the intermediate effective principal stress σ_2'. However, in FEA a three-dimensional principal effective stress space is considered. The general representation of the Mohr-Coulomb failure criterion is given by the six yield functions

(Equ. (3) to Equ. (8)). With these a hexagonal cone is generated as shown in Fig. 4. The right part of the figure displays a cross section through the cone (perpendicular to p'). This plane is called π-plane in literature.

$$f_a = (\sigma_1' - \sigma_3') - (\sigma_1' + \sigma_3') \sin\varphi' - 2c' \cos\varphi' \quad (3)$$

$$f_b = (\sigma_1' - \sigma_2') - (\sigma_1' + \sigma_2') \sin\varphi' - 2c' \cos\varphi' \quad (4)$$

$$f_c = (\sigma_2' - \sigma_1') - (\sigma_2' + \sigma_1') \sin\varphi' - 2c' \cos\varphi' \quad (5)$$

$$f_d = (\sigma_2' - \sigma_3') - (\sigma_2' + \sigma_3') \sin\varphi' - 2c' \cos\varphi' \quad (6)$$

$$f_e = (\sigma_3' - \sigma_2') - (\sigma_3' + \sigma_2') \sin\varphi' - 2c' \cos\varphi' \quad (7)$$

$$f_f = (\sigma_3' - \sigma_1') - (\sigma_3' + \sigma_1') \sin\varphi' - 2c' \cos\varphi' \quad (8)$$

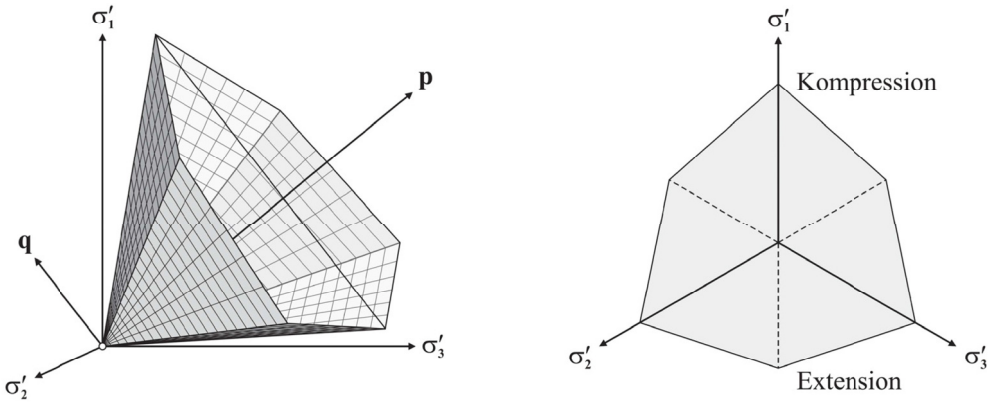

Fig. 4 MC yield function in the principal stress space for a cohesionless soil [11]

In order to describe the direction of the plastic strain increments a *plastic potential g* is defined with six equations equal to the yield functions. Except that the friction angle is substituted with the dilatancy angle as followed:

$$g_a = (\sigma_1' - \sigma_3') - (\sigma_1' + \sigma_3') \sin\psi' - 2c' \cos\psi' \quad (9)$$

$$g_b = (\sigma_1' - \sigma_2') - (\sigma_1' + \sigma_2') \sin\psi' - 2c' \cos\psi' \quad (10)$$

$$g_c = (\sigma_2' - \sigma_1') - (\sigma_2' + \sigma_1') \sin\psi' - 2c' \cos\psi' \quad (11)$$

$$g_d = (\sigma_2' - \sigma_3') - (\sigma_2' + \sigma_3') \sin\psi' - 2c' \cos\psi' \quad (12)$$

$$g_e = (\sigma_3' - \sigma_2') - (\sigma_3' + \sigma_2') \sin\psi' - 2c' \cos\psi' \quad (13)$$

$$g_f = (\sigma_3' - \sigma_1') - (\sigma_3' + \sigma_1') \sin\psi' - 2c' \cos\psi' \quad (14)$$

2.2.1 Interpretation of the stress state

As already mentioned, the failure criterion can be expressed by a Coulomb failure criterion based on the relation between shear stress and normal stress. On the other hand the failure criterion can also be described through the Mohr-Coulomb failure criterion. This failure criterion can be displayed in various ways as indicated in Fig. 5.

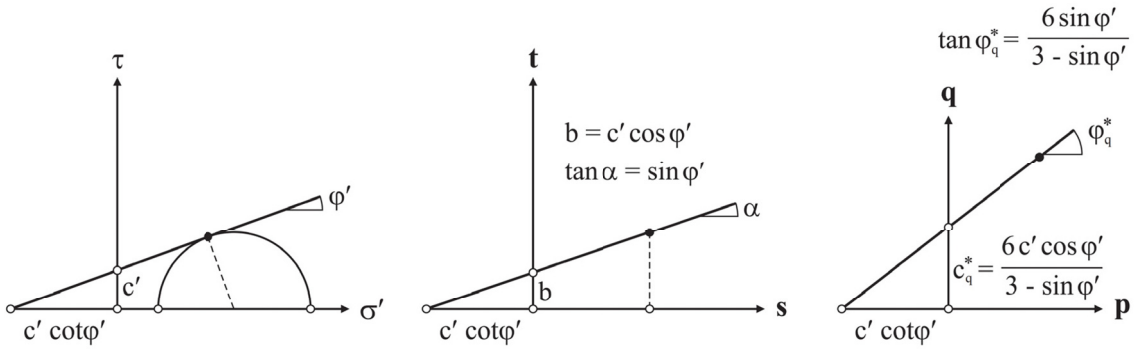

Fig. 5 Different types of presentation of the MC failure criterion [11]

The chart in the middle presents the s-t-diagram, where *s* is the center of the Mohr´s circle and *t* defines the radius of the circle.

$$s' = \frac{\sigma_1' + \sigma_3'}{2} \qquad (15)$$

$$t' = \frac{\sigma_1' - \sigma_3'}{2} \qquad (16)$$

The third chart plots the *principal isotropic effective stress p'* versus the *principal deviatoric effective stress q'* with:

$$p' = \sigma_m' = \frac{(\sigma_1' + \sigma_2' + \sigma_3')}{3} \qquad (17)$$

$$q' = \sqrt{\frac{(\sigma_1' - \sigma_2')^2 + (\sigma_2' - \sigma_3')^2 + (\sigma_3' - \sigma_1')^2}{2} + 3(\sigma_{12}^2 + \sigma_{23}^2 + \sigma_{31}^2)} \qquad (18)$$

In case of a triaxial stress state the above equation reduces to:

$$p' = \frac{(\sigma_1' + 2\sigma_3')}{3} \qquad (19)$$

$$q' = \sigma_1' - \sigma_3' \qquad (20)$$

2.2.2 Principal effective stress space

In FEA a three-dimensional principal effective stress state is considered. Therefore, it is advantageous to display the yield criterion in a principal stress space by means of a p-q-diagram (see Fig. 5). There the principal isotropic effective stress axes builds the space diagonal of the three-dimensional cone (see also Fig. 4). The magnitude of p' measures the distances between origin and current deviatoric plane along the space diagonal. The deviatoric plane named π-plane is perpendicular to the space diagonal and its shape is controlled by the yield function. The *triaxial compression point C* as well as the *triaxial extension point E* determine the cone opening. In order to clarify the following mathematical relation a graphic illustration for cohesionless soils is presented in Fig. 6.

For cohesionless soils the magnitude of triaxial compression / extension at a specific stress state is:

$$\frac{q'}{p'} = \tan\varphi'_c \rightarrow a_c = p' \tan\varphi'_c = p' \frac{6\sin\varphi'}{3-\sin\varphi'} \qquad (21)$$

$$\frac{q'}{p'} = \tan\varphi'_e \rightarrow a_e = p' \tan\varphi'_e = p' \frac{6\sin\varphi'}{3+\sin\varphi'} \qquad (22)$$

For cohesive soils Equ. (21) and (22) extends to:

$$a_c = p' \tan\varphi'_c + c'_c \qquad (23)$$

$$a_e = p' \tan\varphi'_e + c'_e \qquad (24)$$

with:

$$c_c = \frac{6c'\cos\varphi'}{3-\sin\varphi'} \qquad (25)$$

$$c_e = \frac{6c'\cos\varphi'}{3+\sin\varphi'} \qquad (26)$$

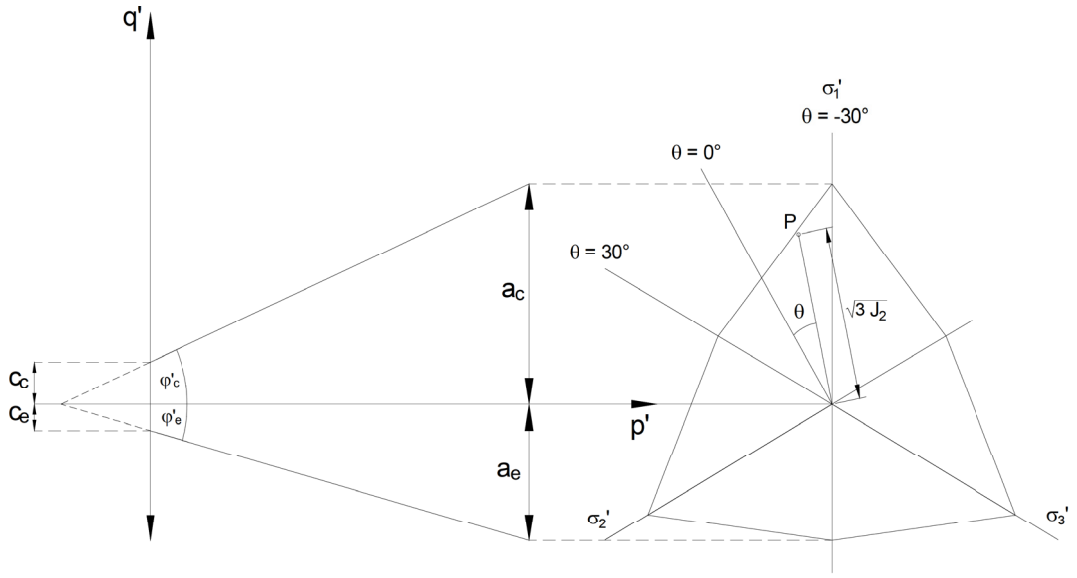

Fig. 6 MC failure criterion in principal effective stress space for cohesionless soil

Furthermore the location of an arbitrary stress state *P* in the deviatoric plane can be determined with the help of invariants. The use of invariants provides independency of the chosen coordinate system. Besides the isotropic effective stress p' the second and third deviatoric stress invariants are necessary to define a stress state in the principal stress space. For completeness the first deviatoric stress invariant is listed in the following (Equ. (27), (28) and (29)).

$$J_1 = (\sigma_1' - \sigma_m') + (\sigma_2' - \sigma_m') + (\sigma_3' - \sigma_m') = 0 \qquad (27)$$

$$J_2 = \frac{1}{6}[(\sigma_1' - \sigma_2')^2 + (\sigma_2' - \sigma_3')^2 + (\sigma_3' - \sigma_1')^2] \qquad (28)$$

$$J_3 = (\sigma_1' - \sigma_m')(\sigma_2' - \sigma_m')(\sigma_3' - \sigma_m') \qquad (29)$$

The distance of a stress state perpendicular from the space diagonal is derived by $\sqrt{3 \cdot J_2}$, whereas the orientation within the deviatoric plane is given by the *lode angle θ* which is formulated as:

$$\theta = \frac{1}{3}\sin^{-1}\left(-\frac{\sqrt{27}}{2} \cdot \frac{J_3}{\sqrt{J_2{}^3}}\right) \qquad (30)$$

Now the stress state *P* is fully determined by means of p', $\sqrt{3 \cdot J_2}$ and θ (see Fig. 6). It has to be noted that the lode angle ranges between -30° and +30°. Where $\theta = -30°$ corresponds to triaxial compression (Point *C*: $\sigma_1' \geq \sigma_2' = \sigma_3'$) and $\theta = +30°$ to triaxial extension (Point *E*: $\sigma_1' = \sigma_2' \geq \sigma_3'$).

2.3 Matsuoka-Nakai (MN)

This chapter relates to a number of sources, notably: [14], [15], [16] and [4]

Unlike the Mohr-Coulomb material model Matsuoka-Nakai considers also the intermediate principal stress σ_2' (stress plane is named s*patially mobilised plane* SMP). Theoretically, three different principal stresses lead to three possible Mohr´s stress circles, namely between $\sigma_1' > \sigma_2'$; $\sigma_2' > \sigma_3'$ and $\sigma_1' > \sigma_3'$ [17]. Each of them create a mobilised plane which indicates the onset of yielding. Note, the Mohr-Coulomb criterion only takes the Mohr´s stress circle $\sigma_1' > \sigma_3'$ into account.

The application of the SMP enables a unique interpretation of the stress-strain relation at yielding under three different principal stresses [4]. Additionally, the yield condition is formulated in such a way that yielding occurs at a point where the shear-normal stress ratio on the SMP reaches a certain value. The yield condition according to Matsuoka-Nakai computed in the π-plane circumscribes the hexagon of the Mohr-Coulomb criterion in a cubic way. At all corners of the π-plane, the yield surface of Matsuoka-Nakai is identical with the Mohr-Coulomb which is illustrated in Fig. 7.

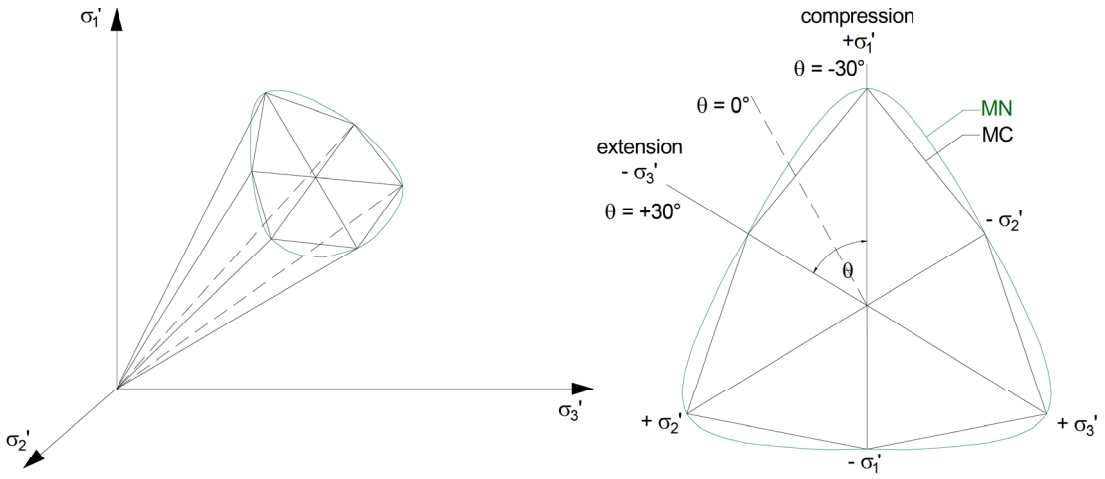

Fig. 7 Matsuoka-Nakai criterion in three-dimensional principal effective stress space and π-plane.

2.3.1 Cohesionless frictional soil

At first the derivation of the yield surface for purely frictional (cohesionless) soils is explained. The content of this chapter is based on [15]. Subsequently the equations for cohesive soils are presented.

Generally, the yield criterion based on Matsuoka-Nakai can be formulated as followed:

$$K_{MN} = \frac{I_1 I_2}{I_3} = \frac{9 - \sin^2 \varphi'^{tr}}{1 - \sin^2 \varphi'^{tr}} \quad (31)$$

Where I_1, I_2 and I_3 are the first, second and third effective stress invariants, which are computed with:

$$I_1 = \sigma_1' + \sigma_2' + \sigma_3' \quad (32)$$

$$I_2 = \sigma_1'\sigma_2' + \sigma_2'\sigma_3' + \sigma_1'\sigma_3' \quad (33)$$

$$I_3 = \sigma_1'\sigma_2'\sigma_3' \quad (34)$$

And φ'^{tr} stands for the friction angle measured in a triaxial compression test.

Accordingly the corresponding yield function forms to:

$$f = I_1 I_2 - I_3 K_{MN} \quad (35)$$

An issue of this thesis has been to compute the yield surface for the three-dimensional principal effective stress space with Mohr-Coulomb, as well as with Matsuoka-Nakai. For the first studies, attention has been paid on cohesionless soils only. Hence, below listed calculation steps are exclusively valid for cohesionless soils and were implemented in MS Excel.

As introduced in [15] the Matsuoka-Nakai yield surface can be expressed in terms of an *equivalent Mohr-Coulomb friction angle* φ_{mc}' outlined by Equ. (36). This angle of friction defines the intersection point with the Mohr-Coulomb surface for a certain stress state and varies with the orientation in the π-plane. Applied to any lode angle between -30°and +30° a smooth curve reflecting the Matsuoka-Nakai yield surface is obtained.

The *equivalent friction angle* φ_{mc}' is given by:

$$\varphi_{mc}' = 2\tan^{-1}\left(\sqrt{R}\right) - \frac{1}{2}\pi \quad (36)$$

In order to calculate φ_{mc}' the formulation of a cubic equation:

$$a_0 + a_1 R + a_2 R^2 + a_3 R^3 = 0 \quad (37)$$

has to be solved for *R*.

The corresponding coefficients are composed of:

$$a_0 = 3 + 4\sqrt{3}\tan\theta + 3\tan^2\theta \quad (38)$$

$$a_1 = (15 - 2K_{MN}) - 2\sqrt{3}(K_{MN} - 3)\tan\theta - 3\tan^2\theta \quad (39)$$

$$a_2 = (15 - 2K_{MN}) + 2\sqrt{3}(K_{MN} - 3)\tan\theta - 3\tan^2\theta \quad (40)$$

$$a_3 = 3 - 4\sqrt{3}\tan\theta + 3\tan^2\theta \quad (41)$$

with K_{MN} related to Equ. (31).

2.3.2 Cohesive frictional soil

Secondly the Matsuoka-Nakai failure criterion has been applied on cohesive soils, which then is called extended Matsuoka-Nakai (E-MN). The derivation of the equivalent friction angle φ'_{mc} is not as simple as above. The cohesion already has to be taken into account at the material coefficient K_{MN}. However, Griffiths and Huang [16] suggest a method to consider cohesion as follows:

$$K_{MN} = \frac{9 - \sin^2\varphi'^{tr}}{1 - \sin^2\varphi'^{tr}} = \frac{[(\sigma'_1 + \sigma'_0)(\sigma'_2 + \sigma'_0) + (\sigma'_2 + \sigma'_0)(\sigma'_3 + \sigma'_0) + (\sigma'_1 + \sigma'_0)(\sigma'_3 + \sigma'_0)]}{(\sigma'_1 + \sigma'_0)(\sigma'_2 + \sigma'_0)(\sigma'_3 + \sigma'_0)} \quad (42)$$

where:

$$\sigma'_0 = -c' \cot\varphi'_{mc} \quad (43)$$

For further calculations it is necessary to substitute the terms of Equ. (42) with:

$$(\sigma'_1 + \sigma'_0) = \left(\frac{\sigma'_1}{\sigma'_3} + \frac{c' \cot\varphi'^{tr}}{\sigma'_3}\right) \quad (44)$$

$$(\sigma'_2 + \sigma'_0) = \left(\frac{b\sigma'_1}{\sigma'_3} + 1 - b + \frac{c' \cot\varphi'^{tr}}{\sigma'_3}\right) \quad (45)$$

$$(\sigma'_3 + \sigma'_0) = \left(1 + \frac{c' \cot\varphi'^{tr}}{\sigma'_3}\right) \quad (46)$$

Note, the equations above (Equ. (44), (45) and (46)) differs from the literature [16], due to the difference in the sign convention.

Now the material coefficient K_{MN} only depends on the parameters σ_3', c', φ'^{tr} and b. As well as the lode angle parameter b defined by Bishop [18]. This parameter opposes the three principal effective stresses relatively and varies between zero and one with:

$$b = \frac{(\sigma_2' - \sigma_3')}{(\sigma_1' - \sigma_3')} \tag{47}$$

$b = 0$ leads to triaxial compression which relates to a lode angle of $\theta = -30°$ and $b = 1$ belongs to triaxial extension with $\theta = +30°$. Equ (47) can be also formulated as a function of θ with:

$$b = \frac{\sqrt{3}\tan\theta + 1}{2} \tag{48}$$

If the values σ_3', c', φ'^{tr} are given only the related σ_1' has to be obtained in order to create the yield surface based on Matsuoka-Nakai. Thereby Equ. (48) is used in Equ. (45) and Equ. (44 - 46) is substituted in Equ. (42), which then is solved for σ_1'. Finally the equivalent friction angle φ_{mc}' can be calculated for each lode angle ($-30° \leq \theta \leq +30°$) with:

$$\varphi_{mc}' = 2\tan^{-1}\left(\frac{-c' + \sqrt{c'^2 + \sigma_1'\sigma_3'}}{\sigma_3'}\right) - \frac{1}{2}\pi \tag{49}$$

The friction angle based on the Mohr-Coulomb failure criterion is assumed to be constant rather than dependent on the lode angle. On the contrary, the Matsuoka-Nakai failure criterion varies the friction angle dependently from the lode angle. Moreover, the cohesion affects the shape of the MN yield surface and thus also the equivalent friction angle φ_{mc}'. The introduced formulas are verified with an example, presented in the literature [16] based on a friction angle $\varphi' = 30°$ and displayed in Fig. 8. There the equivalent friction angle is dependent on the ratio of c'/σ_3'. The plotted curves belong to ratios of $c' = 0$, $c'/\sigma_3' = 0.1$, 1, 10 and $\sigma_3' = 0$. For this reason the cohesion was kept constant with $c' = 10$ kN/m² except of the first case, where $c' = 0$ kN/m². It can be seen that the generated curves (coloured) perfectly agree with the predicted curves (black in the background) reported in the literature.

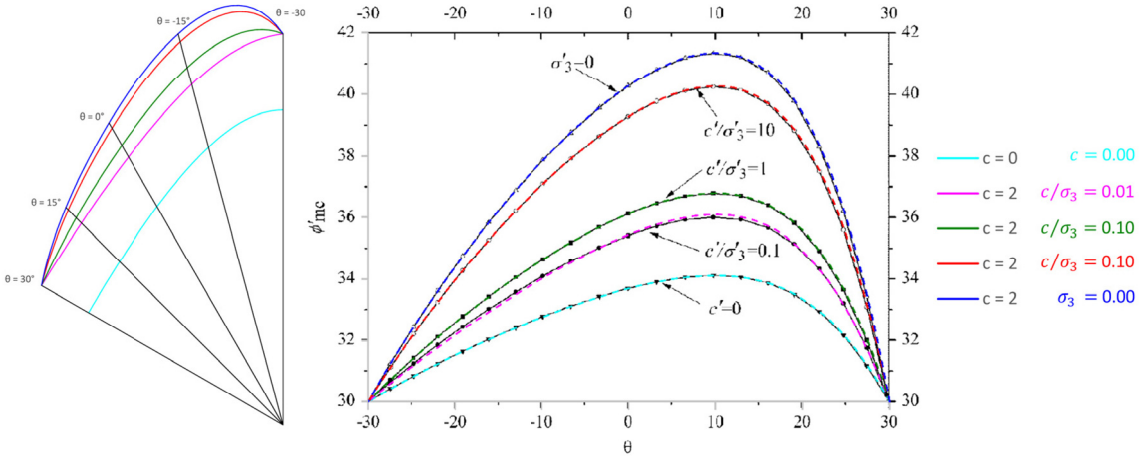

Fig. 8 Comparison of the equivalent friction angle with literature [16]

However, it has not been possible to provide a reasonable φ'_{mc} with stress states based on arbitrary chosen stress points of a slope computed in FEA. This problem is discussed in Appendix A.

Fig. 9 displays the MN yield surfaces (derived by the modified equation proposed in Appendix A) at different values of cohesion and a corresponding friction angle of 25°. Further illustrations including selected friction angles between 20° and 45° are reported in Appendix B.

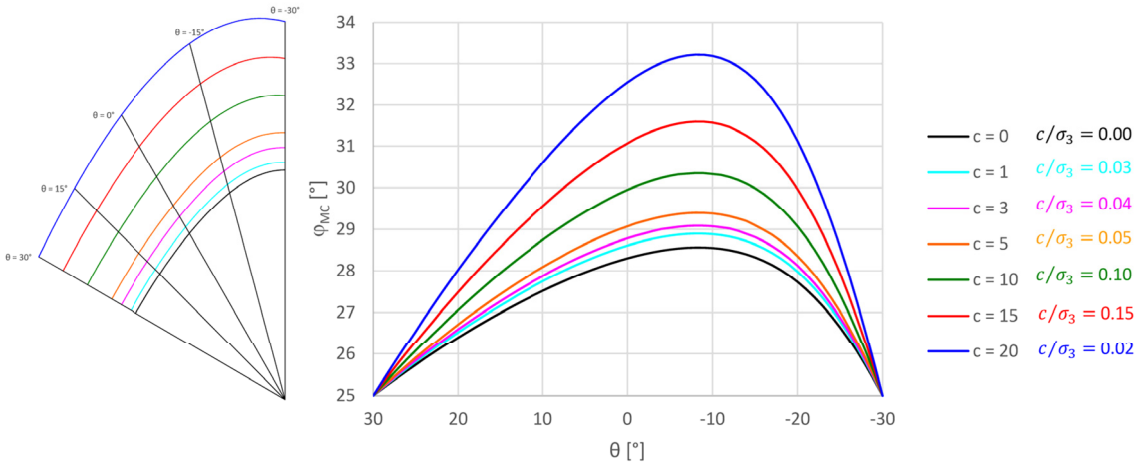

Fig. 9 Determination of φ'_{mc}. for varying cohesion at $\varphi' = 25°$

2.4 Shortcomings

Material models are an approximation of real soil behaviour. Simple failure criteria based on linear elastic-perfectly plastic material behaviour entail some shortcomings such as:

- Real soil behaviour (related to stress-strain relation) is restricted. Hardening effects in form of plastic strains below the yield surface are neglected as well as softening effects after the peak value. This could lead to serious consequences.

- Overestimation of dilatancy if an associated flow rule is applied. This can be solved by using a non-associated flow rule. Unfortunately a non-associated plasticity can cause numerical instabilities in finite-element analysis. For detailed explanation see chapter 4.1.1. Furthermore, the plastic potential with Matsuoka-Nakai cannot be derived as easy as with Mohr-Coulomb. Due to the non-linearity of the failure criterion a substitution of the friction angle with the dilatancy angle is not possible [19].
- Influencing parameters like void ratio are excluded. Furthermore the friction angel is kept constant over depth. In truth it is highly stress dependent and so a constant friction angle can be problematic in some circumstances.
- The stiffness modulus is independent of the stress level but an “averaged” constant. Moreover, a linear elastic-perfectly plastic material assumes a un- / reloading stiffness equal to the primary loading stiffness. For soils this is not a realistic behaviour. In fact the stiffness depends on the stress level, the stress path and the strain level. Besides, all listed material models above are based on the assumption of isotropic material behaviour. That means the stiffness is independent of direction.
- Failure surface is not affected by plastic strains and therefore fixed in space.

Despite these shortcomings it has to be pointed out, that the linear elastic-perfectly plastic material model is still appropriate for certain boundary value problems. But a non-associated flow rule has to be considered! Due to the manageable input parameters it is commonly used in daily engineering practice.

3 Soil Tests to obtain the effective friction angle

This chapter provides a rough overview about common soil tests to determine the friction angle. In some literature [20], [21] or [22] it is investigated that the results of the soil tests differ from each other. Due to differences in boundary conditions and measurement conditions. In the following, the labelling of the effective stresses has been deliberately renounced.

3.1 Interpretation of friction angle

The following chapter is focused on the distinction and definition of friction angles. Since strength properties are the key parameters for calculating the factor of safety, the friction angle should be selected carefully.

Generally, the friction angle is distinguished in a peak, critical state and residual state value. Fig. 10 demonstrates the ratio between these friction angles with:

$$\varphi_p > \varphi_{cv} > \varphi_{res} \qquad (50)$$

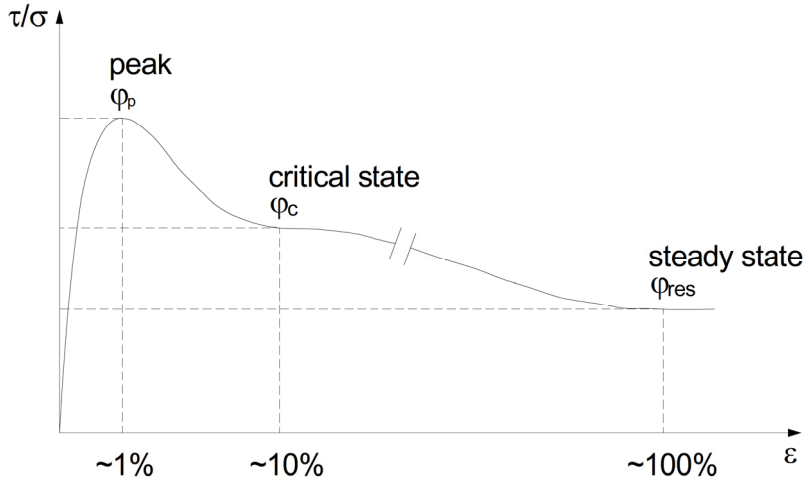

Fig. 10 Strength-strain relation with respect to the friction angle [23]

3.1.1 Peak friction angle φ_p

The *peak friction angle* φ_p indicates the friction angle at maximum shear strength, not to be confused with the *friction angle at failure* φ_f. The latter is related to boundary conditions (such as deformation and failure criterion). The friction angle at the maximum stress ratio reduces with a decreasing relative density and an increasing mean effective stress. Due to an increase in stress the dilatancy angle decreases. The effect of high stress levels on loose and dense sands was investigated by Ortigao in [24] (see Fig. 11).

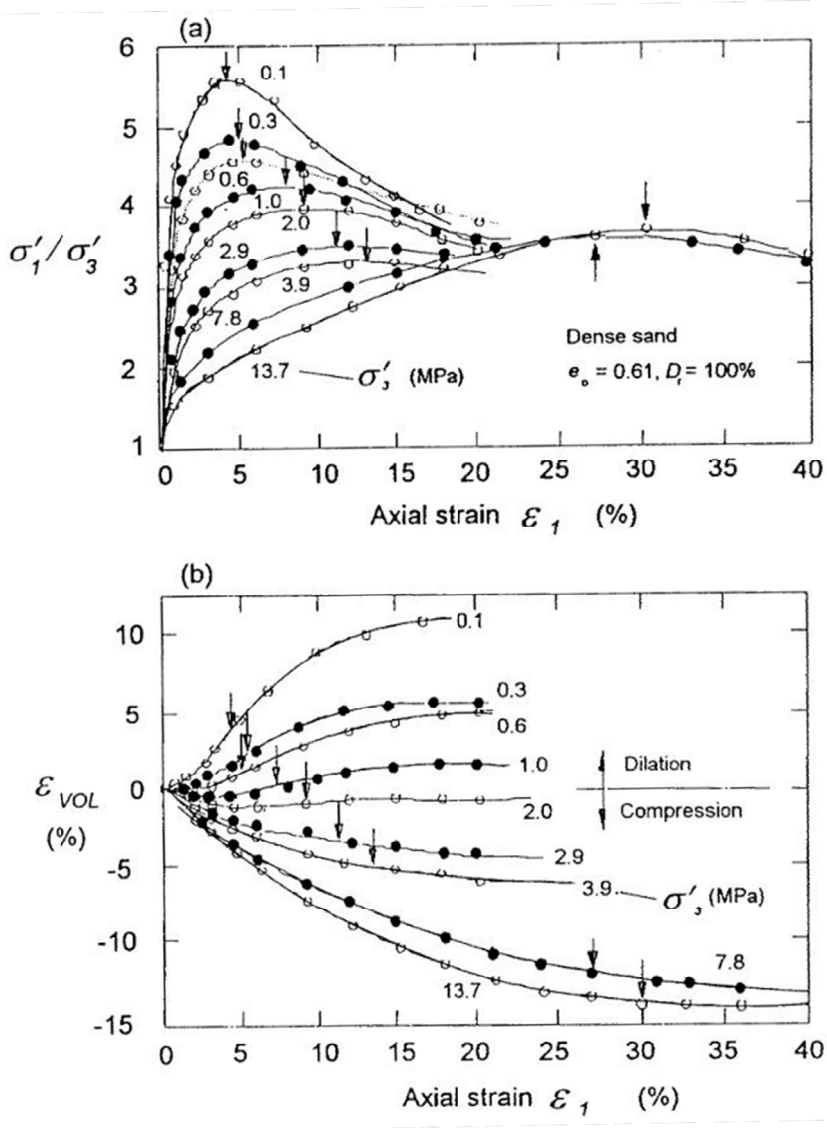

Fig. 11 Behaviour of dense sand in triaxial tests [25]

Further characteristics influencing the peak value of the friction angle are proposed in the literature e.g. [26], [27] and [28]:

- Relative density
- Pressure range
- Stress state
- Constitutive model
- Anisotropy
- Arrangement of the soil test
- Grain distribution
- Mineral composition

3.1.2 Critical friction angle φ_{cv}

In contrast to the peak friction angle φ_{cv} is a real soil parameter. Due to the fact that the critical friction angle belongs to the mineral structure regardless of the relative density. As shown in Fig. 10 the critical friction angle or friction angle at constant volume φ_{cv}

occurs at relatively large deformation ranged from 10 % to 40 % [23]. There, a kind of plateau is reached by means of a constant stress ratio and no change in volume (void ratio). The void ratio which does not change any further is called the critical void ratio e_c.

3.1.3 Residual friction angle φ_{res}

If large deformations (~100 %) [23] occur after reaching the critical state, the residual strength at steady state is obtained. In contrast to the critical state, particles in the shear plane are orientated in a statically constant structure [23]. In order to trigger such a parallel orientation a sufficient clay content is required. For this reason, a small drop in the stress ratio might be determinable. Consequently these implies cohesive soils with medium to strong plastic deformability. Precisely, the steady state describes the critical state based on velocity rates. That means next to the stress and volumetric deformation rate also the velocity rate vanishes a critical void ratio [29].

3.2 Shear test

The evaluation of a shear test describes a general behaviour of soil under shear stress. Generally speaking, the shear test is a boundary value problem and leads to an unknown stress path during shearing (DSB test). Two common methods of shearing are presented in the following.

3.2.1 Direct shear test (DSB)

The direct shear test consists of two frames placed on each other (shear box). The shear box can be quadratic (Casagrande shear box [30]) or circular (Jenike shear cell [31]). The upper as well as the lower half are filled with the soil sample. Hence, a plane (failure plane) in the central of the shear box is prescribed. A vertical *normal force N* acts on the top of the shear box, which is maintained constant during the test. Additionally, a *horizontal force T* is applied on one of the frames in order to translate it relatively to the other half resulting in a formation of the horizontal shear zone (see Fig. 12). Therefore, *T* is increased incrementally in such a way that the shear rate is constant. It is of importance to adjust the normal force and the shear rate with the soil type, the preloading and the construction project. The required shear force is measured by means of a force gauge. Whereas the shear displacement, as well as the reduction of the sample thickness, are gained by a transducer. The ratio of those two forces is assumed to give an average ratio of shear stress to normal stress acting on the shear plane.

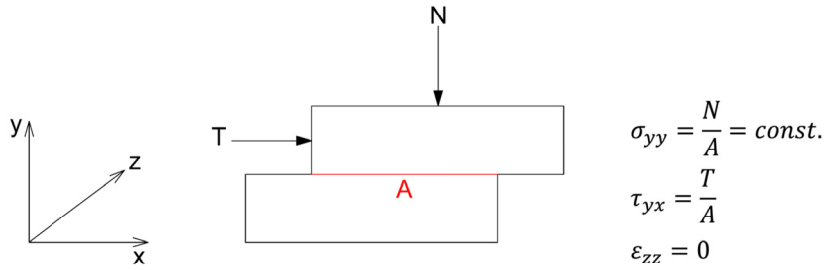

Fig. 12 Shematic representation of DSB

The evaluation of a direct shear test strongly depends on the test arrangement. As explained above, the correlation of the normal force and the horizontal force are clearly defined, which is not the case for the stress ratio. The conventional test arrangement includes a top plate which rests freely on the soil sample. Due to this boundary condition a non-uniform stress distribution develops on the shear plane in the soil. However, in geotechnical engineering the shear strength is defined by stresses. Therefore it is of importance to generate a uniform stress state. If the top plate is fixed with the upper half of the shear box, it moves as a unit and therefore a more uniform stress distribution on the shear plane is achieved. [20]

Unfortunately, the exact stress state within this shear zone is unknown. A shear test belongs to plane strain condition and its interpretation is usually based on the Mohr-Coulomb failure criterion. This leads to the fact, that the Mohr´s definition of failure is equated with that of Coulomb. At this point it has to be mentioned that this statement is disproved in chapter 4.2. The problem is also addressed in [22] by performing numerical simulations of the direct shear test based on the Discrete Element Method (DEM). There it is said: "*The consequence of this assumption is that it is implied that failure planes (shear bands) are planes of maximum stress obliquity, i.e.* τ/σ *is a maximum possible value for the corresponding Mohr circle of stress*." However, a fully defined shear band presents a line of zero extension (velocity characteristics, see [32]). The mobilised shearing resistance acting on the plane (in the standard DSB test) is described by the *direct shear angle of friction* φ^{ds}, which satisfies the Coulomb failure criterion. In the literature the friction angle based on this criterion is also called *Coulomb friction angle* ϕ, so that $\varphi^{ds} = \phi$. The Mohr-Coulomb failure criterion, however, is defined by the *plane strain angle of friction* φ^{ps} and relates to the stress characteristics [20]. As evident from Fig. 13 the formulation $\varphi^{ds} < \varphi^{ps}$ is valid. A detailed difference between both failure criteria is provided in chapter 3.4.1.

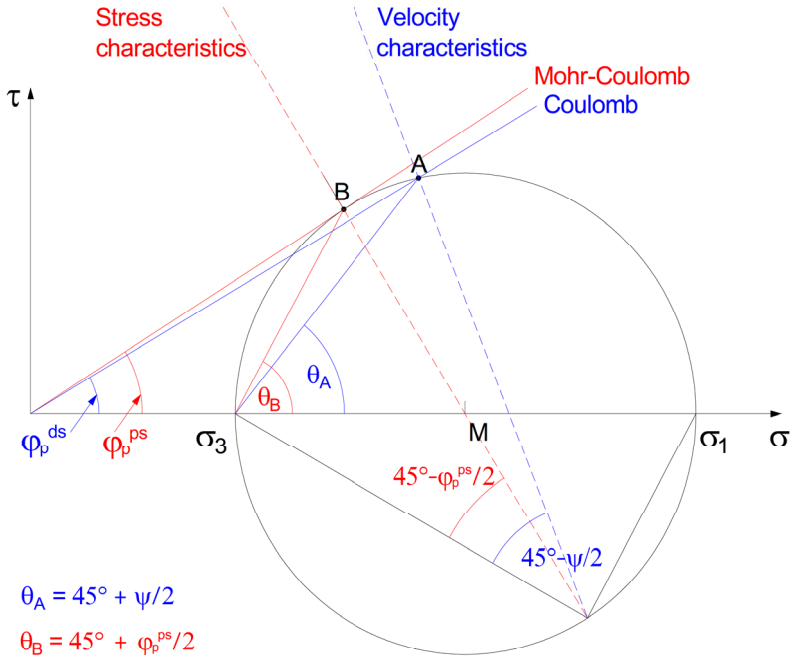

Fig. 13 Differences of friction angle of plane strain and direct shear

3.2.2 Direct simple shear test (DSS)

The Direct simple shear test or also simple shear test provides an improved kinematic arrangement and results in a fairly uniform stress state. Furthermore, the failure mechanism of a direct simple shear test is closer to a slope failure than the direct shear test since no shear plane is predefined. As well as for the DSB several test configurations exist. For example the isochoric simple shear test (constant volume test). There the distortion in all three direction is prevented by a fixed top plate, so that $\varepsilon_{xx} = \varepsilon_{yy} = \varepsilon_{zz} = 0$. This restriction causes constant volume where only shear strain is admitted. Another type of DSS (constant load test) provides a moveable top plate which allows deformation in upward direction, hence $\varepsilon_{yy} \neq 0$. During the test run, a constant vertical normal force *N* is applied and a horizontal force *T* deforms the specimen (see Fig. 14). As in the DSB the forces are converted into stresses in order to plot the stress-strain-relation (compare Fig. 15).

Although the test setup differs from a direct simple shear test, laboratory as well as numerical experiments have shown that the peak and residual strength of this two test types are almost identical [33], [34] and [35]. Hence, the friction angle of a DSS is equal to that obtained in a DSB and relates also on the Coulomb failure criterion.

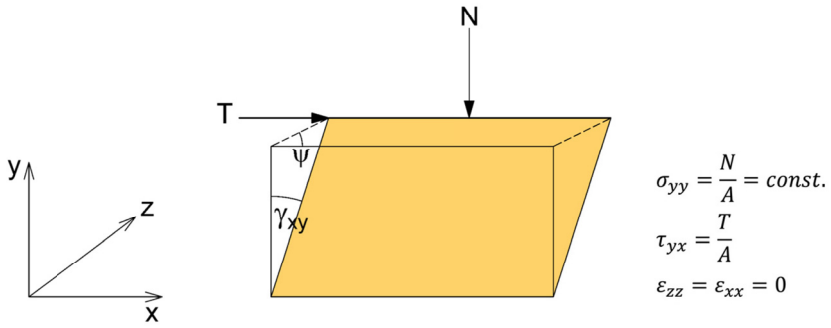

Fig. 14 Shematic representation of DSS

3.2.3 Test results

The corresponding Mohr circle of the shear plane is unknown, since the acting normal stress on this plane as well as the principal effective stresses are unquantifiable. For this reason, in laboratory tests the strength parameters are evaluated by the peak stress ratio assuming $T/N = (\tau/\sigma)_{max}$. Thereby, the measured friction angle is based on the Coulomb failure criterion. If the test is continued after reaching the peak value, the horizontal force reduces, provided that the shear rate is kept constant and the shear way of the sample is long enough. At this point the critical state is attained, which implies no change in the stress ratio. In other words, the shear deformation occurs under constant volume. (see Fig. 15)

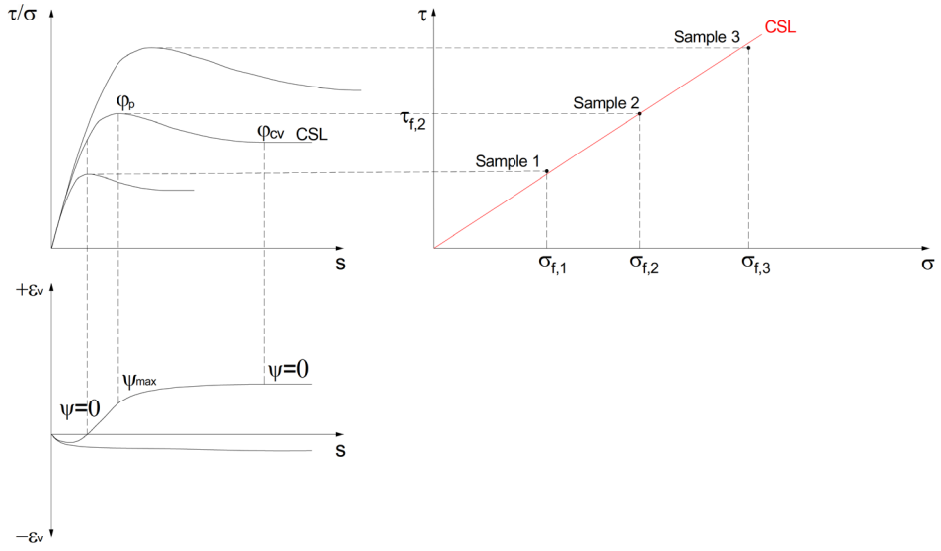

Fig. 15 Interpretation of a shear test

For both test applications the same soil parameters are observed. Those are:

- Effective cohesion c'
- Effective friction angle at peak φ'_p
- Effective friction angle at critical state φ'_{cv}

Although, in practice the exact determination of the peak and residual value is difficult due to the restricted shear displacements. The problem can be solved by using a ring shear test [36], which is not further discussed here. Moreover, it is challenging to reproduce the in-situ stress state. However, the strength parameters are strongly stress dependent and decrease with increasing stress level (depth). Additionally in a DSS, it is possible to determine the dilatancy angle ψ. Its magnitude highly depends on the relative density but also on the friction angle.

It should be mentioned, that the results are restricted by some assumptions such as, a zero extension line along the horizontal shear plane or coaxiality of the principal stresses. Whereas it is indicated in [20], that the principal axis of incremental strain are ahead of the principal axis of stress.

3.3 Triaxial test

In a triaxial test the stress path is defined, thus the test is stress controlled. The results differs from that evaluated in a shear test. A shear test exhibits plane strain conditions rather than triaxial conditions. However, in a triaxial compression test, an almost homogeneous deformation is possible until the maximum stress ratio is achieved [37]. A major advantage in comparison with the shear test is the measurement of the pore water pressure, if an undrained test is performed.

3.3.1 Testing procedure

The surface of a cylindrical saturated soil sample is covered by an impervious membrane. The top and bottom of the soil sample is bounded by porous stones. This test construction is situated in a triaxial cell filled with water, so that the sample is under hydrostatical pressure. There the soil sample is consolidated isotropically ($\sigma_1 = \sigma_2 = \sigma_3$) or anisotropically ($\sigma_1 \cdot K_0 = \sigma_2 = \sigma_3$). The subsequent test procedure differs according to its drainage type. Usually an isotropically consolidated undrained compression test (CU) or an isotropically consolidated drained compression test (CD) is performed. In the former case (CU) the drainage is prevented whereas in the latter case (CD) drainage is permitted during load increment. Another test type is the unconsolidated undrained compression test (UU), but due to its less frequently application it is not further discussed here.

After consolidation the vertical load is increased until failure occurs. However, the cell pressure is kept constant. Hence, the minor principal stresses σ_2 and σ_3 are equal to the surrounding fluid pressure and the major principal stress σ_1 depends on the vertical load.

At this point it should be noted that an intermediate principal stress σ_2 greater than σ_3 is not taken into account in the standard testing procedure. In order to control all three principal stresses separately, the Hollow Cylinder Apparatus has been designed [38]. Due to this fact the resulted friction angle and cohesion in a triaxial test differ from tests where plane strain conditions are assumed. Beside the principal stresses, axial strains ε_1, as well as lateral strains $\varepsilon_2 = \varepsilon_3$, are measured.

3.3.2 Test results

In normal practice stress states are illustrated with the help of the Mohr circle. During the consolidation phase ($\sigma_1 = \sigma_2 = \sigma_3$) no *shear stress* τ is obtained ($\tau = 0$), only after an additional vertical load application σ_1 increases, consequently the shear stress τ increases. The critical state is reached as soon as no further stress increment is possible with ongoing deformation (see also Fig. 16).

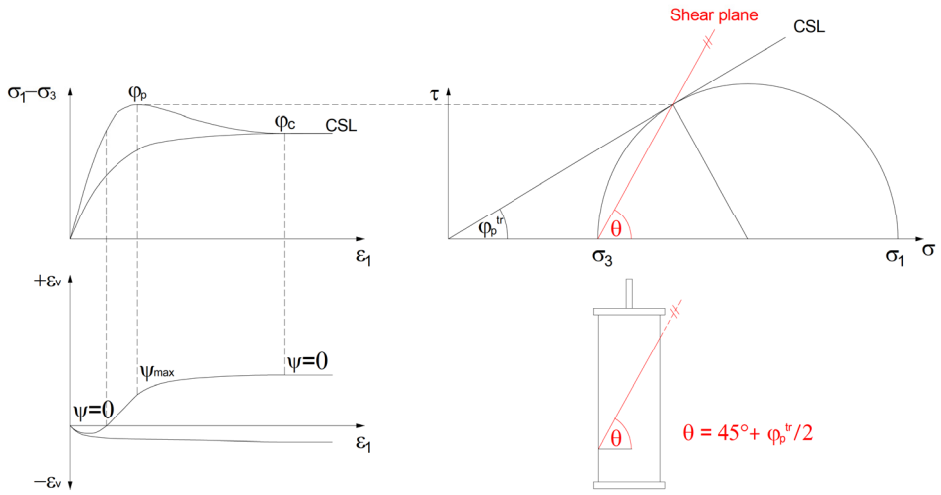

Fig. 16 Interpretation of a triaxial compression test

Generally, in a triaxial test any stress path can be performed. In order to validate the MS Excel worksheet a triaxial compression as well as triaxial extension test are reproduced as shown in Fig. 17 and Fig. 18. In a triaxial extension test a cell pressure greater than the amount of the vertical stress is applied.

Fig. 17 shows a triaxial compression test ($\sigma_3 = \sigma_2 \leq \sigma_1$). The corresponding stress path is plotted in the p-q-space. There the light blue arrow along the p-axis indicates the consolidation phase whereas the orange arrow plots the incremental growth of the vertical stress σ_1 until it hits the MC failure line. This situation is also shown in the π-plane, where the stress path moves from the origin to the upper apex (triaxial compression point at θ = -30°). The green line represents the yield surface of the

Matsuoka-Nakai criterion, whereas the hexagon (black line) represents the yield surface of the Mohr-Coulomb criterion.

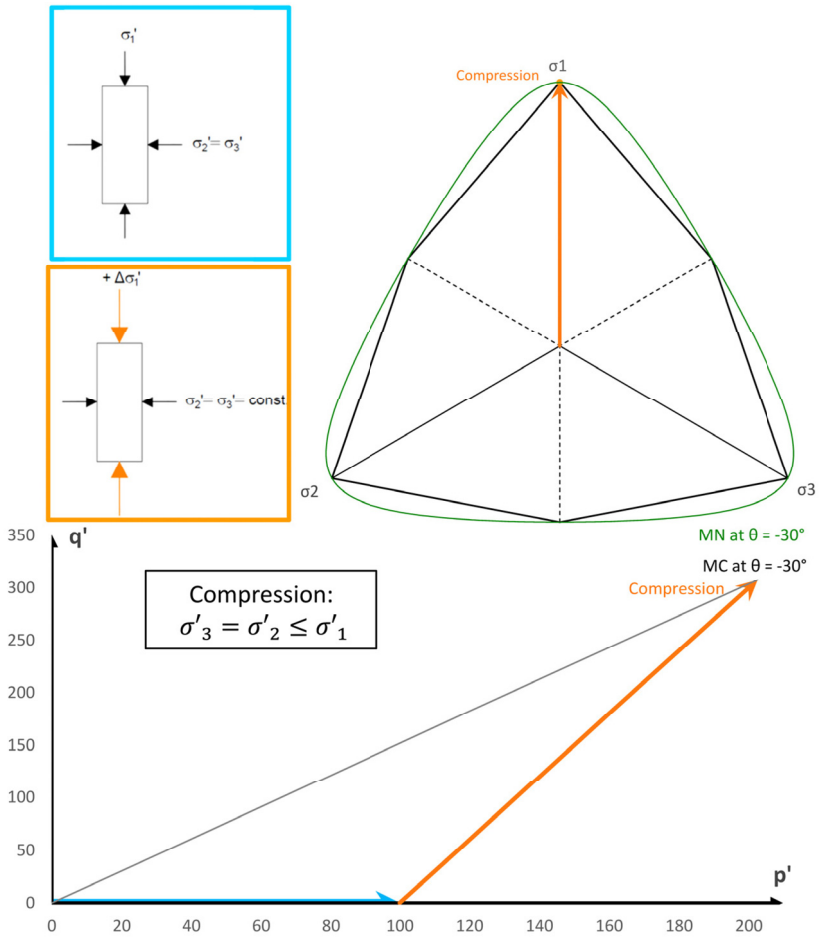

Fig. 17 Triaxial compression test in p-q-space and π-plane

Fig. 18 corresponds to a triaxial extension test ($\sigma_3 \leq \sigma_2 = \sigma_1$). The procedure is similar to a compression test with the difference that the vertical stress is reduced after the consolidation and its notation is changed to σ_3. The corresponding stress path is plotted in the p-q-space. There the light blue arrow along the p-axis indicates the consolidation phase whereas the deep blue arrow plots the incremental reduction of the vertical stress σ_3 until it hits the MC failure line. This situation is also shown in the π-plane, where the stress path moves from the origin to the left apex (triaxial extension point at θ = +30°). The green line represents the yield surface of the Matsuoka-Nakai criterion, whereas the hexagon (black line) represents the yield surface of the Mohr-Coulomb criterion.

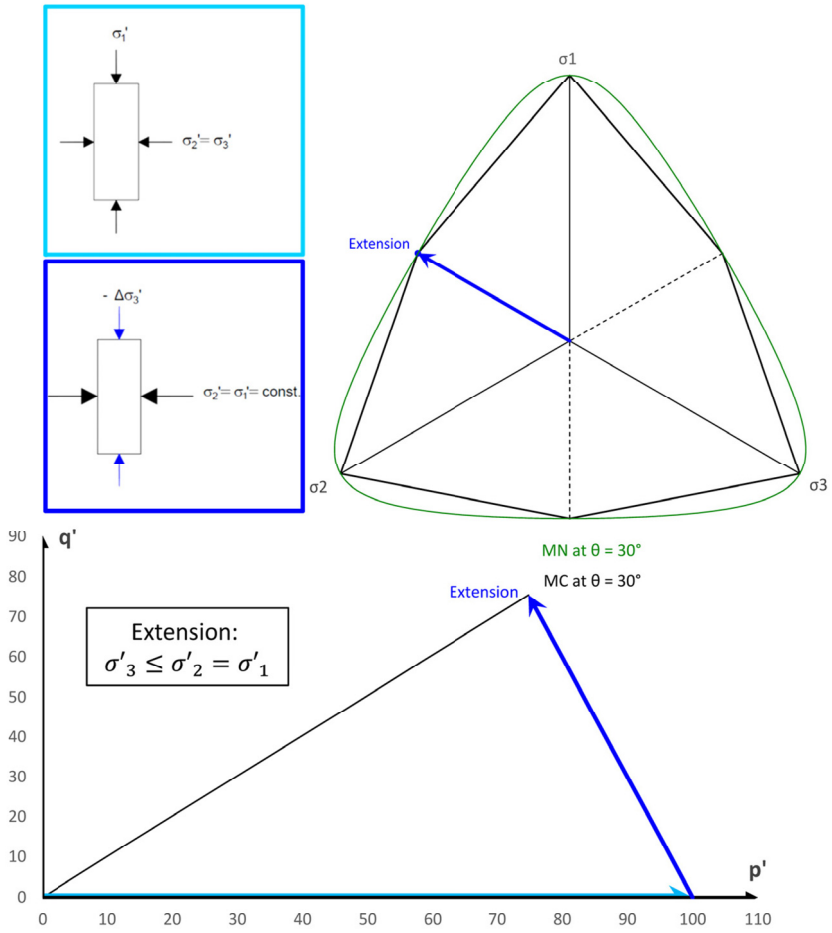

Fig. 18 Triaxial extension test in p-q-space and π-plane

3.4 Approaches of friction angle determination

The way of deriving the friction angle is of importance for the determination of the factor of safety. Since a shear test or a triaxial compression test will yield different friction angles.

3.4.1 Direct shear vs. plane strain

This chapter summarizes different approaches with respect to the relation between the *direct shear angle of friction* φ^{ds} and the *plane strain angle of friction* φ^{ps}. If not specified explicitly, then the terms are related to peak strength.

Rowe published in [21]:

$$\tan \varphi^{ds} = \tan \varphi^{ps} \cos \varphi_{cv}^{ps} \qquad (51)$$

Davis presented in [3]:

$$\tan \varphi^{ds} = \frac{\sin \varphi^{ps} \cos \psi}{1 - \sin \varphi^{ps} \sin \psi} \quad (52)$$

Assuming no change in volume, i.e. $\psi = 0$ and $\varphi^{ps} = \varphi_{cv}$ Equ. (51) and Equ. (52) are the same with $\tan \varphi^{ds} = \sin \varphi^{ps}$.

The equation above can also be reformulated for $\sin \varphi^{ps}$ to:

$$\sin \varphi^{ps} = \frac{\tan \varphi^{ds}}{\cos \psi + \sin \psi \tan \varphi^{ds}} \quad (53)$$

Obviously, φ^{ps} is sensitively dependent on the dilatancy angle. Hence, an underestimation of the dilatancy angle yields a significant overestimation of the plane strain angle of friction [20]. It might be worth noting that typical sands of φ_{cv} = 33° - 37° have been investigated in [20]. There, $\tan \varphi^{ps}$ is predicted to be 20 % to 25 % greater than $\tan \varphi^{ds}$.

3.4.2 Direct shear vs. triaxial compression

Next, different approaches with respect to the relation between the *direct shear angle of friction* φ^{ds} and the *friction angle at triaxial compression* φ^{tr} are outlined. If not specified explicitly, then the terms are corresponded to the peak strength.

With the horizontal shear plane as a zero extension line and assuming coincidence of the principal axes of stresses and strains, Taylor introduced in [39] a correlation as follows:

$$\tan \varphi_p^{ds} = \sin \varphi_{cv}^{ds} + \tan \psi \quad (54)$$

The equation above underestimates the peak angle of friction when the dilatancy angle is underestimated. Therefore it is rather a conservative approach.

Equ. (52) introduced by Davis [3] is also used in triaxial compression:

$$\tan \varphi^{ds} = \frac{\sin \varphi^{tr} \cos \psi}{1 - \sin \varphi^{tr} \sin \psi} \quad (55)$$

In [21] it is noted, that $\varphi^{ds} < \varphi^{tr}$ is valid for loose sands but changes to $\varphi^{ds} > \varphi^{tr}$ as the soil density increases. In a loose state, where movements may be more crucial, φ^{ds} displays a more conservative solution and therefore might be preferred.

3.4.3 Triaxial compression vs. plane strain

This chapter summarizes different approaches with respect to the relation between the *friction angle at triaxial compression* φ^{tr} and the *plane strain angle of friction* φ^{ps}. If not specified explicitly, then the terms are corresponded to the peak strength.

According to [20] and [40], little or no difference between both friction angles is observed for loose sands. Therefore it is assumed that:

$$\varphi_p^{tr} \approx \varphi_p^{ps} \approx \varphi_{cv} \tag{56}$$

This assumption implies, that the Mohr-Coulomb failure criterion is appropriate for very loose soil as well as for the critical state conditions.

However for dense sands, the plane strain friction angle is 5 % - 14 % greater than the friction angle predicted for triaxial compression [40]. In [40] it is proposed that the differences between these two angles get smaller as φ_p^{tr} decreases and tends to be zero at the critical state. A linear relationship which describes this trend quite good is presented by Schanz and Vermeer [26], which combines the empirical equations of Bolton [41].

Empirical equation of Bolton [41]:

$$\varphi_p^{ps} = \varphi_{cv}^{ps} + 0.8\,\psi = 5(I_D(10 - \ln p) - 1) + \varphi_{cv}^{ps} \tag{57}$$

$$\varphi_p^{tr} = 3(I_D(10 - \ln p) - 1) + \varphi_{cv}^{tr} \tag{58}$$

Combined equation introduced by Schanz and Vermeer [26]:

$$\varphi_p^{tr} \approx \frac{1}{5}\left(3\varphi_p^{ps} + 2\varphi_{cv}\right) \tag{59}$$

4 Slope inclination at failure

4.1 Classic derivation based on limit equilibrium consideration [42]

The factor of safety is derived from the method of slices. The acting forces on an arbitrary slice of a cohesionless infinite slope are considered in order to compute a statically admissible state. A stress field is classified to be statically admissible if the equilibrium, the boundary conditions with respect to external loads as well as the yield criterion are satisfied. Due to the fact that in the following no water table is defined, the labelling of the effective stresses has been deliberately renounced.

The forces acting on this arbitrary slice are the gravity load of the soil *G*, the reaction force *Q* (as a result of *G*) and the load due to the surrounding soil *E* (see. Fig. 19)

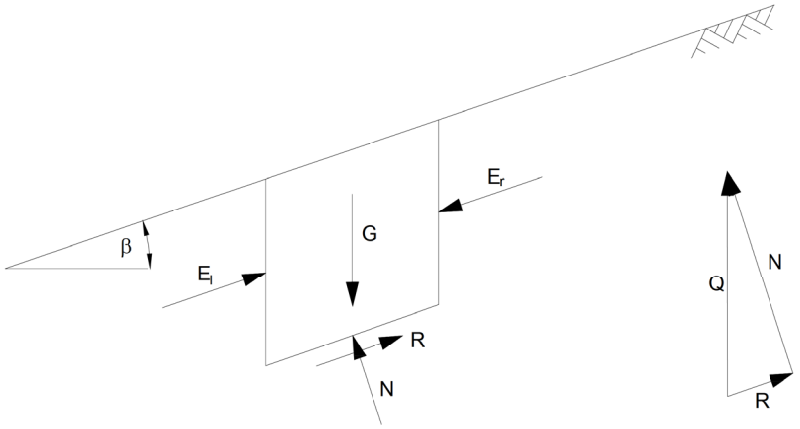

Fig. 19 Method of slices [42]

Because of infinity, the line of action as well as the magnitude are equal for both earth pressures (E_l and E_r). For this reason no additional moment is computed and the forces cancel out. This means that the slope inclination at failure is calculated only by means of *G* and *Q*. The related relation is derived below.

First the gravity load is divided in a stabilizing force $G_\perp$ and a destabilizing force $G_{//}$.

$$G_\perp = G \cos\beta \tag{60}$$

$$G_{//} = G \sin\beta \tag{61}$$

Additionally *Q* can be split into a normal force *N* which acts perpendicular to the bottom and a resistance force R which acts along the bottom plane. Where the magnitude of N is equal to $G_\perp$ but acts in opposite direction. The resistance force depends on the normal force and the effective friction angle at the slip face with:

$$R = N \tan \varphi = G \cos \beta \tan \varphi \quad (62)$$

Putting the resistance force R in a relation with the driving force $G_{//}$ a statement about the ultimate limit state in terms of a factor of safety is made.

$$FoS = \frac{R}{G_{//}} \quad (63)$$

According to that, limit state is reached as soon as R is equal to $G_{//}$ and so the slope inclination at failure computes to:

$$R = G_{//} \rightarrow G \sin \beta = G \cos \beta \tan \varphi \rightarrow \tan \beta = \tan \varphi \rightarrow \beta = \varphi \quad (64)$$

As a result the slope inclination at failure is equal to a friction angle in plane strain condition (see chapter 3.2.1). It has to be noted that this method does not take into account the effect of the dilatancy angle. However, studies in [2] showed, that from a soil mechanics point of view, it is advisable to use a non-associated flow rule to describe soil behaviour. As presented in [1] this could yield significantly lower values of FoS. The importance of the flow rule is discussed below.

4.1.1 Influence of the flow rule

Tschuchnigg et al. observe in [1] that especially for high friction angles ($\varphi \geq 35°$) and steep slopes the factor of safety with a non-associated flow rule diverges from that with an associated flow rule. Generally, a non-associated flow rule leads to a lower factor of safety. It is of interest to point out, that the Matsuoka-Nakai criterion leads to a higher factor of safety as obtained with Mohr-Coulomb. This might be one reason, why conventional calculated slopes with a slight inclination are still stable in practice, at least for a dilatancy angle $\psi > \varphi/3$.

Moreover, it appears that cohesive soils are less dependent on the flow rule. This confirms the big impact of the cohesion on the factor of safety as studied later on (chapter 5.2.1).

If non-associated behaviour is considered, strong oscillations during the φ-c-reduction can occur. This makes it almost impossible to determine a unique factor of safety. The instable calculation state is triggered by multiple possible failure mechanisms (bifurcation). Those are consequences of multiple solutions in the boundary value problem. Furthermore, the erratic behaviour is more pronounced with greater difference between the friction angle φ and the dilatancy angle ψ.

The consequence on the slope inclination at failure based on a non-associated flow rule is studied in the next chapter.

4.2 Simple shear mechanism

As already discussed in chapter 3, different soil tests result in different friction angle and consequently also in different FoS. As illustrated in Fig. 20 the failure mechanism, obtained with a simple shear test, is similar to that of an infinite slope.

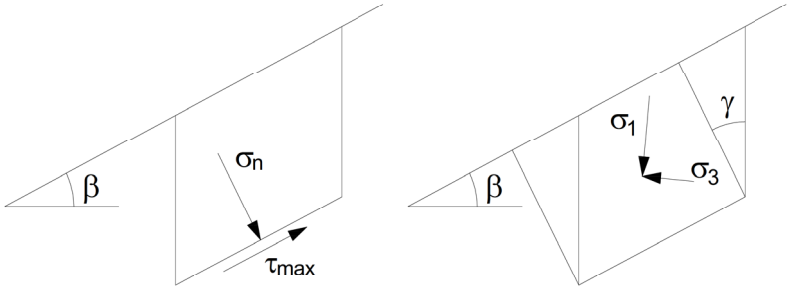

Fig. 20 Possible failure of an element of an infinite slope [5]

A collapse of the soil body is associated with a maximum in shear strain in the shear plane. Due to the assumption of coaxiality, the shear stress has to be also maximum (τ_{max}). Hence, the friction angle at failure according to a simple shear mechanism can be expressed on the basis of the Coulomb failure criterion (see Equ. (1)) as followed:

$$\tan \varphi^{ds} = \frac{\tau_{max}}{\sigma_n} = \frac{p_v \sin \beta}{p_v \cos \beta} = \tan \beta \qquad (65)$$

Where τ_{max} is the maximum shear stress in the slip surface and p_v indicates the vertical stress on the sliding surface of an arbitrary soil element.

In reality, a friction angle at failure (obtained with a triaxial compression test (Mohr´s failure criterion)) differs from the equation above in:

$$\sin \varphi^{tr} = \frac{\sigma_1 - \sigma_3}{\sigma_1 + \sigma_3} = \frac{\tau_{max}}{\sigma_n} = \frac{p_v \sin \beta}{p_v \cos \beta} = \tan \beta \qquad (66)$$

Equ. (66) in Equ. (65) results in:

$$\tan \beta = \tan \varphi^{ds} = \sin \varphi^{tr} \qquad (67)$$

Obviously, the friction angle obtained from a shear test corresponds to the slope inclination at failure. Whereas the friction angle of a triaxial test is greater (see also Fig. 21). It has to be mentioned, that the equations above assume a dilatancy angle of $\psi = 0$. This is for example the case at steady state (critical state), where shear deformation

occurs without any change in volume, i.e. $\psi = 0$. However, it might be reasonable to suppose that the steady state (critical state) is generally not reached in a soil body, which is in limit state, since the required deformations do not occur. The determination of the slope inclination at failure including a dilatancy angle unequal to zero is described in the chapter below.

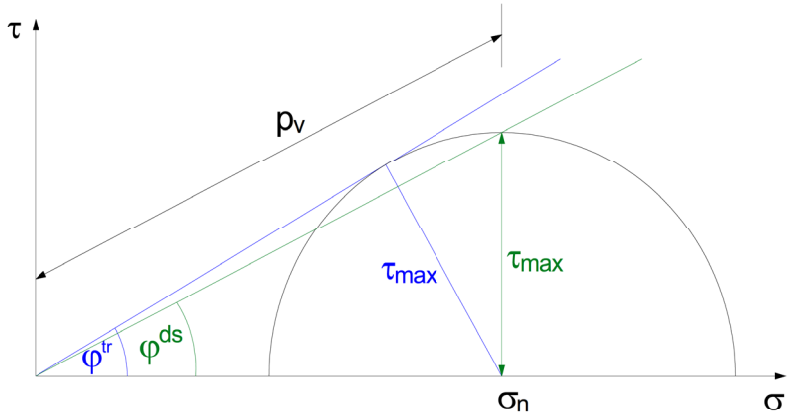

Fig. 21 Friction angle according to triaxial test and simple shear test [42]

4.2.1 Elastic-perfectly plastic MC model

The first approach is based on the Mohr-Coulomb failure criterion and holds for cohesionless material. Under consideration of a non-associated flow rule with a dilatancy angle greater than zero and smaller than the friction angle obtained in a triaxial test following formula is outlined [3]:

$$\tan\beta = \tan\varphi^{ds} = \frac{\sin\varphi^{tr}\cos\psi}{1-\sin\varphi^{tr}\sin\psi} \qquad (68)$$

Note, the formula above is equal to Equ. (52). Moreover, for $\psi = 0$ Equ. (68) reduces to Equ. (67). And for $\psi = \varphi^{tr}$ Equ. (68) reduces to Equ. (64).

In an infinite slope lateral strains cannot develop and plane strain condition are present. However, the Mohr-Coulomb failure criterion does not consider this increased mobilised strength and leads to conservative solutions with respect to FoS.

4.2.2 Elastic-perfectly plastic MN model

The second approach is based on the Matsuoka-Nakai failure criterion and provides a possibility to include the “additional” strength as a consequence of the intermediate principal stress.

The equation presented below was published in [5]. It is an approximation of a numerical simple shear test under plane strain conditions based on an elasto-plastic Matsuoka-Nakai failure criterion. However, reasonable results are achieved for a dilatancy angle between 0 and $\varphi/3$ $(\max \Delta\varphi = \pm 5\%)$.

$$\tan\beta = \tan\varphi^{ds} = \frac{\sin(1.085\varphi^{tr})\cos\psi}{1-\sin\varphi^{tr}\sin\psi} \qquad (69)$$

5 Slope stability analysis

Displacement finite-element analysis is a powerful software and finds increasing acceptance in geotechnical practice. Not just because of a user-friendly interface but also because of advantages related to stability prediction. Some advantages are:

Firstly, the failure mechanism or the slip surface has not to be assumed in advance but is a result of the calculation.

Secondly, a displacement finite-element analysis allows the link between strength and stiffness. In contrast to the approximate LEM discussed in chapter 4.

Thirdly, finite-element codes allow the use of advanced constitutive model to study working load conditions. Those enable a consideration of a non-associated flow rule, realistic stress-strain relation in terms of hardening and softening, creep for soft soil conditions and so on.

This chapter investigates the slope inclination at failure for cohesionless finite slopes computed with the finite-element code Plaxis 2D [6] and compares it with a theoretical approach according to [5]. Further analyses are performed to investigate the stress path development based on the failure criteria Mohr-Coulomb and Matsuoka-Nakai.

Due to the fact that in the following subchapters no water table is defined, the labelling of the effective stresses has been deliberately renounced. Hence, the *effective stresses* σ' are equal to the *total stresses* σ.

5.1 Strength reduction method

In a strength reduction procedure the failure surface is incrementally decreased, which enforces the system to stress redistribution until equilibrium can no longer be maintained. This procedure is also known as φ-c-reduction, which indicates the mathematical relationship as followed:

$$FoS = \frac{\tan \varphi'}{\tan \varphi'_{limit}} = \frac{c'}{c'_{limit}} \qquad (70)$$

It should be emphasised that Plaxis 2D keeps the dilatancy angle constant as long as $\varphi' > \psi'$ is valid. Once the friction angle is equal to the dilatancy angle both are reduced simultaneously [1].

From a soil mechanics point of view, the dilatancy angle belongs to “strength” parameters. Since the factor of safety is derived by strength reduction, the dilatancy angle should be reduced as well from the beginning on [28]. Therefore, performed calculations to determine the limit state in Plaxis 2D, an iterative reduction of the dilatancy angle is included.

5.2 Geometry and material set

This thesis focuses on simple homogeneous slopes in plane strain condition. The dimension of the first model is indicated in Fig. 22, where L = 10 / $\tan\beta$. The slope has a constant height of 10 m but the slope inclination varies between 20° and 50°. High order elements associated with a sufficiently fine mesh are fundamental components for an accurate estimation of the factor of safety. Therefore, a mesh with 15-noded triangles and a *relative element size factor* r_e of 0.5 is generated. In the area of the slope, where large stress concentrations or large deformations are expected, the mesh is refined with a coarseness factor value of 0.1.

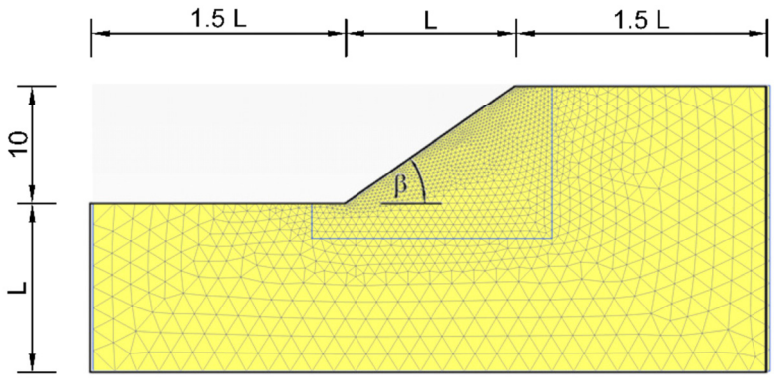

Fig. 22 General slope geometry

A soil under drained conditions is considered and no water table is applied. The unit weight is assumed with $\gamma_{unsat} = 17$ kN/m³ and the Poisson´s ratio with $\nu = 0.3$. All required parameters associated with the individual material models are given in Appendix C.

The earth pressure coefficient at rest (Jaky) is defined as:

$$K_0 = 1 - \sin\varphi \qquad (71)$$

5.2.1 Effect of cohesion

Previous studies performed by [1] have shown an increasing impact of the cohesion with decreasing slope inclination. Therefore it is of interest to evaluate its effect on the failure mechanism and on the factor of safety.

The impact on the FoS with changing cohesion is studied with two different slope inclinations and two different dilatancy angles. First, a necessary friction angle for cohesionless material is found to obtain a FoS value of 1.0. Afterwards the cohesion is increased in small steps to show the importance of choosing a sufficiently accurate value.

It can be identified from subsequent examples (Fig. 23, Fig. 25, Fig. 27 and Fig. 29) that already a slight change in cohesion influences the failure mechanism. At low values a non-uniform failure mechanism appears. On the other hand a growth in cohesion has a “positive” effect on the erratic nature of the failure mechanism as evident from Fig. 30. Though, an exception can be found in Fig. 29 with c = 1.0 kN/m². A reason for this could be the steep inclination of the slope connected with the ratio between friction angle and dilatancy angle. Moreover, the slip plane gets closer to the toe of the slope and a circular shape becomes more pronounced, if small values of c are used in this FEA. Summarised it can be said, the greater the cohesion the deeper and more unique the slip surface.

Additionally Fig. 24, Fig. 26, Fig. 28 and Fig. 30 illustrate the effect on the factor of safety. As expected, a higher value in cohesion results in a greater FoS and provides a more stable calculation. However the factor of safety increases almost 20 % by considering a cohesion of c = 1 kN/m² instead of c = 0 kN/m². This has to be kept in mind!

The examples below are classified due to the dilatancy angle and slope inclination, so that the notation *M_yy_bb* used has following meaning:

- *M*: material model where M = not specified, MC = Mohr-Coulomb, MN = Matsuoka-Nakai
- *yy*: dilatancy angle where *phi_x* means *phi* over *x*
- *bb*: slope inclination

- **M_phi-30_35**

Fig. 23 represents a slope inclined 35° from the horizontal whereas limit state (FoS = 1.0) arises with a friction angle of 37.6° along with c = 0 kN/m² and $\psi = \varphi - 30°$.

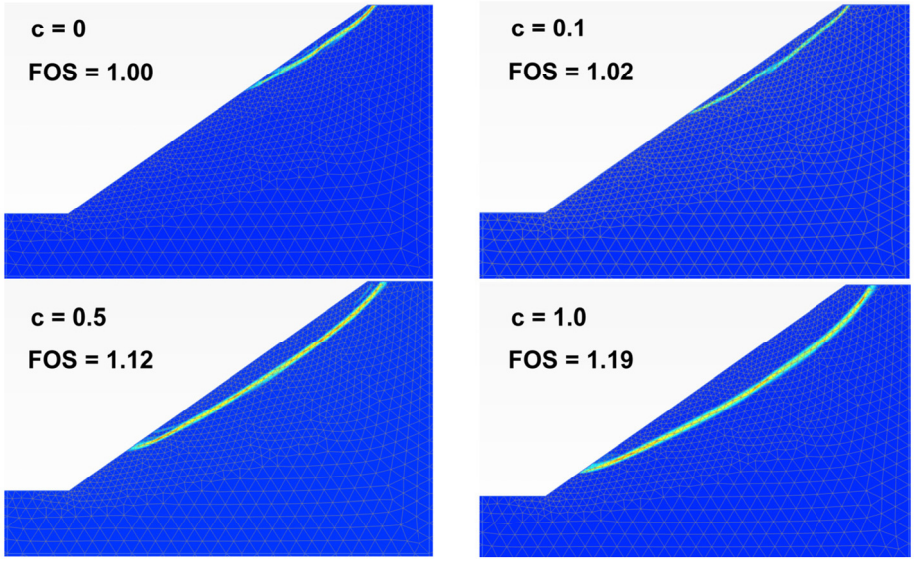

Fig. 23 Incremental deviatoric strain at different cohesion levels on a 35° inclined slope including $\psi = \varphi - 30°$

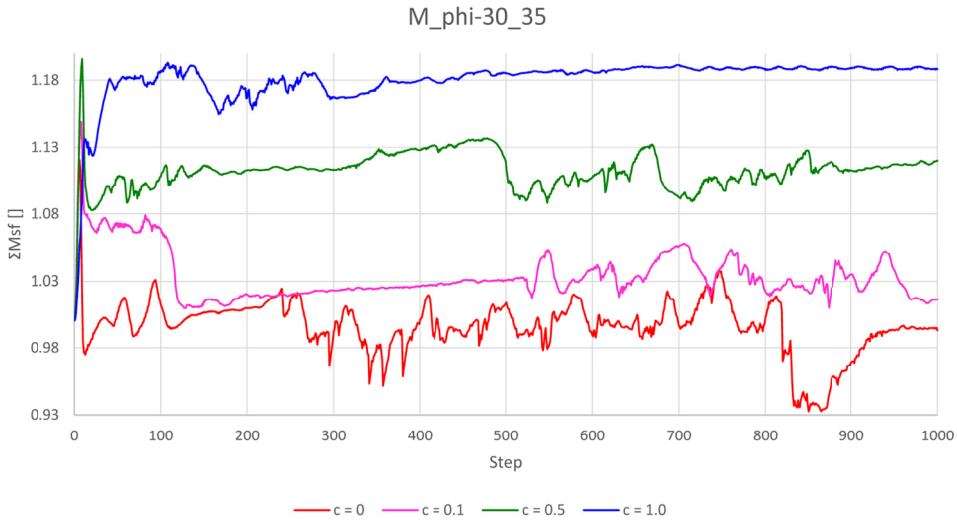

Fig. 24 FoS at different cohesion levels on a 35° inclined slope including $\psi = \varphi - 30°$

- **M_phi_3_35**

Fig. 25 represents a slope inclined 35° from the horizontal whereas limit state (FoS = 1.0) arises with a friction angle of 37.3° along with c = 0 kN/m² and $\psi = \varphi/3$.

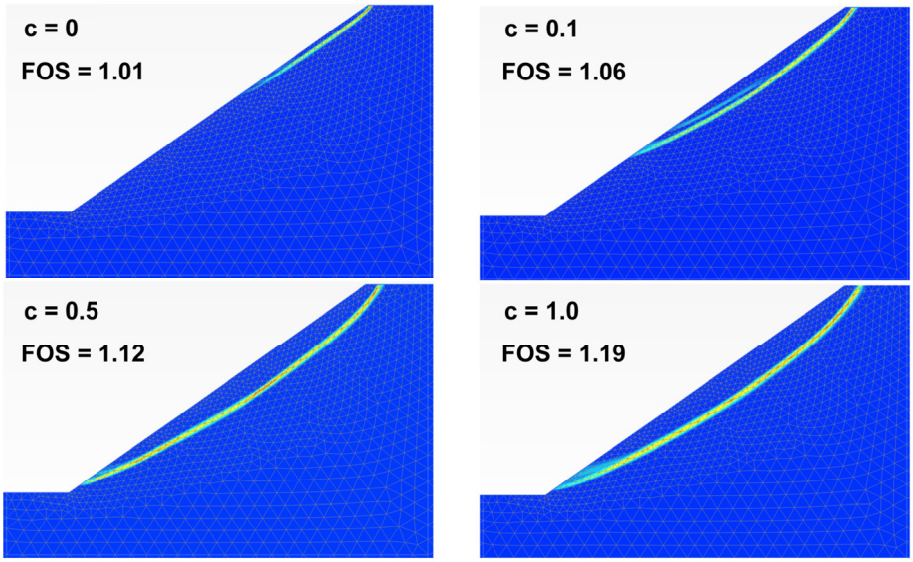

Fig. 25 Incremental deviatoric strain at different cohesion levels on a 35° inclined slope including $\psi = \varphi/3$

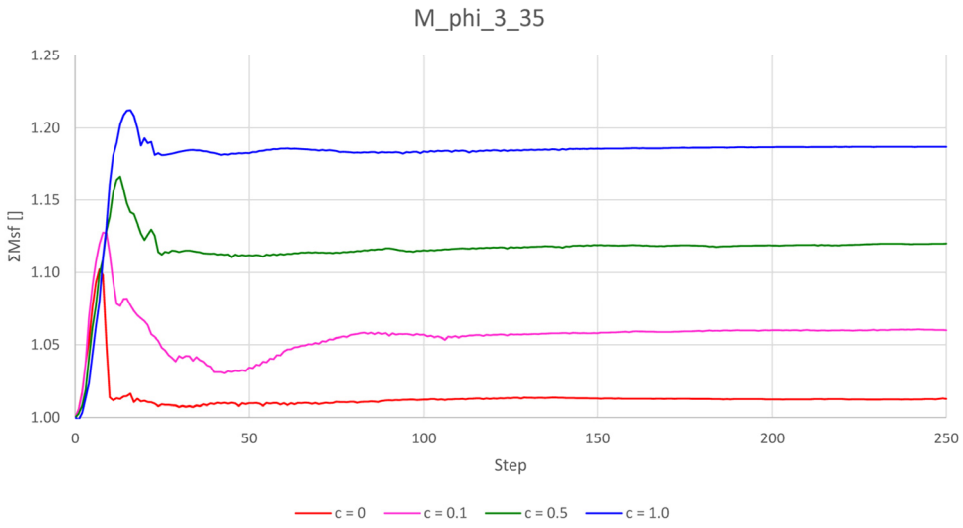

Fig. 26 FoS at different cohesion levels on a 35° inclined slope including $\psi = \varphi/3$

- **M_phi-30_40**

Fig. 27 represents a slope inclined 40° from the horizontal whereas limit state (FoS = 1.0) arises with a friction angle of 43.3° along with c = 0 kN/m² and $\psi = \varphi - 30°$.

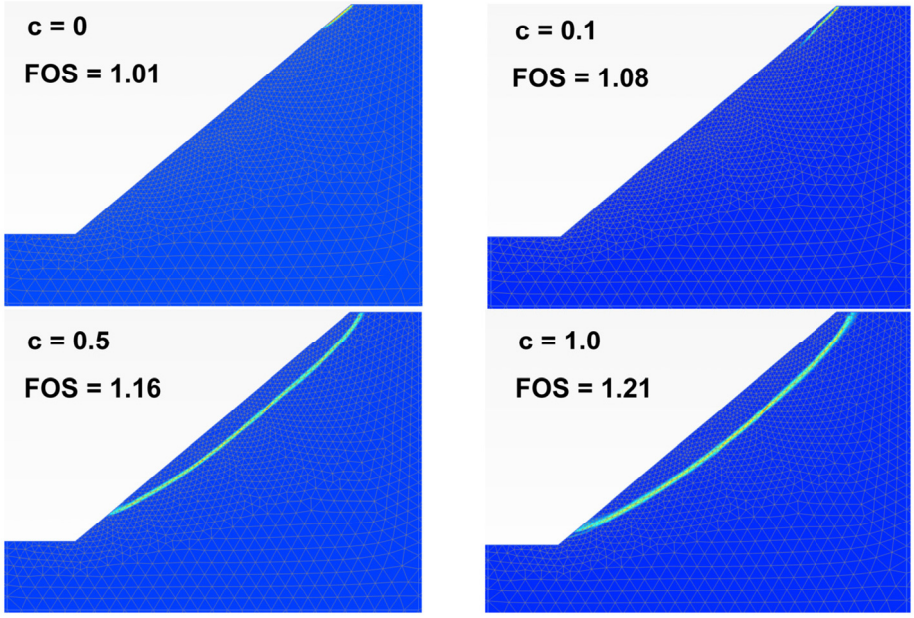

Fig. 27 Incremental deviatoric strain at different cohesion levels on a 40° inclined slope including $\psi = \varphi - 30°$

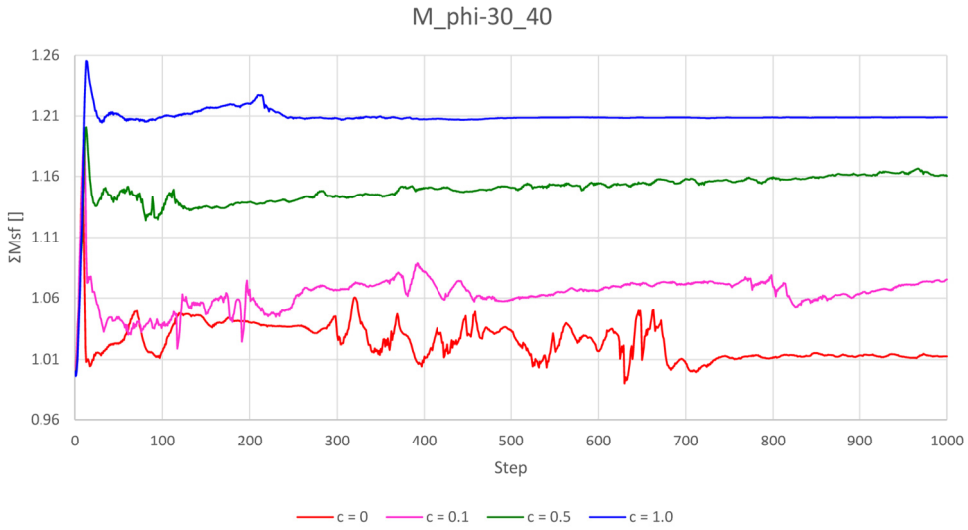

Fig. 28 FoS at different cohesion levels on a 40° inclined slope including $\psi = \varphi - 30°$

- **M_phi_3_40**

Fig. 29 represents a slope inclined 40° from the horizontal whereas limit state (FoS = 1.0) arises with a friction angle of 43.4° along with c = 0 kN/m² and $\psi = \varphi/3$.

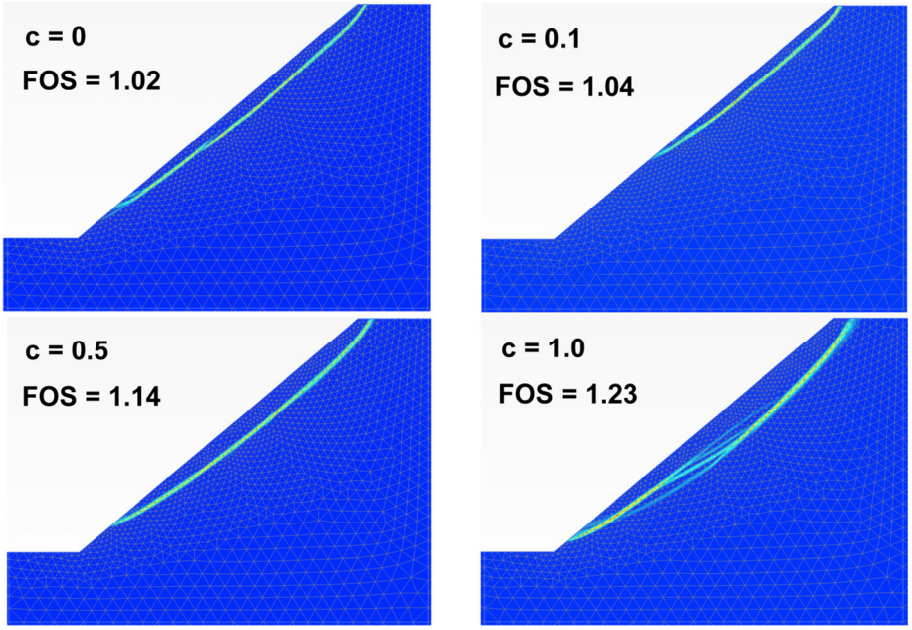

Fig. 29 Incremental deviatoric strain at different cohesion levels on a 40° inclined slope including $\psi = \varphi/3$

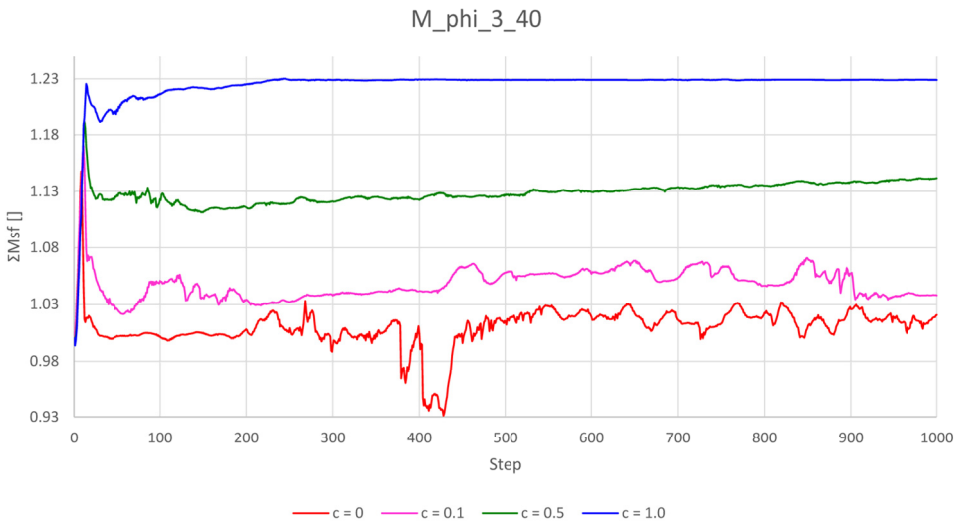

Fig. 30 FoS at different cohesion levels on a 40° inclined slope including $\psi = \varphi/3$

The findings indicate an impact on the failure mechanism and on the FoS even for a relatively small increase in cohesion. Fig. 31 summarizes the effect of the cohesion on the FoS. For this reason it is important that c = 0 kN/m². In some FEA c = 0 kN/m² caused numerical problems and an artificial value of c = 0.001 kN/m² has been chosen (for numerical reasons).

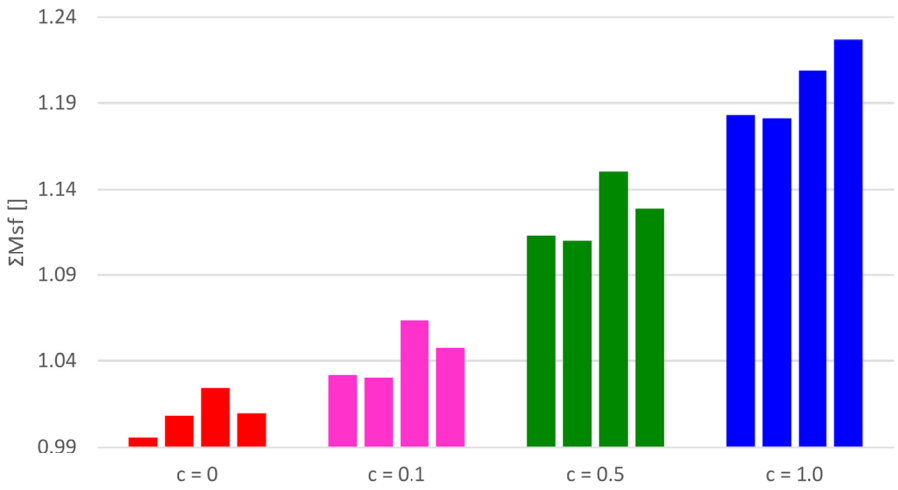

Fig. 31 FoS dependent on cohesion

Later a user-defined soil model is used to work out the FoS, which provides a failure criterion according to Matsuoka-Nakai. Due to numerical instabilities when using this model (arising at steep slope inclinations), a greater artificial cohesion was necessary, which ranges between 0.01 kN/m² and 0.05 kN/m².

5.3 Slope inclination at failure

One aim is to express the ultimate limit state for a predefined slope inclination. The scatter of the factor of safety is defined in a range of $0.99 \leq \text{FoS} \leq 1.02$ and the required friction angle is determined by means of the strength reduction method.

Within the scope of this work the slope angle β is defined with 20°, 25°, 30°, 35°, 40°, 45° and 50°. In general clay soils tend to show less to non dilatancy, unless they are over-consolidated. On the other hand, sands show various values of dilatancy. For example quartz sands show a dilatancy angle about $\psi \approx \varphi - 30°$ [10] and for Hudson sand a dilatancy angle from $\varphi/3$ to $\varphi/4$ is observed [43]. Based on these suggestions the dilatancy angle ψ is varied with $\varphi/3$, $\varphi/4$, $\varphi - 30°$ and 0°.

5.3.1 Mohr-Coulomb criterion

The analysis performed in Plaxis 2D is structured in two phases. The *Initial phase* and the *Safety phase*. The former implies the calculation type *Gravity loading*. This type applies the soil self-weight to generate an initial stress field which fulfils equilibrium.

The displacements calculated in the *Initial phase* are reset (*Reset displacement to zero*) parameter is selected at the start of the *Safety phase*. There the φ-c-reduction (chapter 5.1) is used with the *Incremental multipliers* loading type. This allows a specification with a maximal number of steps in which the strength parameters have to

be reduced successfully [44]. The maximal number of steps in the presented examples is defined by 1000 steps with the purpose to ensure a “completed” failure mechanism.

In a first variation the Mohr-Coulomb material model is used, while the dilatancy angle is not directly affected by the φ-c-reduction but is constant with an initial input parameter (see chapter 5.1). This implies that $\psi_{limit} = \psi_{input}$ (as long as $\varphi_{red} > \psi_{input}$).

In a second variation the dilatancy angle is reduced simultaneously with the friction angle:

$$\psi_{limit} = \tan^{-1}\left(\frac{\tan\psi_{input}}{FoS}\right) \quad (72)$$

In a third variation the dilatancy angle ψ_{limit} is related to the limit friction angle and varies occasionally with $\varphi_{limit}/3$, $\varphi_{limit}/4$, $\varphi_{limit} - 30°$ and 0°. However, in the following computations (chapter 5.3.3) the latter is preferred. Note, all quantitative results can be looked up in Appendix D.

5.3.2 Matsuoka-Nakai criterion

After the investigation of the ultimate limit state with the Mohr-Coulomb failure criterion, the more appropriate Matsuoka-Nakai failure criterion is applied in Plaxis 2D. Therefore, two separate user-defined material models (DLL) are used. Preliminary, both models are studied in order to point out potential problems.

One of the user-defined models is the so called “*Generalised Hardening Soil”* model (GHS), which is a more advanced version of the original *Hardening Soil model with Small-strain stiffness* (HSS) [45]. Configurations allow an individual application. One key point of the GHS model is the consideration of the mean effective stress p' in the stress dependency formulation of stiffness:

$$E_{ur} = E_{ur}^{ref}\left(\frac{p' + p_c}{2p^{ref}}\right)^m \quad (73)$$

Moreover, the model contains the application of the Matsuoka-Nakai failure criterion. However, after a number of trials it has not been successful to provide reasonable results by means of strength reduction (see Appendix E). Because of this problem the GHS model is not used in this work.

Preliminary studies with the second user-defined model shows more satisfactory results. Because of this, FEA discussed in the following are based on the latter user-defined model.

Appendix C lists all input parameters, where also a parameter *Model SW* is highlited. There the Matsuoka-Nakai failure criterion can be chosen by using a *Model Switch* (Model SW) set to 2. Besides, a Model SW of 1 considers the Mohr-Coulomb criterion, whereas a Model SW of 3 presents the Lade surface (which is not further discussed in this work). The ratio of shear moduli G_0/G_{ur} is set to 1. As explained in the previous chapter the dilatancy angle is a function of φ.

Initially no equilibrium could be generated with the calculation type *Gravity loading* when adopting the user-defined material model. Especially steep slopes were problematic. Alternatively two methods are investigated to overcome this numerical issue. In the first method the initial stresses are computed with a *K0 procedure* followed by a plastic nil-step, which forces the initial stress field (after stress redistribution) into equilibrium again. A plastic nil-step is a plastic calculation step without any additional loading, which helps to produce an admissible stress state. The second method includes a linear elastic *LE* material during a *Gravity loading* calculation. Subsequently, a plastic nil-step combined with a material change, from *LE* to *MN*, is defined. Finally a φ-c-reduction is performed for all methods.

An overview of the phase structure used in the individual method is listed below:

- **MN-Gravity loading (MN-GR)**
  Phase Initial: *Gravity loading* with the user-defined MN material model
  Phase 1: *Safety phase* by means of φ-c-reduction

- **MN-K0 procedure (MN-K0)**
  Phase Initial: *K0 procedure* with the user-defined MN material model
  Phase 1: Plastic nil-step
  Phase 2: *Safety phase* by means of φ-c-reduction

- **MN-Linear elastic including Gravity loading (MN-LE)**
  Phase Initial: *Gravity loading* with a linear elastic material model
  Phase 1: Plastic nil-step associated with a material change to MN
  Phase 2: *Safety phase* by means of φ-c-reduction

In order to study the impact of each method on the FoS (as well as on the numerical robustness) test runs were carried out with the user-defined construction mode but with SW set to 1, thus using the Mohr-Coulomb failure criterion. A required reference is performed by the material model *Mohr-Coulomb*, which is provided in the Plaxis 2D material data base. In the following, this model (including *Gravity loading* to generate initial stresses) is termed as MC-STD. Next to the individual methods the cohesion is modified between 0.0, 0.1, 1.0 and 10.0 kN/m². For further analysis the results of the test run, with c = 0.0 kN/m², is of interest and therefore outlined in Fig. 32 and Fig. 33. Fig. 33 illustrates the FoS for an associated flow rule ($\varphi = \psi = 37.3°$). More results are presented in Appendix F.

It appears that the method using a linear elastic material in the initial phase is more stable and corresponds quite well with the standard procedure. For these reasons the method MN-LE is applied on further computations.

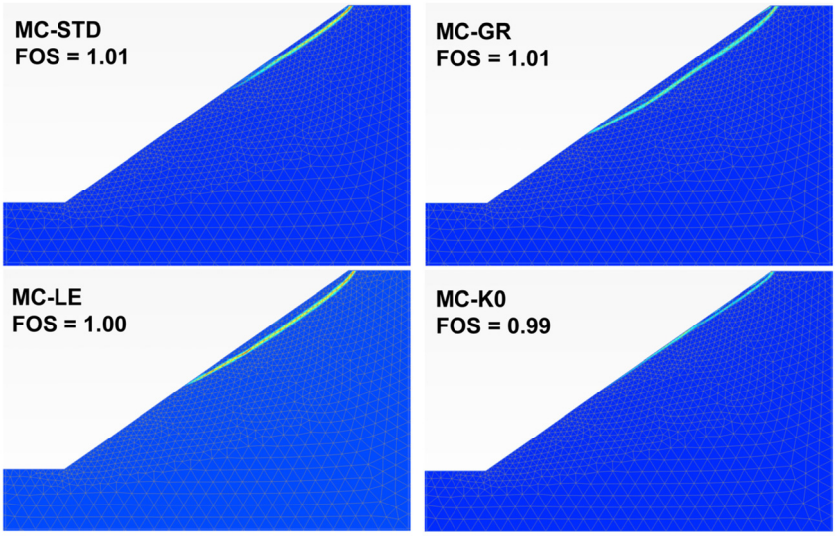

Fig. 32 Incremental deviatoric strain on a slope with $\beta = 35°$ and c = 0 kN/m² based on the user-defined material model

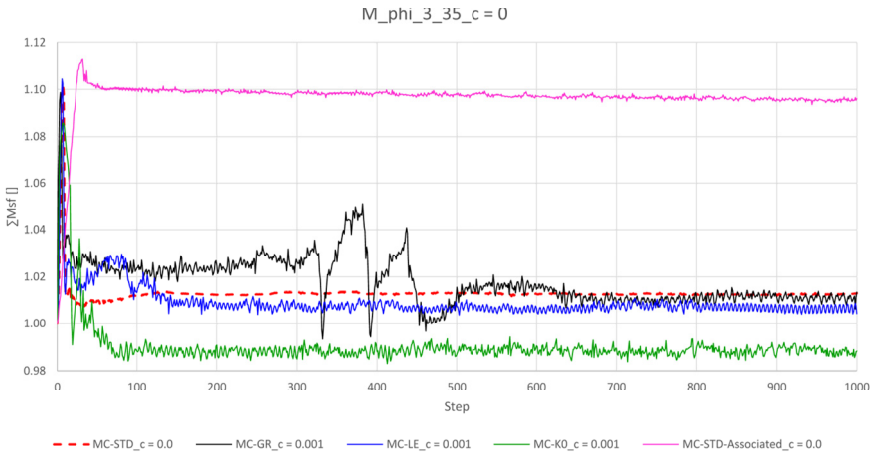

Fig. 33 FoS of a 35° inclined slope with c = 0 kN/m² based on the user-defined material model

Based on a sensitivity analysis it has been found that the user-defined material model has sometimes problems to undertake a φ-c-reduction when MN-LE is used. After a random step number, the occurring plastic points do not correlate with a plausible failure mechanism (see Fig. 34). This behaviour is solved by a small increase in cohesion, which does not influence significantly the factor of safety (see chapter 5.2.1), but provides a more stable calculation. The magnitude of the cohesion is c = 0.03 kN/m². It is suggested to allow tensile stresses. Because of low cohesion values the tensile stresses do not affect the factor of safety significantly as demonstrated in Tab. 1. In contrast, a high accuracy is required by means of a reduced tolerated error (up to 0.1 %). To investigate the effect of the tolerated error a parameter study was performed and will be discussed later in chapter 5.4.

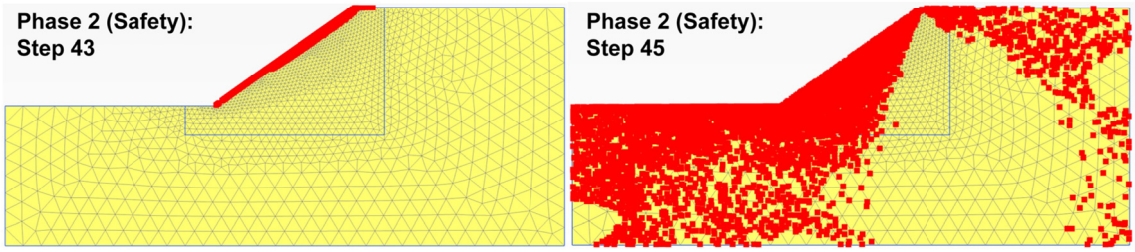

Fig. 34 Stepwise development of plastic points with MN-LE

Tab. 1 Parameters of several trails analysing the effect of tensile stress

Parameter \ Trial		1	2	3	4	5
Plaxis Model		MC -LE	MC -LE	MC -LE	MC -LE	MC -LE
Material Model		LE / MC	LE / MC	LE / MC	LE / MC	LE / MC
Calc. Type		Gravity Loading	Gravity Loading	Gravity Loading	Gravity Loading	Gravity Loading
E_{50}^{ref}	[kN/m²]	1.80E+04	1.80E+04	1.80E+04	1.80E+04	1.80E+04
E_{ur}^{ref}	[kN/m²]	5.39E+04	5.39E+04	5.39E+04	5.39E+04	5.39E+04
ν	[-]	0.3	0.3	0.3	0.3	0.3
φ	[°]	37.3	37.3	37.3	37.3	37.3
c	[kN/m²]	0.01	0.01	0.01	0.01	0.01
ψ	[°]	12.4	12.4	12.4	12.4	12.4
σ_t	[kN/m²]	0.0	1.0	5.0	10.0	100.0
m	[-]	0.5	0.5	0.5	0.5	0.5
p_{ref}	[kN/m²]	100	100	100	100	100
R_f	[-]	0.9	0.9	0.9	0.9	0.9
G_0/G_{ur}	[-]	1	1	1	1	1
$\gamma_{0.7}$	[-]	1.30E-04	1.30E-04	1.30E-04	1.30E-04	1.30E-04
Model SW		1	1	1	1	1
Skempton		0.98	0.98	0.98	0.98	0.98
ε_{tol}	[-]	0.01	0.01	0.01	0.01	0.01
FoS	[-]	1.00	1.01	1.02	1.02	1.02

Apart from the assumptions and problems discussed above one more matter needs to be addressed. During the safety analysis, sometimes the criterion of maximal number of plastic points has not been achieved. To mitigate this, the *incremental multiplier* M_{sf} was lowered from 0.1 (default) to 0.01. In the course of this a parameter study is done to clarify its influence on the FoS (see chapter 5.5).

5.3.3 Results of slope inclination at failure

Fig. 35 gives the slope inclination at failure related to the effective friction angle depending on the dilatancy angle. There, results of different computations are compared. Those are computed with Plaxis 2D, the theory of direct shear mechanism (Equ. (68) and Equ. (69)) and the classical derivation (Equ. (64)).

Comparing Fig. 35 (a) to (d) it gets clear, that the flow rule and the dilatancy angle play an important role. Because the lower the dilatancy the higher the required angle of friction. For example, if a slope inclination of 40° is given and a cohesionless material with $\psi = \varphi/3$ is considered, a friction angle of 43.4° (MC-Plaxis) is required. On the contrary, if the dilatancy reduces to $\psi = \varphi/4$ the effective friction angle should be at least 44.4° (MC-Plaxis) (see Fig. 36 (a)). Those friction angles change to an even lower magnitude once the Matsuoka-Nakai failure criterion is taken into account. This means, that the necessary friction angle for a slope inclination of 40° reduces to 39.0° (for $\psi = \varphi/3$) and 40.9° (for $\psi = \varphi/4$) (see Fig. 36 (b)).

A further detail might be worth to mention is the tendency of the MC-Plaxis-curve. It seems that the corresponding limit friction angle at low slope inclinations tends to converge more with the computation of Equ. (68), i.e. MC-DSS [5]. But if the slope gets steeper, the limit friction angle moves closer to that of Equ. (69), i.e. MN-DSS [5]. Of course the equations Equ. (68) and Equ. (69) do not consider a real failure mechanism, but are valid for infinite slopes and are highlighted in Fig. 37.

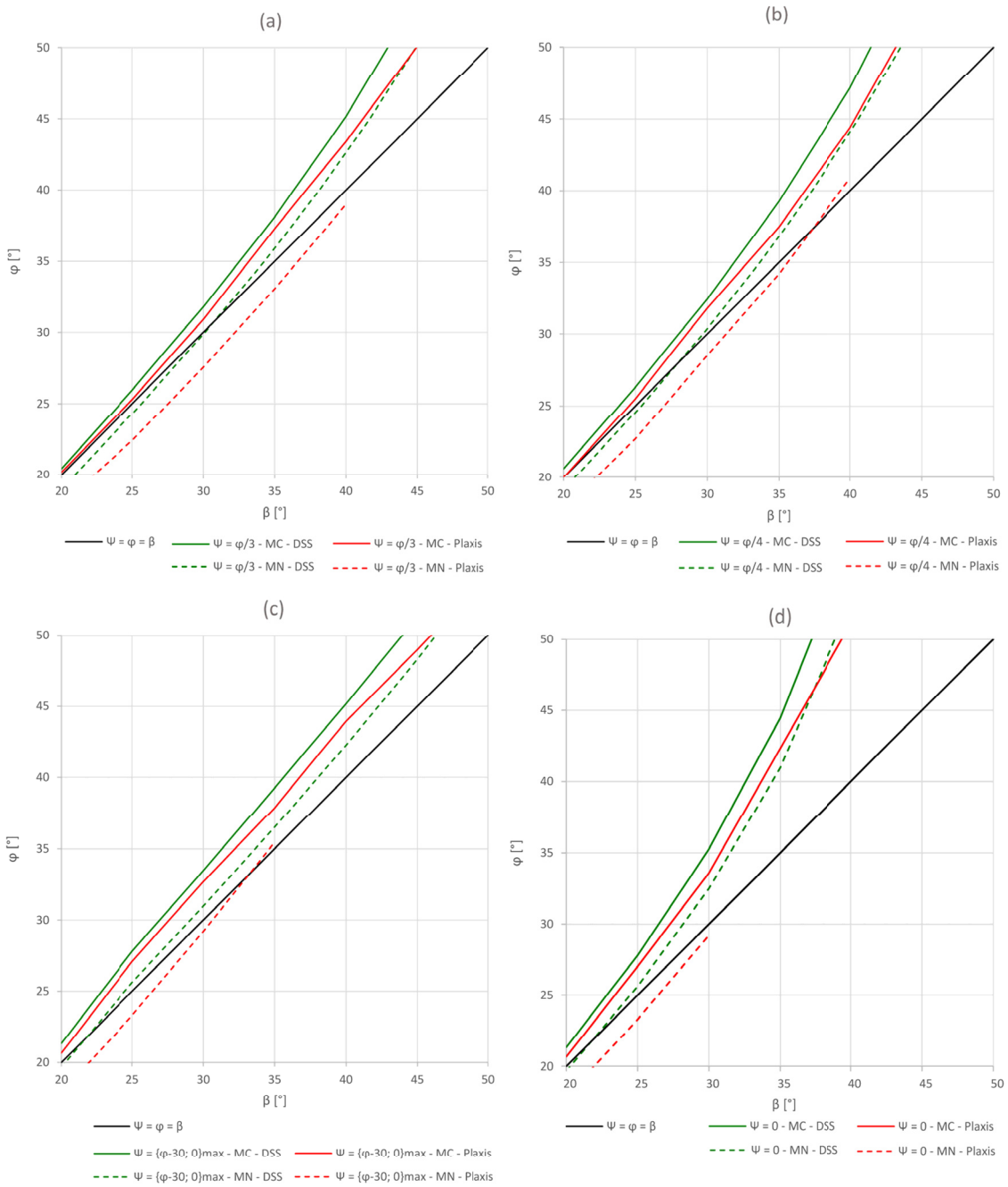

Fig. 35 Comparison of limit states for different computations and dilatancy angles - (a): $\psi = \varphi/3$; (b): $\psi = \varphi/4$; (c): $\psi = \varphi - 30°$; (d): $\psi = 0°$

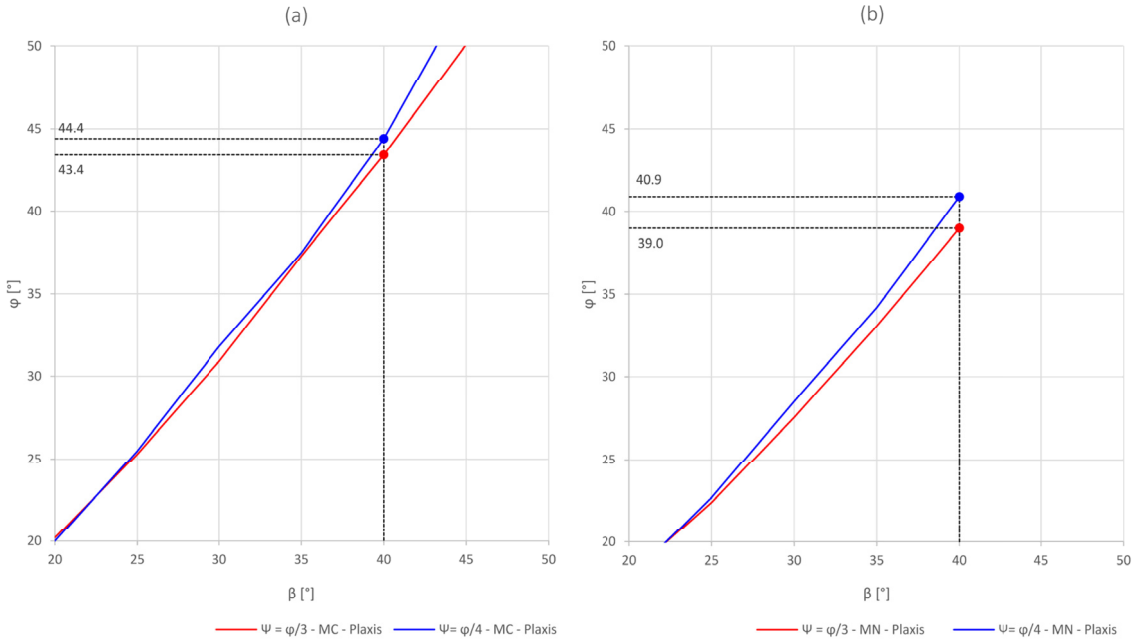

Fig. 36 friction angle at failure for $\beta = 40°$, $\psi = \varphi/3$ and $\psi = \varphi/4$ with MC (a) and MN (b)

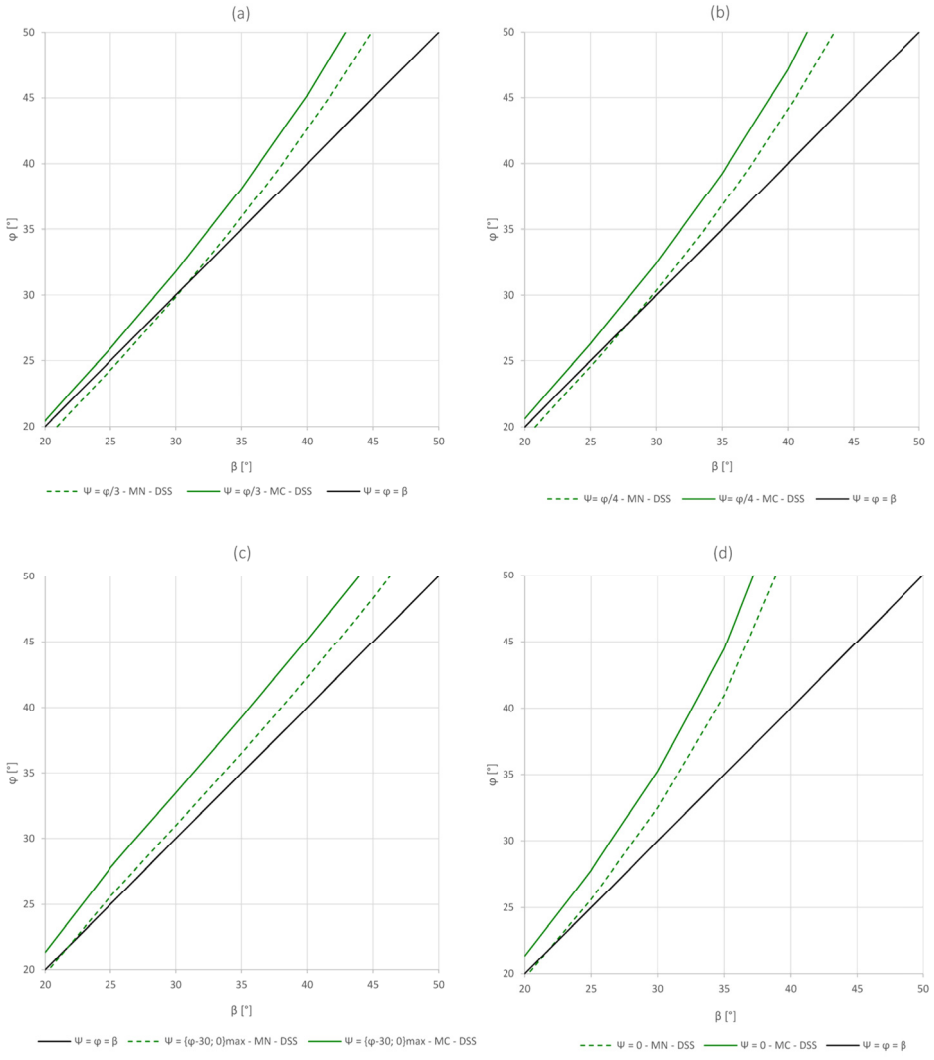

Fig. 37 Comparison of limit states for MC-DSS and MN-DSS with: (a): $\psi = \varphi/3$; (b): $\psi = \varphi/4$; (c): $\psi = \varphi - 30°$; (d): $\psi = 0°$ [5]

Regarding the comparison between MC-Plaxis and MN-Plaxis it seems that the divergence grows the more the dilatancy angle deviates from the friction angle. Observing a dilatancy angle of $\psi = \varphi/3$ it can be identified that the friction angle obtained with MN-Plaxis is about 10 % to 11 % lower than with MC-Plaxis. However, with $\psi = 0°$ the difference is around 13 %. Tab. 2 lists the percentage difference between the MC criterion and the MN criterion dependent on the dilatancy angle and the slope inclination.

Tab. 2 Percentage difference of the FoS between MC and MN

$\Delta FoS = 100 \cdot (FoS_{MC} - FoS_{MN})/FoS_{MC}$ [%]				
β [°]	$\psi = \varphi/3$ [°]	$\psi = \varphi/4$ [°]	$\psi = \varphi - 30°$ [°]	$\psi = 0°$ [°]
20	10.89	11.00	13.40	13.40
25	11.46	10.98	13.94	13.77
30	10.87	10.38	10.70	13.09
35	11.34	8.80	6.41	-
40	10.18	7.88	-	-

Finally it appears, that in some circumstances the Matsuoka-Nakai allows even steeper slopes as those considering an associated flow rule. Provided that the slope angle do not exceed ~35°. Appendix D contains a full comparison of the results as well as the evaluation of the percentage difference between MC and MN.

5.4 Effect of tolerated error

As mentioned above the *tolerated error* ε_{tol} is reduced in the MN-LE analysis. The influence of ε_{tol} on the FoS is studied in the following (using MC-STD). The slope has an inclination of 35°. The corresponding strength parameters are assumed with $\varphi = 40°$ and $\psi = \varphi/3 = 13.3°$ and c = 0 kN/m². Whereas ε_{tol} is varied from 0.001 % to 5 % as listed in Tab. 3. Fig. 38 shows a noticeable decrease in the FoS combined with an increase in the accuracy. But with respect to the oscillations no trend can be seen.

Tab. 3 Parameters of several trails analysing the effect of tolerated error (MC-STD)

Parameter \ Trial		1	2	3	4	5
Plaxis Model		MC - STD	MC - STD	MC - STD	MC - STD	MC - STD
Material Model		MC	MC	MC	MC	MC
Calc. Type		Gravity Loading	Gravity Loading	Gravity Loading	Gravity Loading	Gravity Loading
E'	[kN/m²]	4.00E+04	4.00E+04	4.00E+04	4.00E+04	4.00E+04
E_{oed}	[kN/m²]	5.39E+04	5.39E+04	5.39E+04	5.39E+04	5.39E+04
ν	[-]	0.3	0.3	0.3	0.3	0.3
φ	[°]	40.0	40.0	40.0	40.0	40.0
c	[kN/m²]	0	0	0	0	0
ψ	[°]	13.3	13.3	13.3	13.3	13.3
σ_t	[kN/m²]	0	0	0	0	0
ε_{tol}	[-]	0.05	0.01	0.001	0.0001	0.00001
FoS	[-]	1.15	1.13	1.07	1.03	1.01

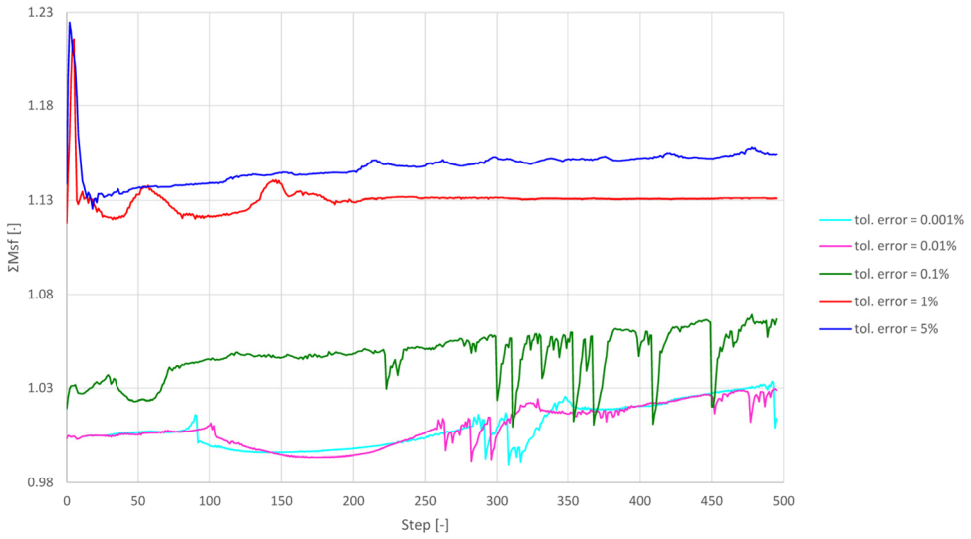

Fig. 38 FoS over steps depending on the tolerated error (MC-STD)

5.4.1 Influence of ε_{tol} using different constitutive models

Further investigations are made on slopes (γ_{unsat} = 17 kN/m³) considering an inclination of 23°, 27° and 30°. On the one hand a cohesionless soil is considered and on the other hand a cohesion of c = 5 kN/m² is applied. The friction angle is adjusted so that a factor of safety of FoS ≅ 1.05 is achieved for the 30° inclined slope. The used material sets are given in Tab. 4. At the other two slope inclinations (23° and 27°), the values of the friction angles are the same as for the 30° inclined slope (see Tab. 4). The analysis is performed to assess the effect of the tolerated error not only on the *elastic-perfectly plastic material model* (MC), but also on other constitutive models such as *Hardening Soil model* (HS) and *Hardening Soil model with Small-strain stiffness* (HSS). All employed parameters associated with the individual material models are given in Appendix C. The results of

the 30° inclined slope are discussed in detail in the following. The calculations of the other two are presented in Appendix C.

In Fig. 39 the charts are captured with (a) and (b), which imply the results considering a cohesion of c = 5 kN/m² and c = 0 kN/m². It could be assumed, that a higher accuracy (low tolerated error) leads to a reduced factor of safety. However, this is not the case for HS and HSS. There the factor of safety at high accuracy is greater than at low accuracy.

In the case of cohesionless material, the differences are even more striking as evident from the right column in Fig. 39. The factor of safety decreases with decreasing tolerated error, but once the cohesion vanishes the results are strongly erratic. The difference at step 100 between $\varepsilon_{tol} = 0.01$ and $\varepsilon_{tol} = 0.001$ and 0.0001 are about 6 %. The percentage difference of the factor of safety is computed with:

$$\Delta FoS = \left| FoS_i - FoS_j \right| \cdot 100 \qquad (74)$$

When comparing the factor of safety based on the HS model it seems that the FoS computed with $\varepsilon_{tol} = 0.001$ or $\varepsilon_{tol} = 0.0001$ is greater than a FoS computed with a lower accuracy (~ 4 %). The difference according the HSS model is around 4 % too, however, the factor of safety with $\varepsilon_{tol} = 0.0001$ is lower compared to $\varepsilon_{tol} = 0.01$.

Fig. 40 highlights the differences of a cohesive soil between the constitutive models for (c): $\varepsilon_{tol} = 0.02$ and (d): $\varepsilon_{tol} = 0.001$. The FoS is lower with the application of MC than with HS and HSS. It seems, that this difference gets more significant as ε_{tol} decreases.

Related to these findings it could be concluded that the tolerated error has an influence on the factor of safety and the erratic nature of the solution. Nevertheless, no trend could be found, thus further investigations are necessary to give a general recommendation.

Tab. 4 Strength parameters for cohesionless and cohesive material

Parameter	Cohesionless material	Cohesive material	Unit
φ	34.5	21.4	[°]
ψ	0	0	[°]
c	0	5	[kN/m²]

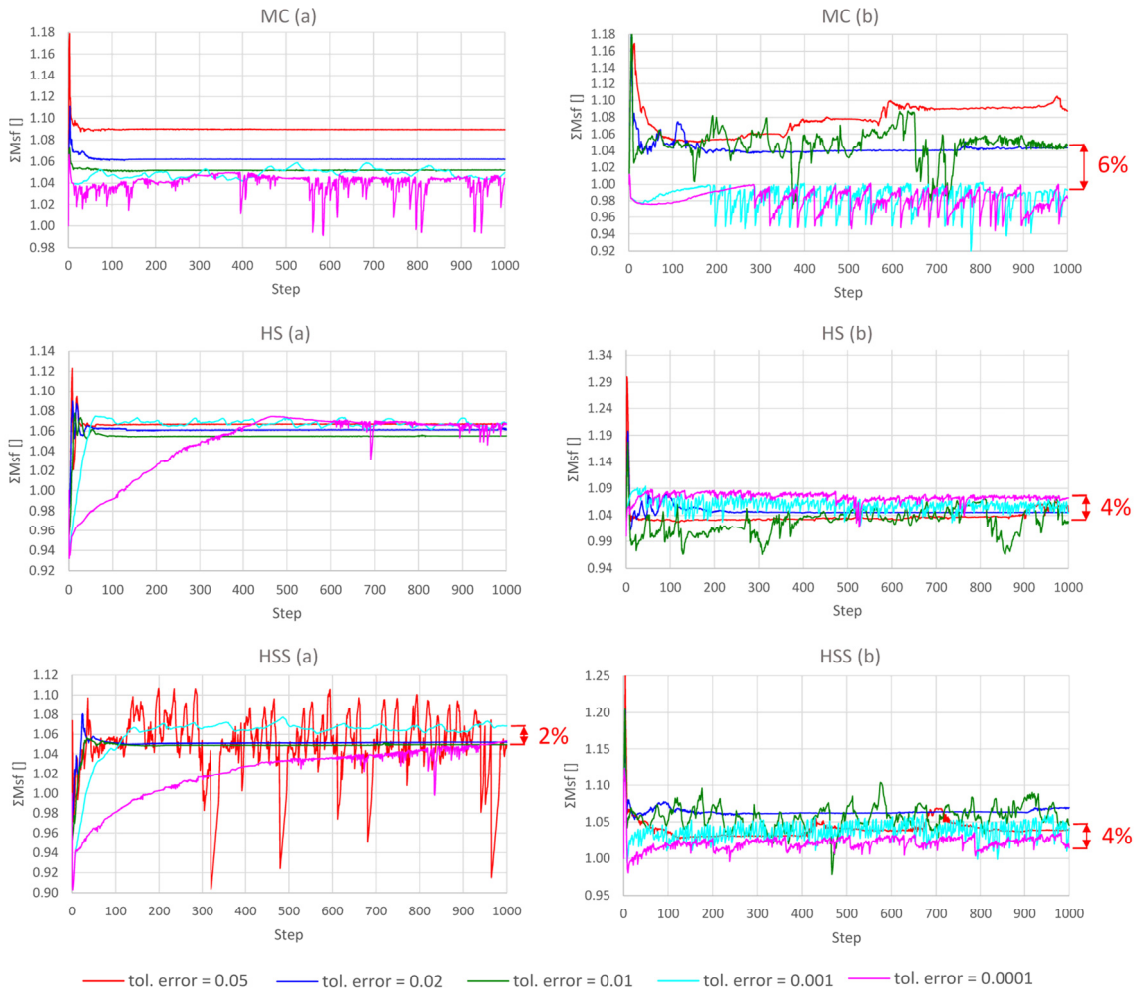

Fig. 39 Effect of tolerated error on FoS - (a): c = 5 kN/m²; (b): c = 0 kN/m²

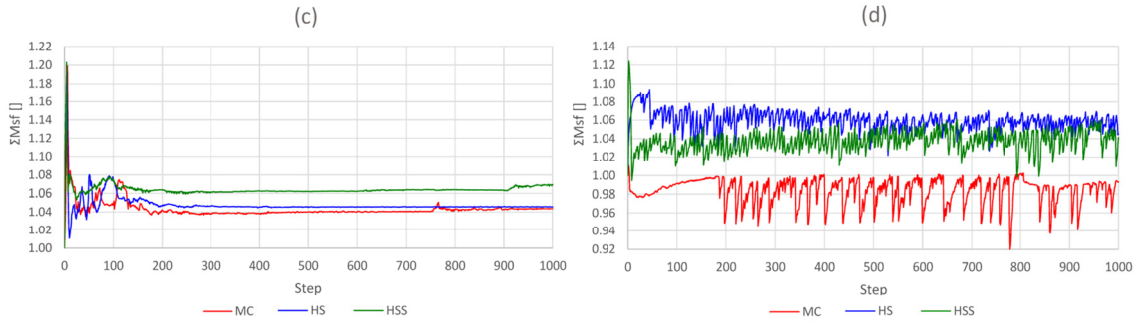

Fig. 40 Comparison of constitutive models for c = 0 kN/m² - (c): $\varepsilon_{tol} = 0.02$; (d): $\varepsilon_{tol} = 0.001$

5.4.2 Investigation of the failure mechanism

The impact of the tolerated error on the incremental deviatoric strain is investigated in this chapter. For this reason a model based on [32] is chosen (which shows a highly erratic behaviour). The slope has a height of 10 m and an inclination of 45°. The mesh is generated with 1160 15-noded triangles. Again drained conditions are assumed, including a material with $\varphi = 45°$, c = 6 kN/m² and $\psi = 0°$. Fig. 41 plots the FoS over calculation steps conducted in Plaxis 2D. The incremental deviatoric strain is illustrated

at step 500 and step 1000. Apparently, the lower the tolerated error the stronger the erratic behaviour of the FoS.

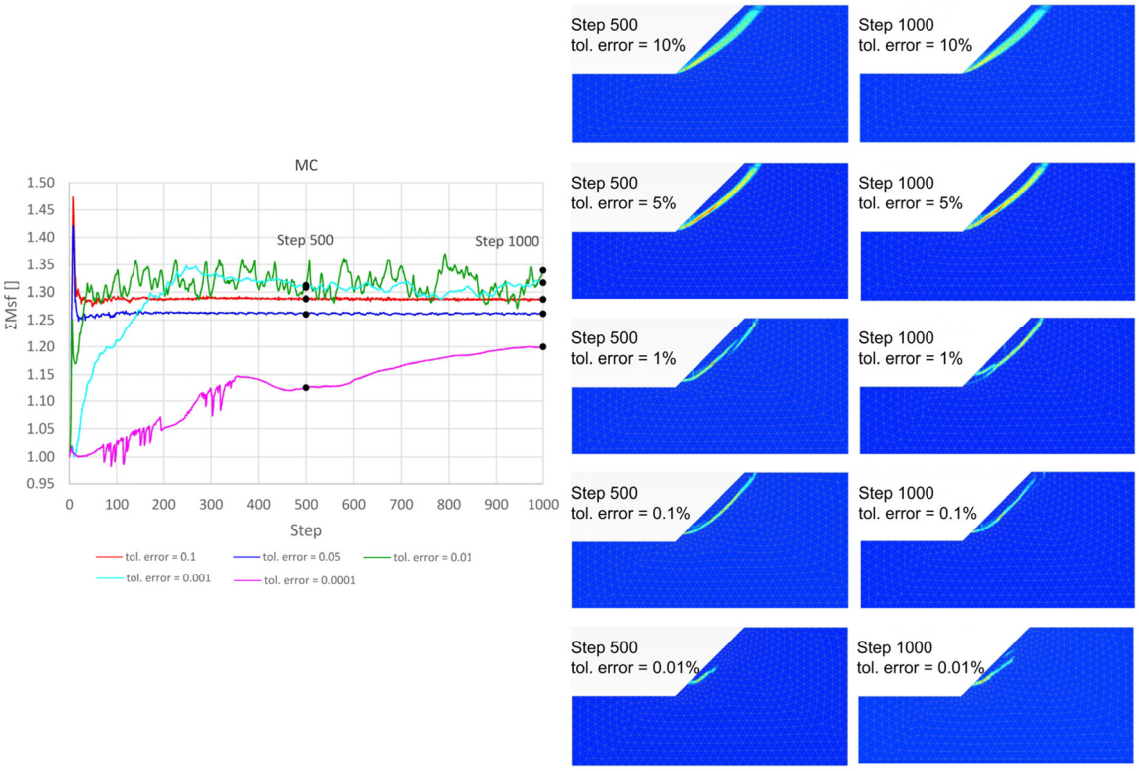

Fig. 41 FoS and incremental deviatoric strain depending on the tolerated error

Another point of concern is to show the occurrence of the erratic nature, even if the strength reduction method is performed by means of a manual iteration. Therefore, a FEA is computed with an initial phase (including *Gravity loading*) followed by a plastic nil-step. The "strength" parameters (φ_{input}, c_{input} and ψ_{input}) are reduced stepwise until no admissible stress state is found in the plastic phase.

Fig. 42 provides an overview on the incremental deviatoric strain for varying tolerated errors (0.01 % - 10 %). On the left side the results are based on a *strength reduction finite-element analysis* (SRFEA) whereas the results on the right side are obtained with the aid of an iterative strength reduction. In particular for high accuracy the erratic nature gets visible.

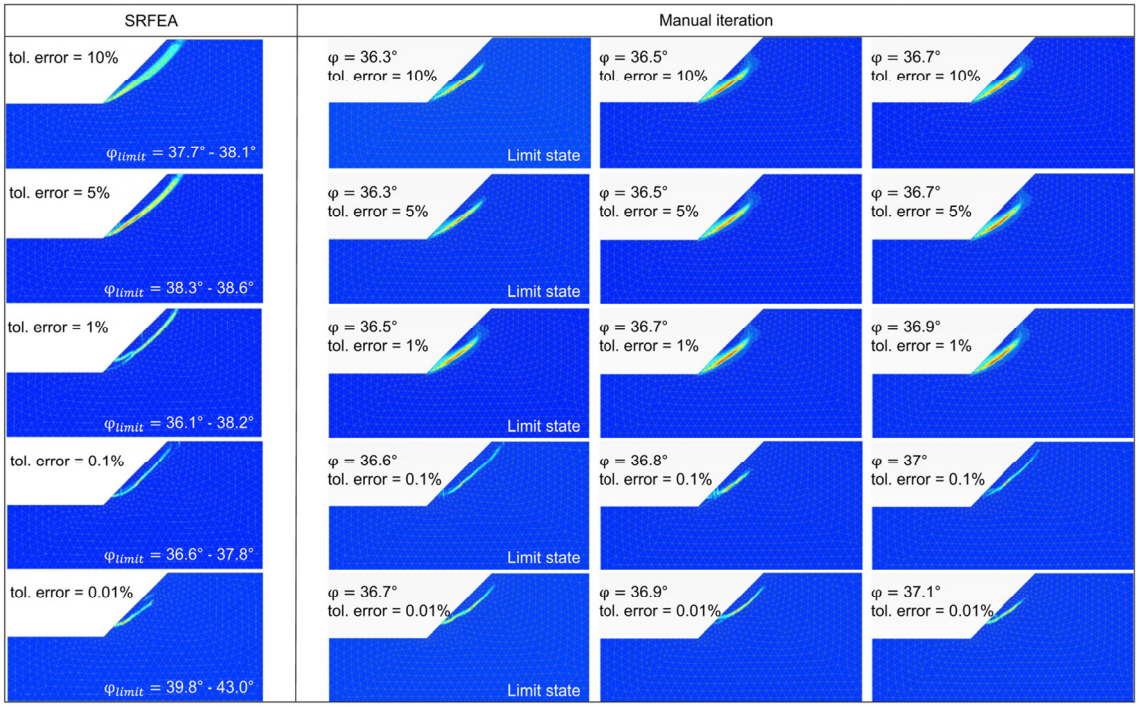

Fig. 42 Incremental deviatoric strain at limit state - manual iteration

5.5 Effect of incremental multiplier M_{sf}

Additionally the effect of the *incremental multiplier* M_{sf} is studied on a 30° inclined slope as described in the previous chapter (same model as in chapter 5.4.1).

As shown left in Fig. 43 the factor of safety is not affected by the magnitude of M_{sf}. A lower M_{sf} leads to a lower increment of the strength reduction of the first calculation step [44]. Therefore, the peak in the first calculation step is less pronounced. Due to a cohesion of c = 5 kN/m² and a “moderate” slope inclination, the FoS is quite constant over iteration steps. In contrast to a cohesionless soil, where the factor of safety highly oscillates. There, it seems that the application of the HS and HSS model gives smaller factors of safety as the cohesion tends to zero.

Fig. 44 highlights the differences between the constitutive models for (c): M_{sf} = 0.1 and (d): M_{sf} = 0.005. A comparison of MC with HS and HSS do not indicate a specific trend.

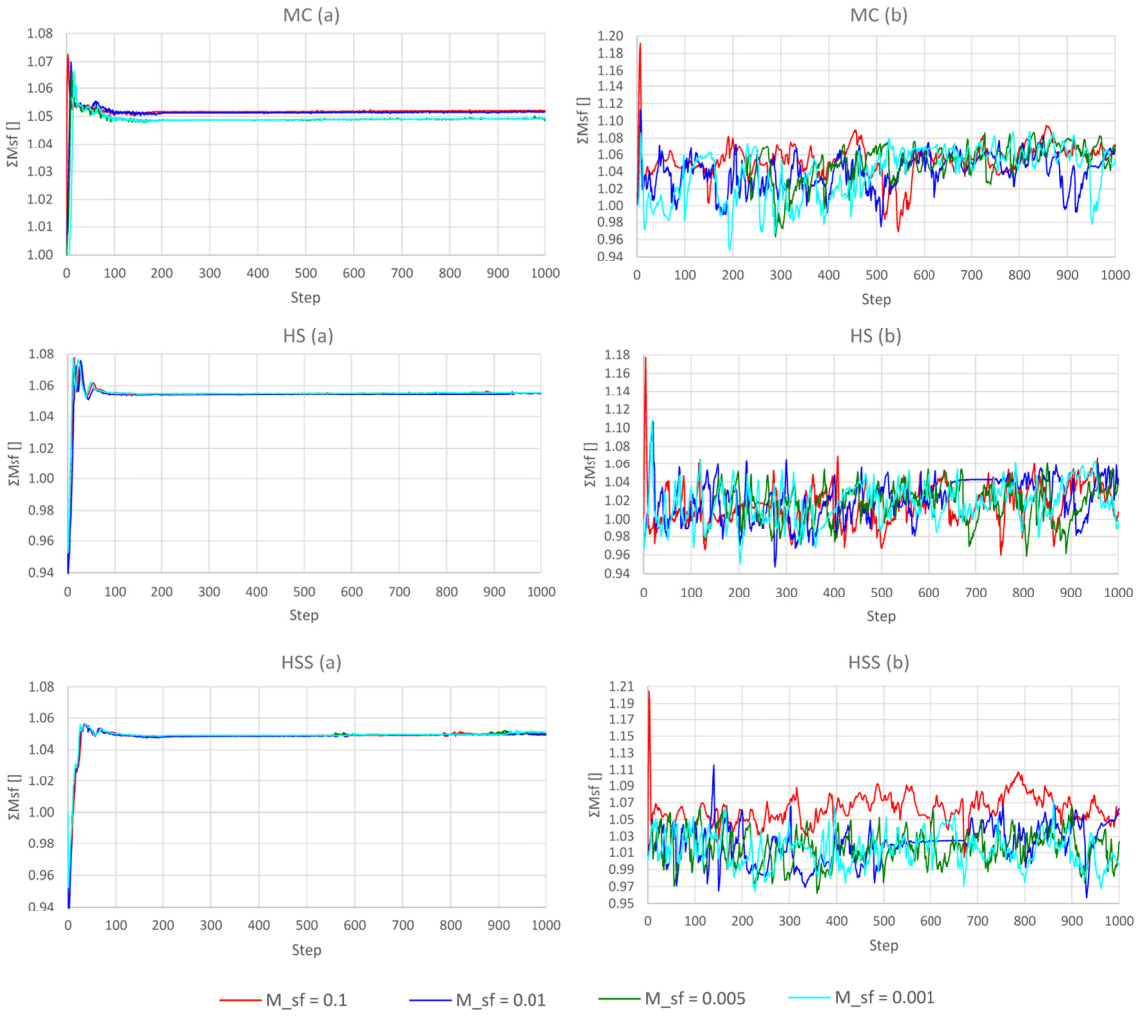

Fig. 43 Effect of incremental multiplier on FoS - (a): c = 5 kN/m²; (b): c = 0 kN/m²

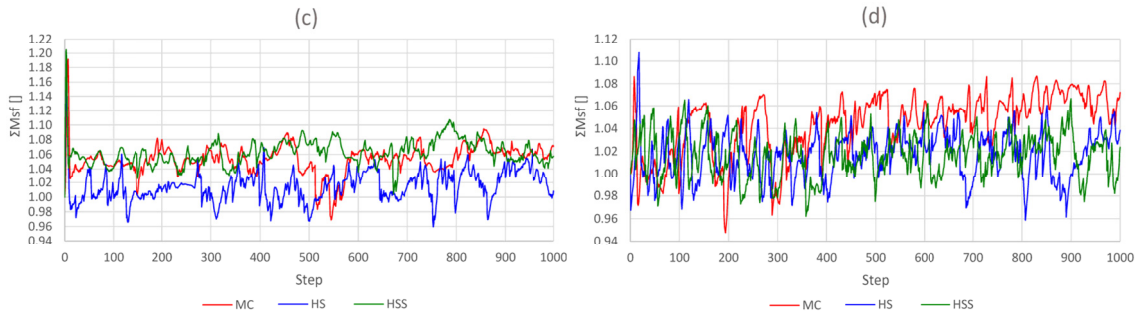

Fig. 44 Comparison of constitutive models for c = 0 kN/m² - (c): M_{sf} = 0.1; (d): M_{sf} = 0.005

5.6 Stress paths development during φ-c-reduction

This chapter deals with the development of stresses during a φ-c-reduction. Selected stress points are investigated in a MS Excel worksheet. The stress paths are plotted in the deviatoric plane (π-plane), as well as in the p-q-space. The development of the stress path has been generated with the aid of the *SoilTest* option in Plaxis 2D and is reported in Appendix G.

Additionally, the difference between MN and MC is discussed by a *normalised principal deviatoric stress deviation* Δq. Which is the normalised difference between the *maximum deviatoric stresses of the Matsuoka-Nakai failure criterion* q_{MN} and *the Mohr-Coulomb failure crit*erion q_{MC} with:

$$\Delta q = \frac{(q_{MN} - q_{MC})}{p} \cdot 100 \qquad (75)$$

In this context the illustration presented in chapter 2.3.2 can be adapted to Δq (see Fig. 45). Fig. 45 gives the Δq (based on the modified equation proposed in Appendix A) at different values of cohesion and a corresponding friction angle of 25°. It has to be noted, that the modified equation includes difficulties in the generation of the yield surface at low stress states. Further investigations are needed to determine the problem.

Additional illustrations including selected friction angles between 20° and 45° are reported in Appendix B. It seems that Δq increases with increasing strength parameters namely φ and c (compare Appendix B).

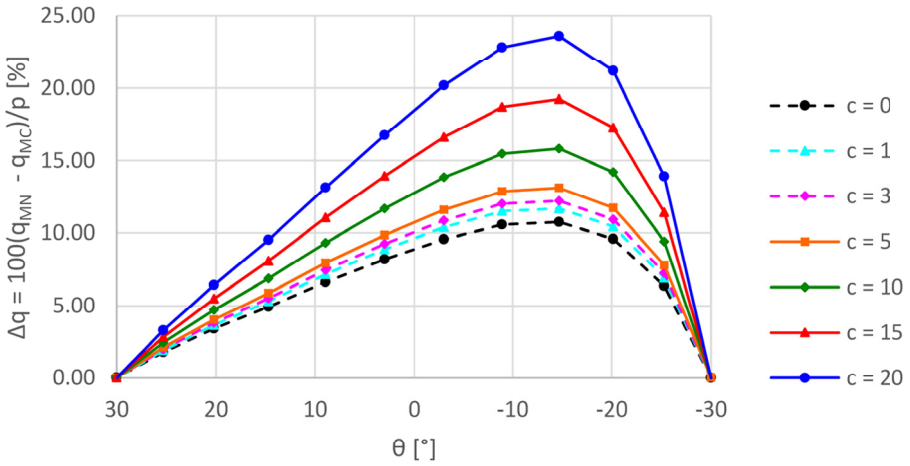

Fig. 45 Determination of Δq with varying cohesion at $\varphi = 25°$

First of all, a brief introduction to the structural set-up of the plots below is given in the following. The stress path of a certain stress point is drawn in the π-plane (see Fig. 46). The blue arrows display the stress path in the initial phase, whereas the red arrows belong to the *Safety phase*. The yield surface drawn in solid lines displays the surface at *maximum principal isotropic effective stress* p_{max}. On the other side, the yield surface drawn with dashed lines shows the surface at the last calculation step (after φ-c-reduction). If the last step (step 1000) hits the yield surface the current stress point is a plastic point, otherwise it is elastic. The present example (Fig. 46) shows a stress state which plasticize under consideration of the MN failure criterion. Fig. 47 illustrates the

stress path in a p-q space at the previously selected step (current step = step 1000). The yield surfaces at a specific lode angle are reduced to a line (MC = black, MN = green). The corresponding π-plane is perpendicular to the principal isotropic effective stress axes (p') as indicated in the figure.

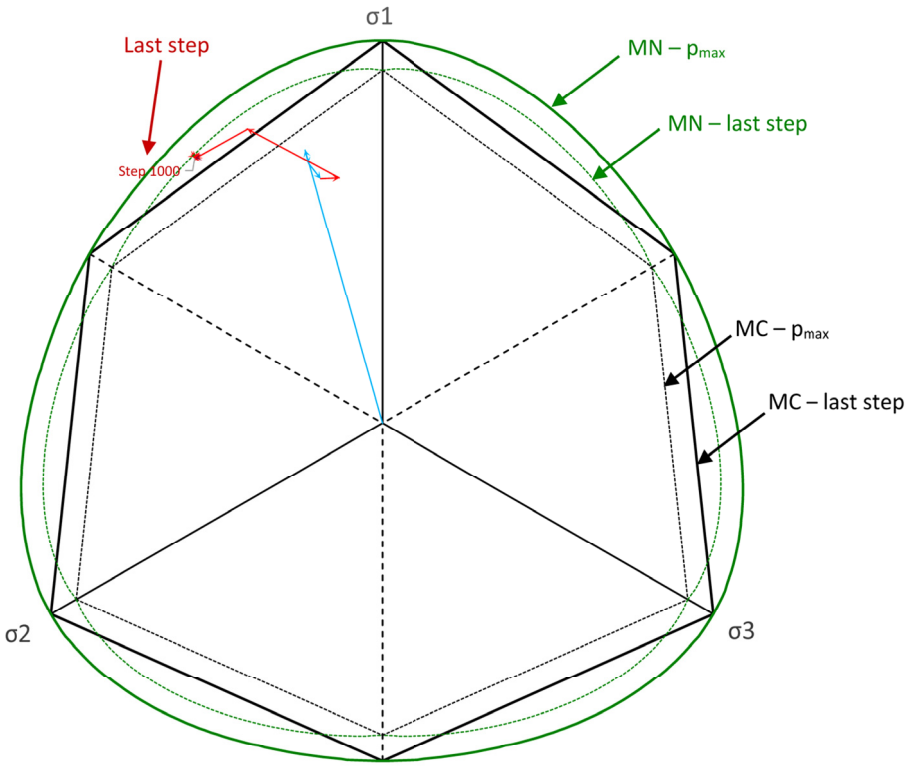

Fig. 46 Introduction of the π-plane

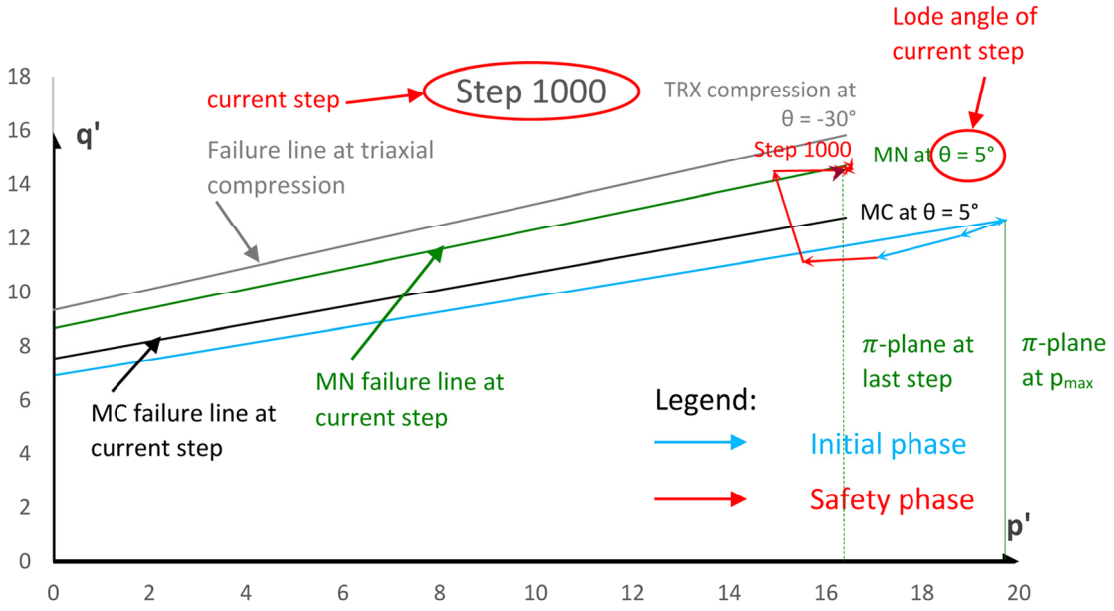

Fig. 47 Introduction of the p-q-space

In the following, different slopes are studied using various material models. The development of θ over steps as well as the stress path tendency are discussed. In a last example the factor of safety between both failure criteria is compared.

5.6.1 Example 1

Example 1 is a 35° inclined slope with two separated material sets. Material set 1 uses the friction angle at failure under consideration of a MC failure criterion, so that $\varphi = \varphi_{MC,limit}$ and $\psi = \varphi_{MC,limit}/3$. Material set 2 gives the required parameters at ultimate limit state with a MN failure criterion ($\varphi = \varphi_{MN,limit}$ and $\psi = \varphi_{MN,limit}/3$ (see Tab. 5)). Any results presented below are related to a specific stress point SP 20145 (Fig. 48 indicates its position). Results of additional stress points are reported in Appendix H.

First, the stress path obtained with material set 1 is analysed, by means of MC-STD and MC-STD-associated. For the latter, an associated flow rule is considered (i.e. $\varphi = \psi = 37.3°$). Afterwards the user-defined material model is used, where MC-LE and MN-LE calculations have been performed. Hence, for MN-LE a factor of safety greater than one is reached. In order to investigate the stress path at failure when MN is used, material set 2 is introduced. Afterwards, the corresponding lode angles are summarized.

Tab. 5 Material set – example 1

Parameter	Material set 1	Material set 2	Unit
φ	37.3	33.1	[°]
ψ	12.4	11.0	[°]
c	0	0.01	[kN/m²]

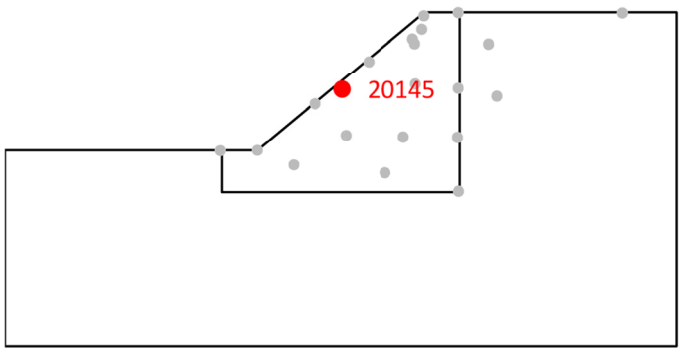

Fig. 48 Position of SP 20145 (schematic representation)

- **MC-STD**

Fig. 49 contains the zone of plasticity (left) as well as the incremental deviatoric strain (right) derived by the computation with MC-STD.

Tab. 6 indicates the stress state at several steps calculated with the material set MC-STD. The grey-shaded fields present the initial phase (*Gravity loading*). The fields with orange background relate to the *Safety phase* (by means of strength reduction). During the calculation the lode angle stays fairly constant with θ = -21°.

In Fig. 50 (left) the deviatoric plane is plotted with the MC-hexagon and the circumscribing MN yield surface. The table to the right of the deviatoric plane, contains the measured distances between the stress state at the considered calculation step (step 1000) and the yield surfaces. These values are expressed in terms of differences of the principal deviatoric stress. There Δ(MC-Point) = 0.12 kN/m² is close to zero, which verifies that the stress point SP 20145 is a failure point. In the p-q-space it appears that the stress path moves along the MC failure line (Fig. 50 right).

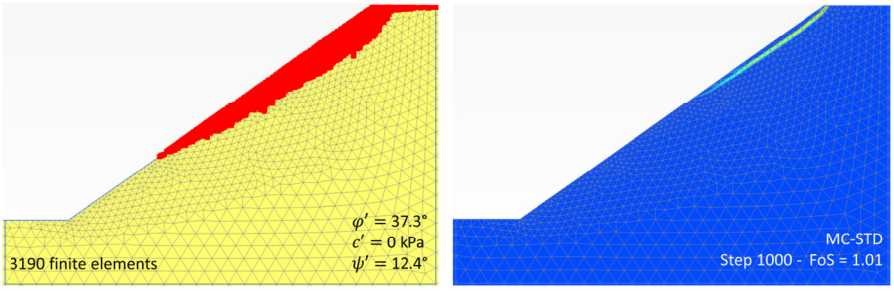

Fig. 49 MC-STD: plasticity zone (left) and incremental deviatoric strain (right)

Tab. 6 Stepwise stress state with MC-STD – SP 20145

Step	σ_1	σ_2	σ_3	p'	q'	φ'	c'	θ
	[kN/m²]	[kN/m²]	[kN/m²]	[kN/m²]	[kN/m²]	[°]	[kPa]	[°]
Step 5	3.05	1.14	0.75	1.65	2.13	37.3	0.00	-20.9
Step 8	7.68	2.87	1.88	4.14	5.37	37.3	0.00	-20.9
Step 11	22.35	8.35	5.48	12.06	15.63	37.3	0.00	-20.9
Step 1	22.15	8.29	5.47	11.97	15.46	37.3	0.00	-20.9
Step 127	16.48	6.28	4.47	9.08	11.22	37.3	0.00	-21.9
Step 253	16.21	6.15	4.30	8.89	11.10	37.3	0.00	-21.7
Step 379	16.39	6.19	4.24	8.94	11.30	37.3	0.00	-21.4
Step 505	15.41	5.77	3.84	8.34	10.73	37.3	0.00	-21.0
Step 631	14.28	5.35	3.56	7.73	9.95	37.3	0.00	-21.0
Step 754	15.33	5.75	3.82	8.30	10.68	37.3	0.00	-21.0
Step 877	15.47	5.80	3.85	8.37	10.78	37.3	0.00	-21.0
Step 1000	18.72	7.02	4.66	10.13	13.04	37.3	0.00	-21.0

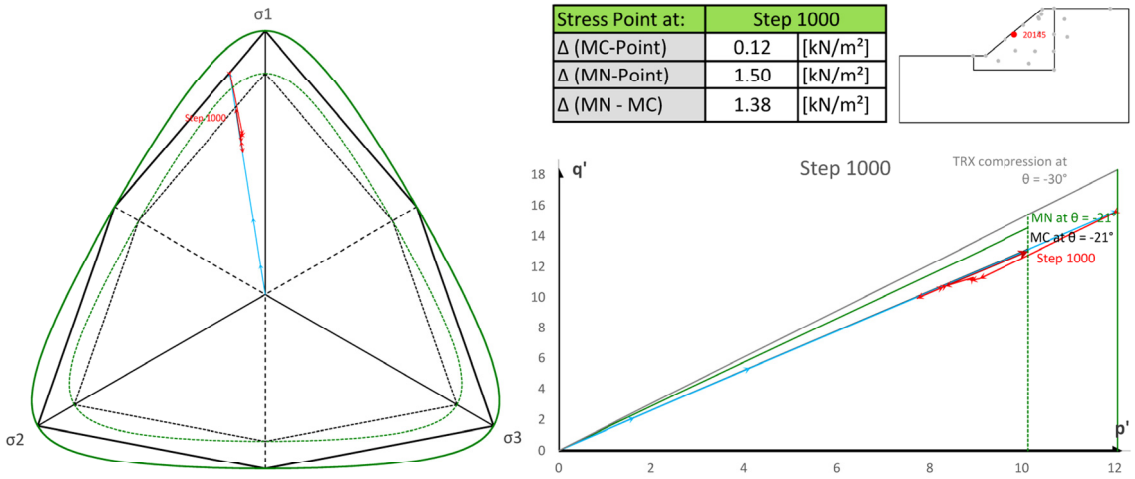

Fig. 50 π-plane (left) and p-q-space (right) with MC-STD – SP 20145

- **MC-STD-associated**

At this FEA the dilatancy angle of material set 1 is replaced by a value equal to the friction angel ($\varphi = \psi = 37.3°$) which results in a factor of safety of FoS = 1.10. Fig. 51 illustrates the obtained plastic zone (left) as well as the incremental deviatoric strain (right). Again stress point SP 20145 is considered, which is definitely inside the zone of plasticity.

Tab. 7 indicates the stress state at several steps calculated with the material set MC-STD-associated. The grey-shaded fields present the initial phase (*Gravity loading*). The fields with orange background relate to the *Safety phase* (by means of strength reduction). During the calculation the lode angle remains fairly constant with θ = -22°. The deviatoric plane illustrated on the left in Fig. 52 shows similar results as obtained with MC-STD. Furthermore, the isotropic stresses at the particular steps are close to those obtained with the MC-STD FEA. But, when looking at the table to the right of Fig. 52, a small increase in the deviatoric stress deviation of 0.63 kN/m² gets obvious. Hence, under the consideration of an associated flow rule, SP 20145 is still an elastic point (do not hit the yield surface).

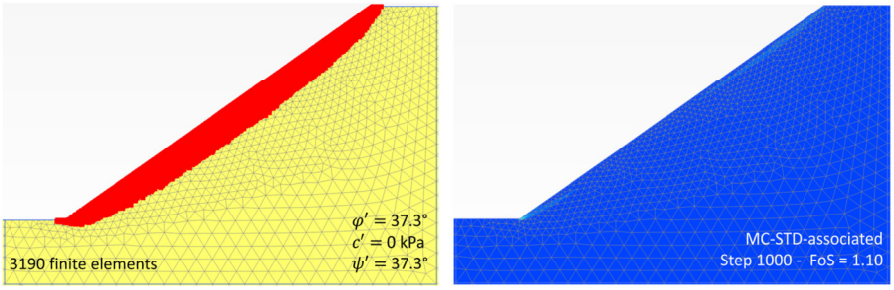

Fig. 51 MC-STD-associated: plasticity zone (left) and incremental deviatoric strain (right)

Tab. 7 Stepwise stress state with MC-STD-associated – SP 20145

Step	σ_1	σ_2	σ_3	p'	q'	φ'	c'	θ
	[kN/m²]	[kN/m²]	[kN/m²]	[kN/m²]	[kN/m²]	[°]	[kPa]	[°]
Step 5	2.45	0.91	0.60	1.32	1.71	37.3	0.00	-20.9
Step 8	9.89	3.70	2.43	5.34	6.92	37.3	0.00	-20.9
Step 11	22.36	8.35	5.49	12.07	15.64	37.3	0.00	-20.9
Step 1	22.28	8.33	5.49	12.03	15.57	37.3	0.00	-20.9
Step 127	18.79	7.18	5.15	10.37	12.75	37.3	0.00	-22.1
Step 253	17.78	6.80	4.87	9.82	12.07	37.3	0.00	-22.1
Step 379	27.47	10.50	7.53	15.16	18.63	37.3	0.00	-22.1
Step 505	17.32	6.62	4.74	9.56	11.75	37.3	0.00	-22.0
Step 631	16.58	6.33	4.53	9.15	11.26	37.3	0.00	-22.0
Step 754	14.21	5.43	3.89	7.84	9.64	37.3	0.00	-22.0
Step 877	15.34	5.86	4.19	8.47	10.42	37.3	0.00	-22.0
Step 1000	12.97	4.95	3.54	7.15	8.80	37.3	0.00	-22.0

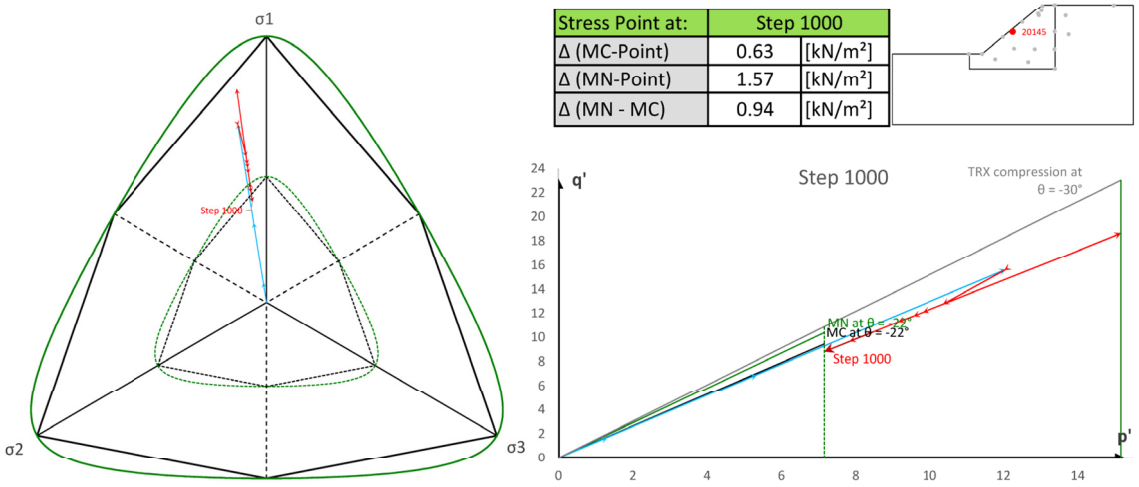

Fig. 52 π-plane (left) and p-q-space (right) with MC-STD-associated – SP 20145

- **MC-LE**

For the following FEA the user-defined material model (*Model Switch* set to 1) has been used. It includes a linear elastic material in the initial phase. Subsequently, a plastic nil-step is introduced where the material is replaced by the MC failure criterion. Again material set 1 is applied, which leads to a factor of safety of FoS = 1.00 where SP 20145 is indicated as a failure point. Fig. 53 displays the zone of plasticity (left) as well as the incremental deviatoric strain (right).

Tab. 8 shows the stress state at several steps calculated with the material set MC-LE. The grey-shaded fields present the plastic phase (plastic nil-step). The fields with orange background relate to the *Safety phase* (by means of strength reduction). The lode angle is alike in the case of MC-STD fairly constant with θ = -21°. It should be emphasised that the high values of the stresses at step 4 result from the initial phase. As mentioned before, the material has been changed from a linear elastic to a linear elastic-perfectly plastic material model including a MC failure criterion. Note, step 4 to 26 (grey-shaded fields in Tab. 8) belong to the plastic nil-step. At the end (step 1000), the isotropic stress is slightly greater as in the models before. This is also shown in the p-q-space representation in Fig. 54. Furthermore, Δ(MC-Point) = 0.12 kN/m² matches with that of MC-STD FEA (see also Fig. 55).

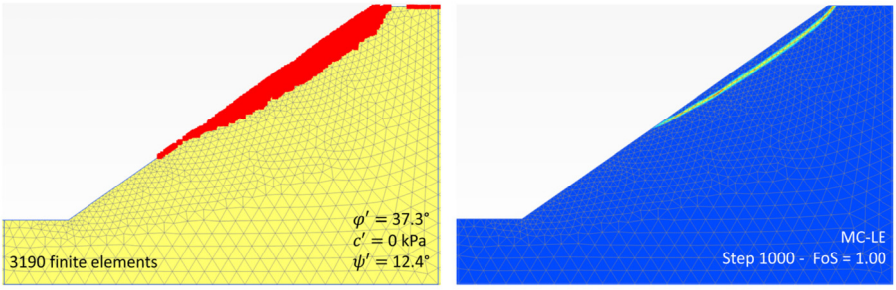

Fig. 53 MC-LE: plasticity zone (left) and incremental deviatoric strain (right)

Tab. 8 Stepwise stress state with MC-LE – SP 20145

Step	σ_1	σ_2	σ_3	p'	q'	φ'	c'	θ
	[kN/m²]	[kN/m²]	[kN/m²]	[kN/m²]	[kN/m²]	[°]	[kPa]	[°]
Step 4	42.66	15.94	10.46	23.02	29.84	37.3	0.00	-20.9
Step 11	34.39	12.85	8.44	18.56	24.05	37.3	0.00	-20.9
Step 26	22.27	8.32	5.46	12.02	15.58	37.3	0.00	-20.9
Step 1	22.02	8.24	5.44	11.90	15.37	37.3	0.00	-20.9
Step 127	15.29	5.99	4.69	8.66	10.02	37.3	0.00	-23.5
Step 253	14.23	5.33	3.54	7.70	9.92	37.3	0.00	-21.0
Step 379	15.97	5.99	4.00	8.66	11.11	37.3	0.00	-21.1
Step 505	16.38	6.13	4.06	8.86	11.43	37.3	0.00	-21.0
Step 631	16.41	6.15	4.10	8.89	11.43	37.3	0.00	-21.0
Step 754	16.31	6.11	4.07	8.83	11.36	37.3	0.00	-21.0
Step 877	16.58	6.22	4.14	8.98	11.54	37.3	0.00	-21.0
Step 1000	17.15	6.43	4.28	9.29	11.94	37.3	0.00	-21.0

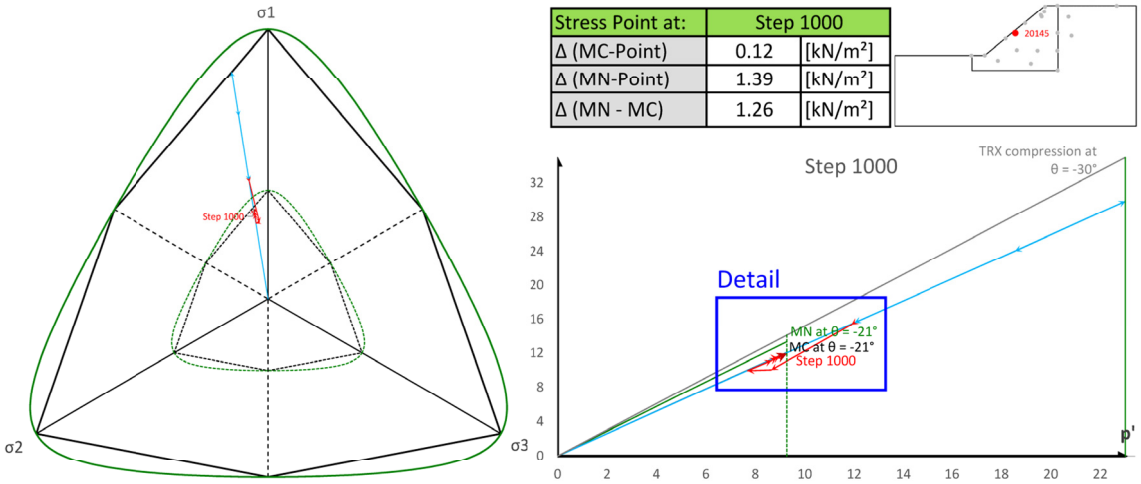

Fig. 54 π-plane (left) and p-q-space (right) with MC-LE – SP 20145

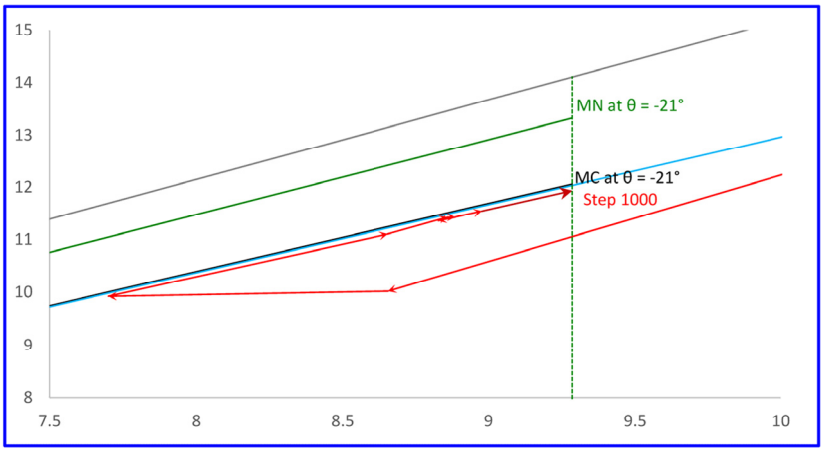

Fig. 55 Detail: MC-LE – SP 20145

- **Comparison of the lode angle using the MC failure criterion**

Fig. 56 underlines the differences in the compared lode angle for each analysis. Additionally the lode angle of MC-GR and MC-K0 are given. For both FEA the user-defined material model has been used (*Model Switch* set to 1). MC-GR considers the calculation type *Gravity loading* including a linear elastic-perfectly plastic material model. MC-K0 uses the K0 procedure in order to compute the initial stresses followed by a plastic nil-step. Finally a φ-c-reduction is performed for all methods.

Calculations performed with the MC failure criterion range between -26.6° $\leq \theta \leq$ -20.9°. Methods using *Gravity loading* show good correlation during the computation of initial stresses. But during the φ-c-reduction some deviations occur. In the final step MC-STD-associated reaches a lode angle of θ = -22°, whereas with MC-GR a lode angle of θ = -21.6° arises. However, there is an exception in the case of using MC-K0. The corresponding lode angle already shows significant discrepancy at the initial phase. Finally θ is about 4.6° smaller than the lode angle derived by MC-STD. In contrast MC-

LE shows a good agreement with MC-STD, which verifies its application on the user-defined material model.

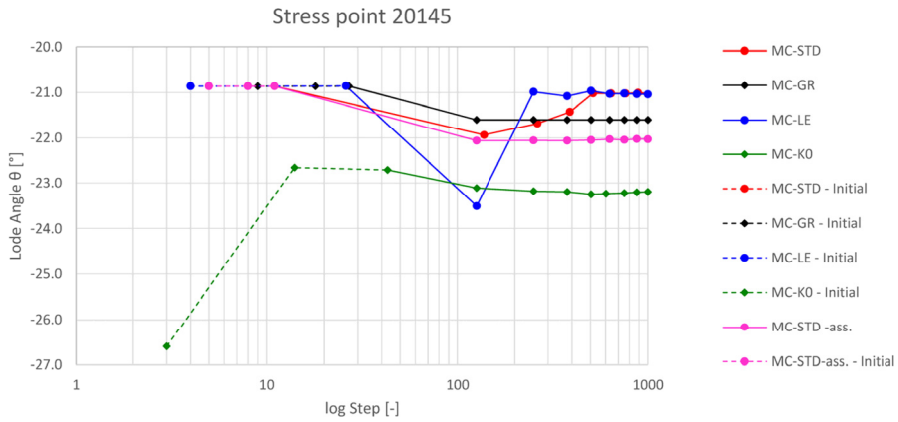

Fig. 56 Lode angle over steps in logarithmic scale considering the MC failure criterion

In the next step, the development of the stress state is analysed applying the MN failure criterion. First the parameters of material set 1 are used, which lead to a factor of safety greater than one. Afterwards, the parameters are changed according to material set 2. Thus a MN failure criterion at limit state is investigated. In order to consider the Matsuoka-Nakai failure criterion, a user-defined material model is applied. Due to the findings discussed before (compare chapter 5.3.2) a linear elastic material is applied and in a second phase the material is changed. This approach has also been validated in chapter 5.6.1, where obtained results with MC show that its application is suitable.

- **MN-LE-M1**

This model uses parameters of material set 1 (M1), which lead to a factor of safety of around FoS = 1.17. The zone of plasticity differs from that obtained with the Mohr-Coulomb failure criterion (compare Fig. 53 with Fig. 57). Fig. 57 provides the zone of plasticity (left) as well as the incremental deviatoric strain (right). The inspected stress point SP 20145 at step 1000 does not reach the yield surface (MN), but is elastic related to a distance of Δ(MN-Point) = 1.02 kN/m² (see Fig. 58).

Tab. 9 indicates the stress state at several steps calculated with the material set MN-LE. The grey-shaded fields present the plastic phase (plastic nil-step). The fields with orange background relate to the *Safety phase* (by means of strength reduction). It appears that the lode angle of each step deviates substantially from the values calculated with the Mohr-Coulomb failure criterion. In the latter phases the lode angle varies between $3.8° \leq \theta \leq 21.8°$. The deviatoric plane presented in Fig. 58 visualizes the lode angle at each step. From the p-q-space it can be seen that the stress state ends close to the MC

yield surface, more precisely with Δ(MC-Point) = 0.36 kN/m². However, SP 20145 is in the elastic region with a distance to the MN yield surface of Δ(MN-Point) = 1.02 kN/m².

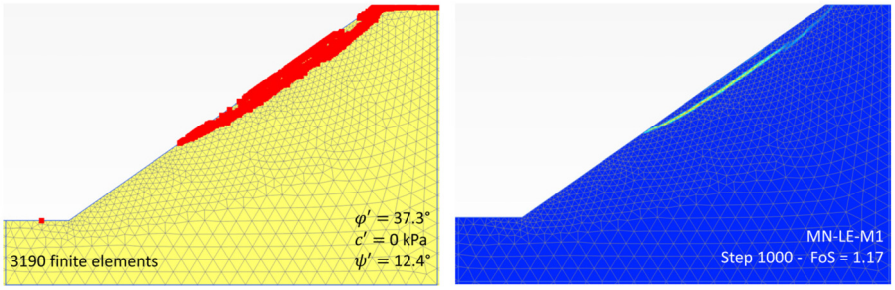

Fig. 57 MN-LE-M1: plasticity zone (left) and incremental deviatoric strain (right)

Tab. 9 Stepwise stress state with MN-LE-M1 – SP 20145

Step	σ_1	σ_2	σ_3	p'	q'	φ'	c'	θ
	[kN/m²]	[kN/m²]	[kN/m²]	[kN/m²]	[kN/m²]	[°]	[kPa]	[°]
Step 5	44.66	17.90	8.66	23.74	32.38	37.3	0.00	-15.7
Step 8	39.54	18.91	7.66	22.04	28.01	37.3	0.00	-9.6
Step 11	29.09	18.67	6.01	17.92	20.02	37.3	0.00	3.2
Step 1	28.57	18.58	5.96	17.70	19.63	37.3	0.00	3.8
Step 127	16.76	14.92	4.77	12.15	11.19	37.3	0.00	21.8
Step 253	15.95	13.83	4.45	11.41	10.60	37.3	0.00	20.0
Step 379	15.85	13.78	4.37	11.33	10.59	37.3	0.00	20.3
Step 505	14.97	11.66	3.99	10.20	9.76	37.3	0.00	12.9
Step 631	15.66	11.10	4.01	10.26	10.17	37.3	0.00	7.1
Step 754	16.04	11.31	4.33	10.56	10.20	37.3	0.00	6.3
Step 877	15.00	10.94	3.88	9.94	9.74	37.3	0.00	8.9
Step 1000	15.23	11.10	4.01	10.11	9.82	37.3	0.00	8.7

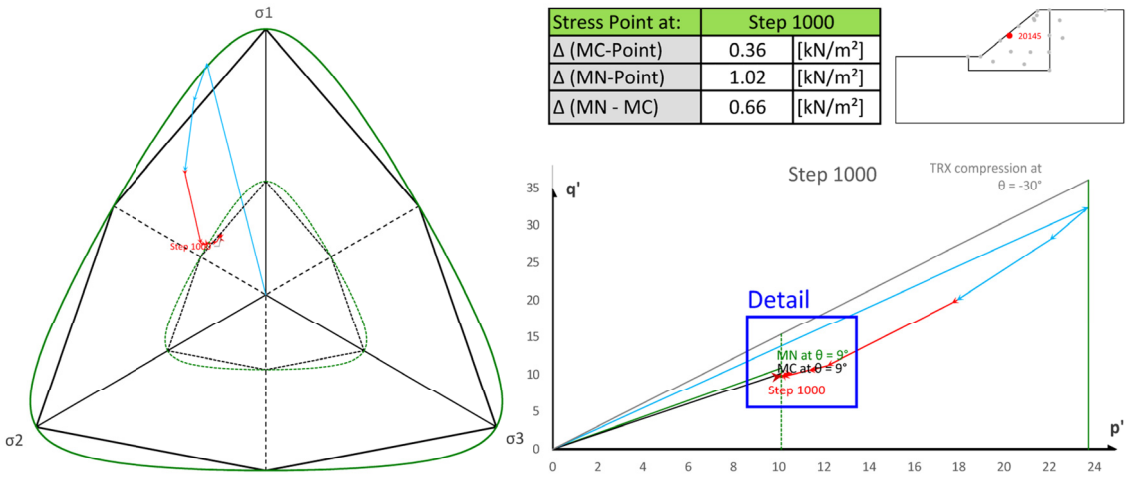

Fig. 58 π-plane (left) and p-q-space (right) with MN-LE-M1 – SP 20145

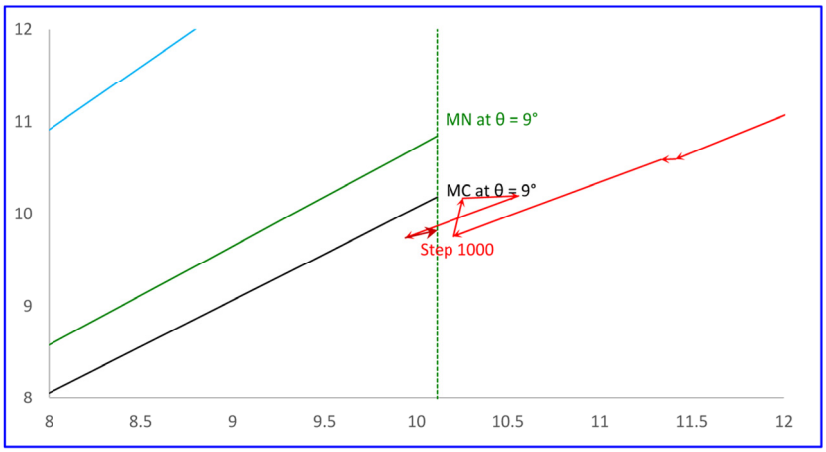

Fig. 59 Detail: MN-LE-M1 – SP 20145

- **MN-LE-M2**

In a second variation the material parameters are changed to material set 2 (M2), so that the factor of safety reduces to FoS = 1.00. All other settings are similar as previously declared. It can be observed in Fig. 60, that the zone of plasticity (left) and the incremental deviatoric strain (right) varies slightly from that, generated with MN-LE-M1. Moreover, it is striking that the principal isotropic effective stress p' as well as the lode angle stay almost constant during the strength reduction procedure (compare Tab. 10 with Fig. 61). At step 1000 the difference between the stress point SP 20145 and the MN yield surface amounts 0.19 kN/m² (see also Fig. 62). From this it can be deduced that SP 20145 is very close to the yield surface, thus almost at failure.

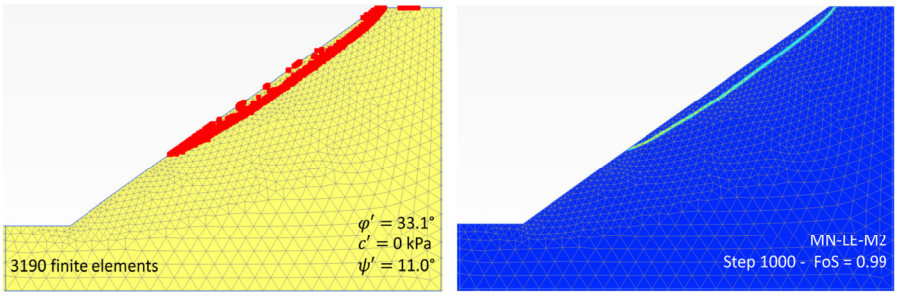

Fig. 60 MN-LE-M2: plasticity zone (left) and incremental deviatoric strain (right)

Tab. 10 Stepwise stress state with MN-LE-M2 – SP 20145

Step	σ_1	σ_2	σ_3	p'	q'	φ'	c'	θ
	[kN/m²]	[kN/m²]	[kN/m²]	[kN/m²]	[kN/m²]	[°]	[kPa]	[°]
Step 3	43.02	19.05	10.24	24.10	29.39	33.1	0.00	-15.0
Step 11	32.74	19.39	7.87	20.00	21.56	33.1	0.00	-2.4
Step 25	19.43	15.01	5.09	13.18	12.72	33.1	0.00	12.5
Step 1	19.23	14.89	5.08	13.07	12.55	33.1	0.00	12.6
Step 127	18.19	14.39	4.99	12.52	11.77	33.1	0.00	13.8
Step 253	18.07	14.36	5.02	12.48	11.65	33.1	0.00	14.0
Step 379	18.06	14.35	5.00	12.47	11.66	33.1	0.00	14.0
Step 505	17.95	14.31	4.97	12.41	11.59	33.1	0.00	14.2
Step 631	18.05	14.35	5.00	12.47	11.64	33.1	0.00	14.0
Step 754	18.10	14.37	5.02	12.50	11.67	33.1	0.00	13.9
Step 877	18.01	14.35	5.04	12.47	11.58	33.1	0.00	14.1
Step 1000	18.28	14.42	5.01	12.57	11.83	33.1	0.00	13.6

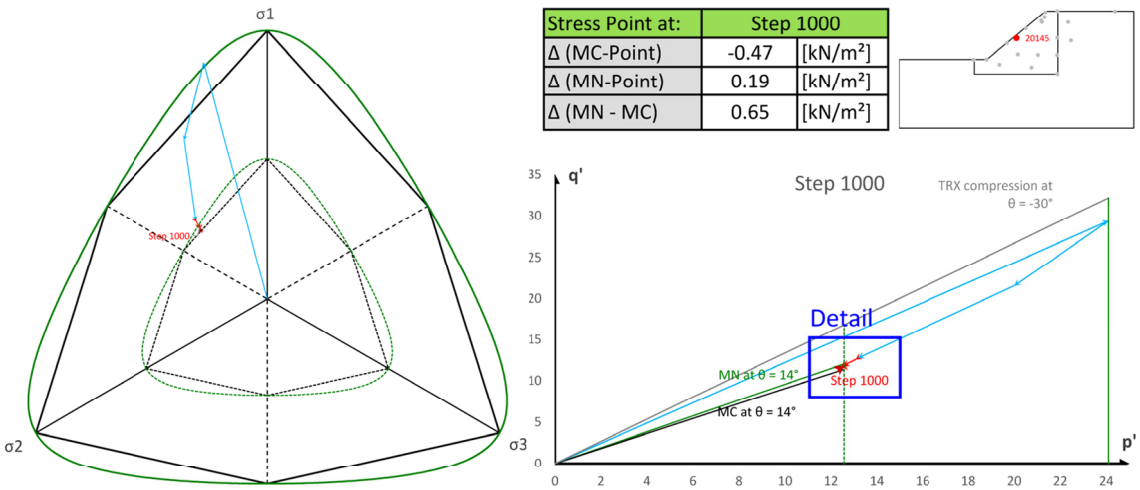

Fig. 61 π-plane (left) and p-q-space (right) with MN-LE-M2 – SP 20145

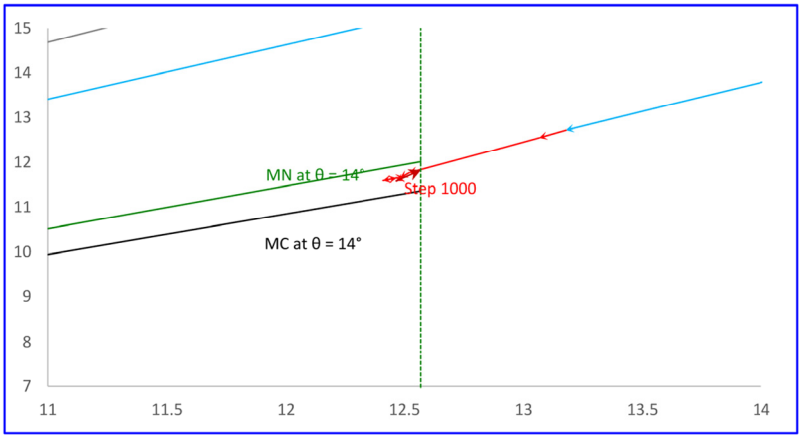

Fig. 62 Detail: MN-LE-M2 – SP 20145

- **Comparison of the lode angle using the MN failure criterion**

Additionally, the lode angle obtained during FEA using the MN failure criterion is summarized in Fig. 63. However, the resulted lode angles range from θ = -15.0° to θ = 21.8°, which are far away from the results detailed in Fig. 56. It should be noted that σ_2 already show a significant increase in the plastic phase, which is a reason for its deviation to MC-LE.

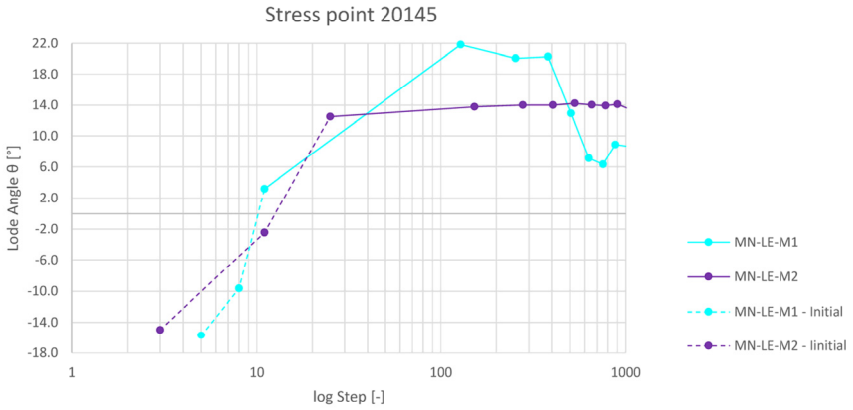

Fig. 63 Lode angle over steps in logarithmic scale considering the MN failure criterion

5.6.2 Example 2

In Example 2 a 20° inclined slope at limit state is analysed, where a cohesive material is considered (Tab. 11). The slope inclination in combination with a cohesion allows a numerical stable calculation which enables the application of *Gravity Loading* on both failure criteria. Therefore, no material change is necessary (see chapter 5.3.2). This allows an evaluation of the differences of MN-GR and MN-LE. Tab. 11 lists the *input parameters* and *limit parameters* based on the failure criterion. However, the dilatancy angle which is stayed constant with:

$$\psi_{limit} = \psi_{input} = \frac{\varphi_{input}}{3} \qquad (76)$$

In the following the stress path of the stress point SP 11725 is discussed. This stress point hits the yield surface in both failure criteria and is situated close to the toe of the slope as displayed in Fig. 64. Additional stress points are displayed in Appendix I.

At the beginning, SP 11725 is inspected using MC-STD. Afterwards the stress path is analysed by applying the user-defined material model with the approaches MN-GR and MN-LE. At the end, the corresponding lode angles are compared.

Tab. 11 Strength parameters – example 2

Parameter	MC	MN	Unit
φ_{input}	23.0	23.0	[°]
ψ_{input}	7.7	7.7	[°]
c_{input}	10.00	10.00	[kN/m²]
φ_{limit}	12.1	10.7	[°]
ψ_{limit}	7.7	7.7	[°]
c_{limit}	5.06	4.45	[kN/m²]

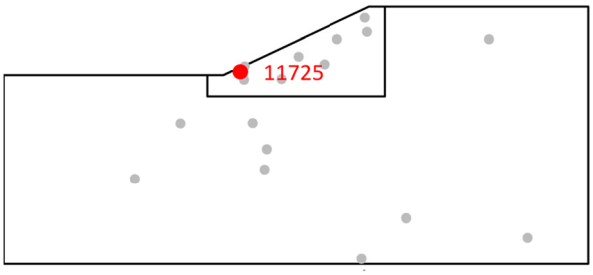

Fig. 64 Position of SP 11725 (schematic representation)

- **MC-STD**

Fig. 65 displays the plastic zone (top) and the incremental deviatoric strain (bottom). Due to cohesion a well-defined slip surface develops. Tab. 12 shows the stress state at several steps arising from the MC-STD calculation. The grey-shaded fields present the initial phase (*Gravity loading*). The orange coloured fields relate to the *Safety phase* (by means of strength reduction).

During the calculation the lode angle develops from θ = -28.6° to θ = -19.6°. Note, there is no significant change to the stresses or the lode angle after step 127 (*Safety phase*). This fact is shown also in Fig. 66 on the left, where the deviatoric plane is illustrated. The rather symmetrical shape of the hexagon results from the ratio between friction angle and cohesion. Theoretically, if φ tends to zero, a regular hexagonal cylinder is obtained which then complies with the Tresca model. Whereas the Matsuoka-Nakai yield surface creates a circle in the deviatoric plane if $\varphi = 0°$ [46]. Obviously, SP 11725 belongs to a failure point as Δ(MC-Point) = 0.03 kN/m². Which is also observable in the p-q-space (Fig. 66).

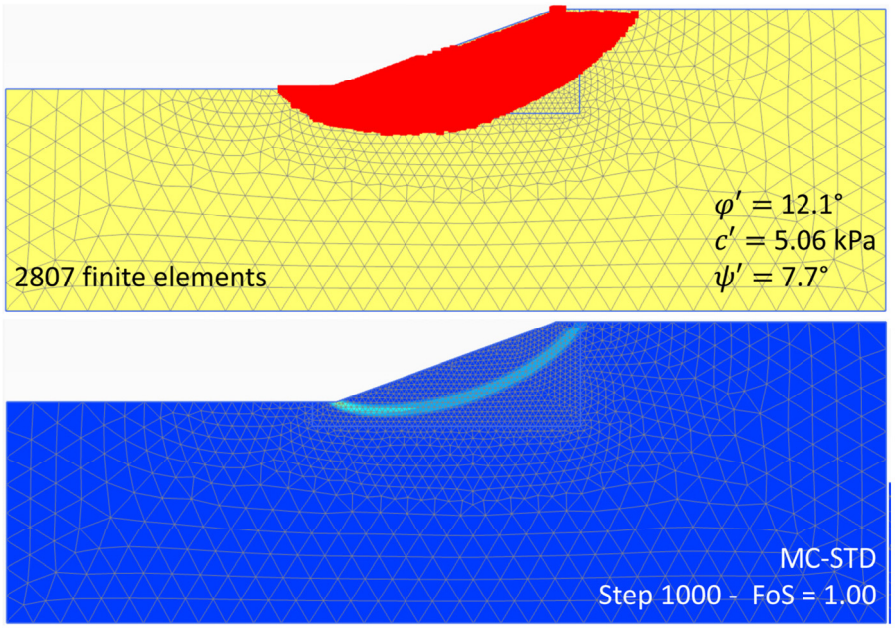

Fig. 65 MC-STD: plasticity zone (top) and incremental deviatoric strain (bottom)

Tab. 12 Stepwise stress state with MC-STD – SP 11725

Step	σ_1	σ_2	σ_3	p'	q'	φ'	c'	θ
	[kN/m²]	[kN/m²]	[kN/m²]	[kN/m²]	[kN/m²]	[°]	[kPa]	[°]
Step 3	2.80	1.18	1.13	1.71	1.65	12.1	5.06	-28.6
Step 7	22.85	8.88	6.75	12.83	15.15	12.1	5.06	-23.0
Step 14	27.15	11.01	9.55	15.90	16.91	12.1	5.06	-25.7
Step 1	26.63	10.88	9.65	15.72	16.40	12.1	5.06	-26.3
Step 127	18.65	6.79	3.98	9.81	13.48	12.1	5.06	-19.6
Step 253	18.65	6.79	3.98	9.81	13.48	12.1	5.06	-19.6
Step 379	18.66	6.79	3.99	9.81	13.49	12.1	5.06	-19.6
Step 505	18.72	6.83	4.03	9.86	13.51	12.1	5.06	-19.7
Step 631	18.62	6.78	3.97	9.79	13.47	12.1	5.06	-19.6
Step 754	18.57	6.76	3.93	9.75	13.45	12.1	5.06	-19.5
Step 877	18.74	6.85	4.04	9.87	13.51	12.1	5.06	-19.6
Step 1000	18.69	6.82	4.01	9.84	13.49	12.1	5.06	-19.6

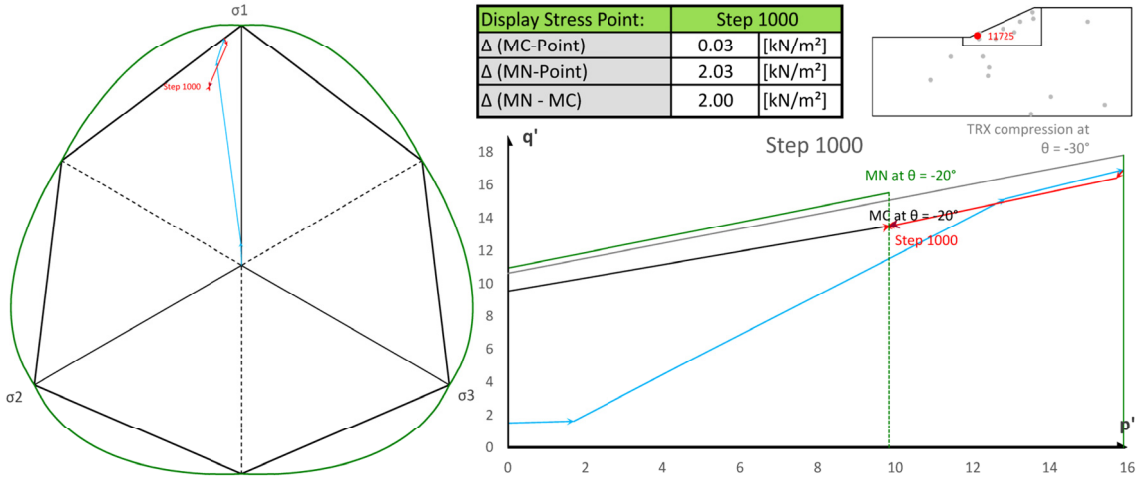

Fig. 66 π-plane (left) and p-q-space (right) with MC-STD – SP 11725

- **MN-GR**

Due to the slope geometry in combination with the cohesion, the generation of initial stresses with a linear elastic material can be avoided (see chapter 5.3.2). The amount of points hitting the yield surface (plastic points) reduce significantly in this analysis (see Fig. 67).

Tab. 13 is structured the same as before explained in MC-STD. It is of interest that the lode angles in the first steps of the initial phase match quite well with that in MC-STD. But during the φ-c-reduction, the intermediate principal stress increases noticeably. Whereas σ_1 and σ_3 decrease slightly. Consequently a large change in the lode angle, namely $\theta = 5.4°$ (step 1000) is observed.

On the right side of Fig. 68 the p-q-space shows, that the stress path moves backwards along the MN failure line. At step 1000 the difference between SP 11725 and the MN yield surface amounts 0.13 kN/m². Consequently, SP 11725 can be interpreted as a failure point (see also Fig. 69).

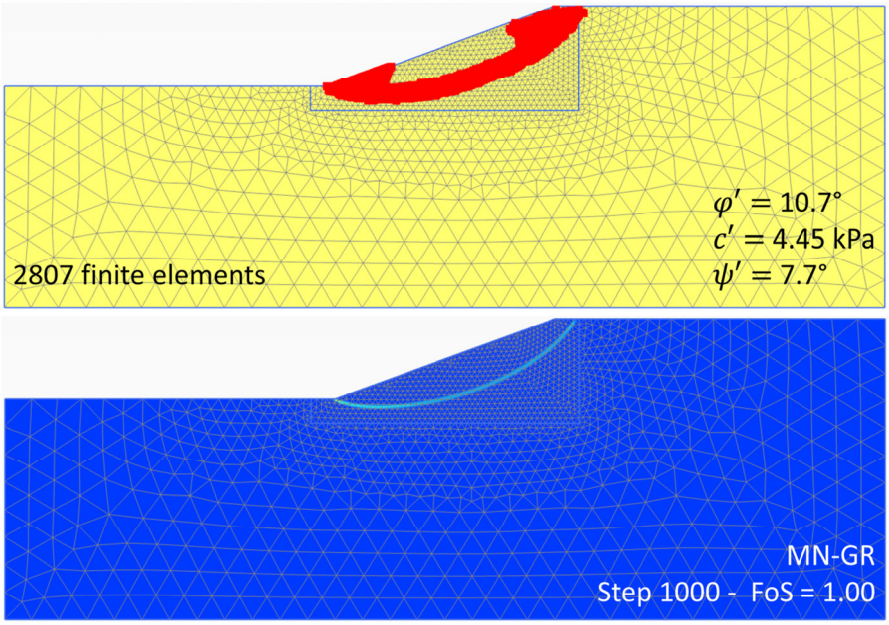

Fig. 67 MN-GR: plasticity zone (top) and incremental deviatoric strain (bottom)

Tab. 13 Stepwise stress state with MN-GR – SP 11725

Step	σ_1	σ_2	σ_3	p'	q'	φ'	c'	θ
	[kN/m²]	[kN/m²]	[kN/m²]	[kN/m²]	[kN/m²]	[°]	[kPa]	[°]
Step 3	2.20	0.92	0.87	1.33	1.31	10.7	4.45	-28.0
Step 7	11.83	4.53	3.25	6.54	8.01	10.7	4.45	-22.1
Step 14	27.00	17.68	9.22	17.97	15.40	10.7	4.45	-1.6
Step 1	26.50	17.64	9.11	17.75	15.07	10.7	4.45	-0.6
Step 127	26.50	17.64	9.11	17.75	15.07	10.7	4.45	-0.6
Step 253	26.49	19.19	9.03	18.23	15.18	10.7	4.45	5.4
Step 379	26.28	18.98	8.85	18.04	15.16	10.7	4.45	5.3
Step 505	26.35	19.03	8.94	18.11	15.14	10.7	4.45	5.3
Step 631	25.31	18.21	8.26	17.26	14.83	10.7	4.45	5.5
Step 754	25.09	18.01	8.10	17.07	14.79	10.7	4.45	5.5
Step 877	24.71	17.64	7.88	16.74	14.63	10.7	4.45	5.2
Step 1000	24.78	17.71	7.89	16.79	14.69	10.7	4.45	5.4

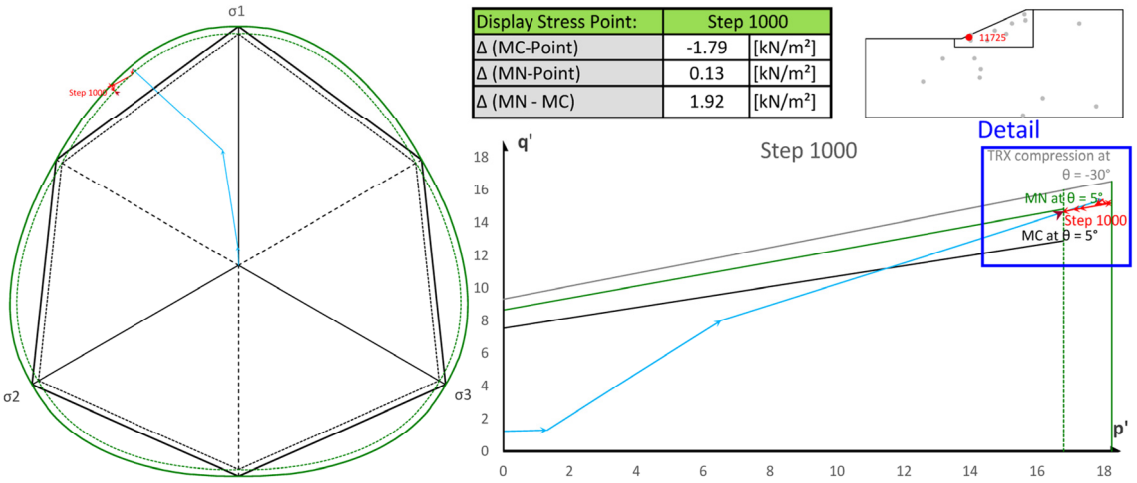

Fig. 68 π-plane (left) and p-q-space (right) with MN-GR – SP 11725

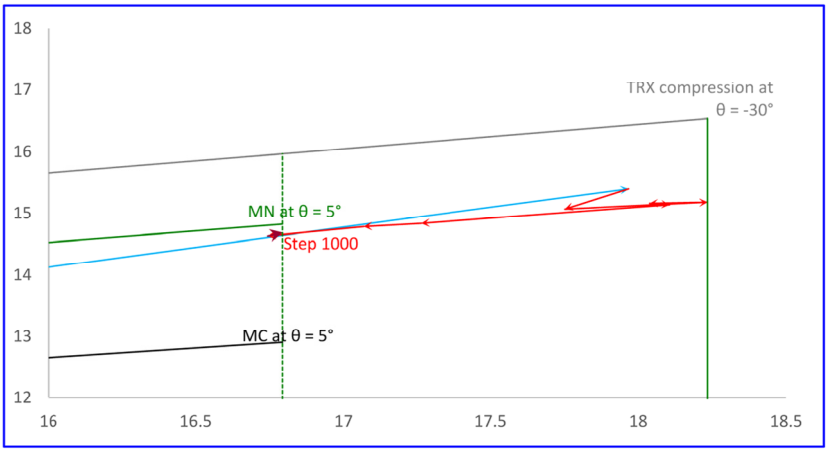

Fig. 69 Detail: MN-GR – SP 11725

- **MN-LE**

Next, the impact on the initial stress state is studied, based on the differences between MN-GR and MN-LE. Comparing Fig. 67 and Fig. 70 shows that the zone of plasticity as well as the failure mechanism are identical. Which shows again, that the approach MN-LE (see also chapter 5.6.1) is suitable.

Tab. 14 lists the stress state at several steps arising from MN-LE. The grey-shaded fields present the plastic phase (plastic nil-step). The fields with orange background relate to the *Safety phase* (by means of strength reduction).

The deviatoric plane as well as the p-q-space presented in Fig. 71 visualize the development of stresses. Note, the difference between SP 11725 and the MN yield surface is neglectable small with Δ(MN-Point) = 0.11 kN/m² and therefore indicated as a failure point (see also Fig. 72).

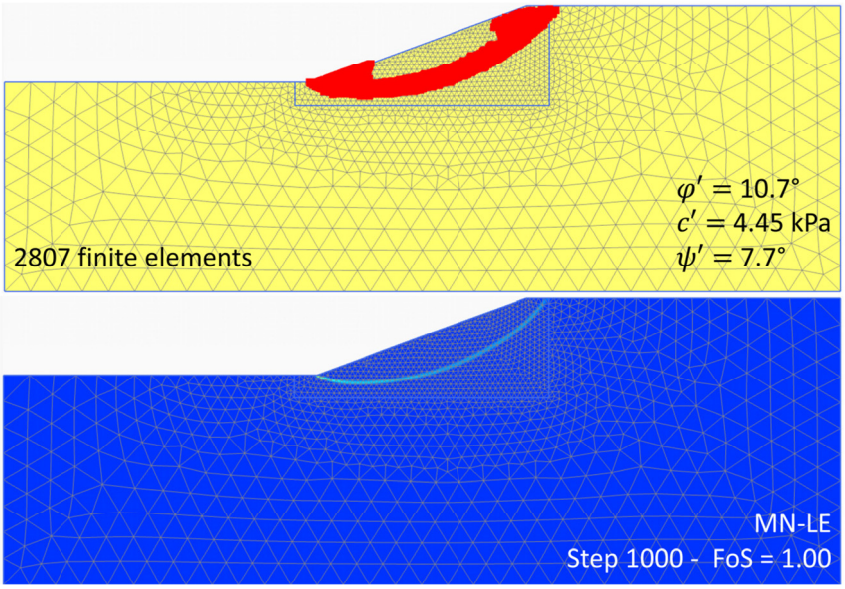

Fig. 70 MN-LE: plasticity zone (top) and incremental deviatoric strain (bottom)

Tab. 14 Stepwise stress state with MN-LE – SP 11725

Step	σ_1	σ_2	σ_3	p'	q'	φ'	c'	θ
	[kN/m²]	[kN/m²]	[kN/m²]	[kN/m²]	[kN/m²]	[°]	[kPa]	[°]
Step 3	24.82	10.39	9.06	14.75	15.14	10.7	4.45	-25.6
Step 7	28.48	15.76	10.06	18.10	16.34	10.7	4.45	-12.4
Step 14	28.09	18.83	9.74	18.88	15.89	10.7	4.45	-0.3
Step 1	26.65	18.44	9.16	18.08	15.15	10.7	4.45	2.0
Step 127	26.51	19.19	9.06	18.26	15.18	10.7	4.45	5.3
Step 253	26.38	19.08	8.95	18.14	15.16	10.7	4.45	5.4
Step 379	26.30	18.97	8.87	18.05	15.15	10.7	4.45	5.3
Step 505	26.27	19.01	8.91	18.07	15.10	10.7	4.45	5.4
Step 631	26.39	19.09	8.96	18.14	15.17	10.7	4.45	5.3
Step 754	25.92	18.67	8.65	17.75	15.02	10.7	4.45	5.3
Step 877	24.89	17.86	7.99	16.91	14.70	10.7	4.45	5.6
Step 1000	25.59	18.51	8.45	17.52	14.92	10.7	4.45	5.7

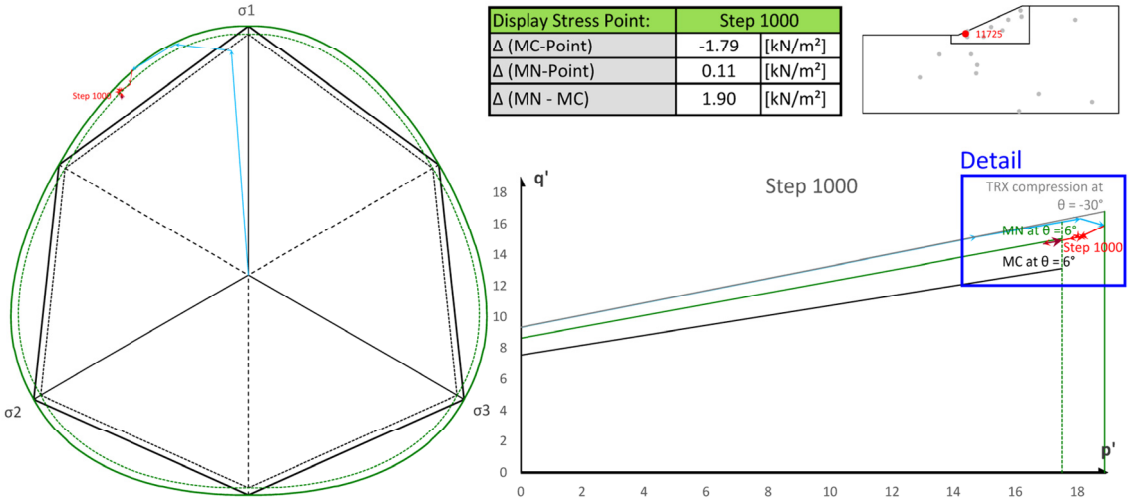

Fig. 71 π-plane (left) and p-q-space (right) with MN-LE – SP 11725

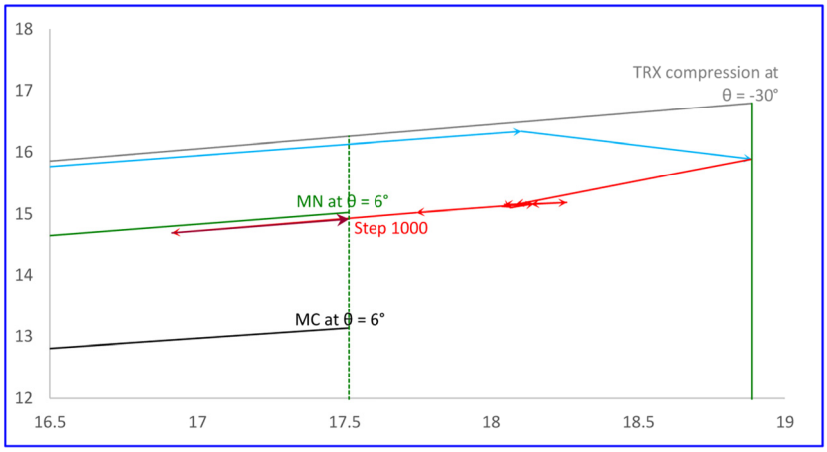

Fig. 72 Detail: MN-LE – SP 11725

- **Comparison of the lode angle**

Fig. 73 underlines the differences in the lode angle for previous discussed models (MC-STD, MN-GR and MN-LE). It has to be mentioned that right from the start, θ deviates strongly from MC-STD. However, when performing MN-LE FEA the lode angle as well as the stresses itself show good accordance with MN-GR. Except of the stress state in

the first steps, which are unusual high, due to the linear elastic material model applied in the initial phase. Calculations performed with the MC failure criterion range between -28.6° ≤ θ ≤ -19.6°. MC-STD and MN-GR show good correlation at the beginning of the calculation. However, during the strength reduction θ of MN-GR increases from -28° up to 5.4°. Whereas with MC-STD a lode angle of θ = -19.6° is computed. This means a difference of 25° between MC-STD and MN-GR. On the other side, after some calculation steps θ of MN-GR shows good agreement with θ of MN-LE.

Further studies on this slope have revealed, that the lode angle in the failure mechanism derived with the MN failure criterion tends to a value around 5.3° (see Fig. 74). Based on these findings an advice (for simple slopes, as considered here) could be carried out to adopt the equivalent friction angle in order to maintain the less conservative FoS with MC (see chapter 5.8).

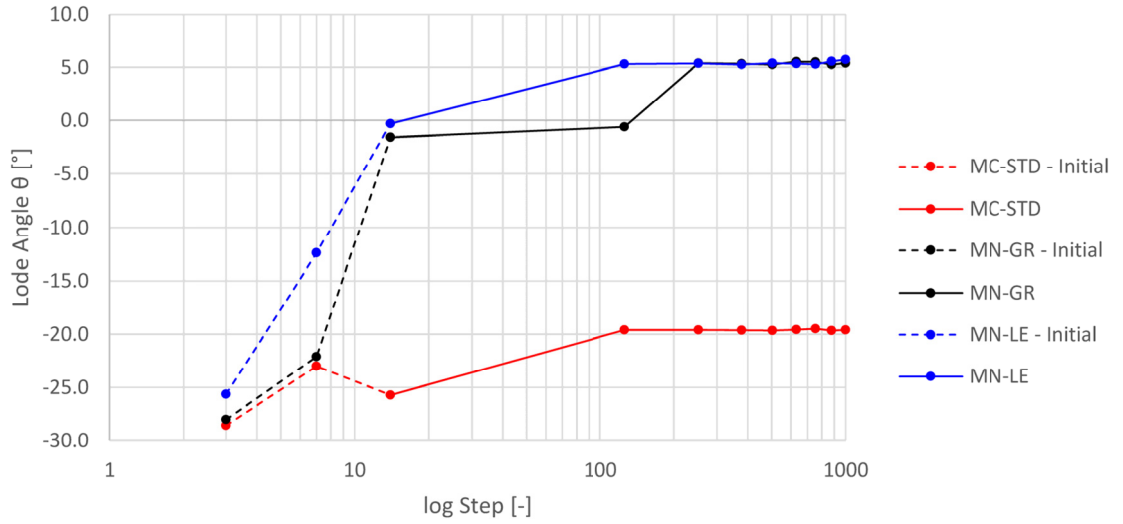

Fig. 73 Comparison of the lode angle

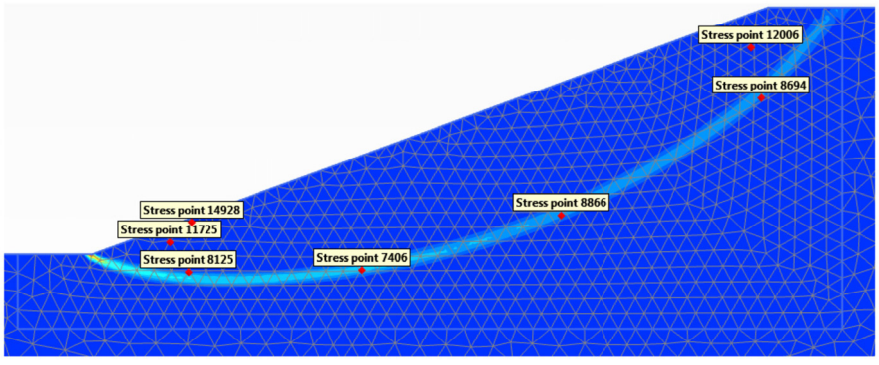

Stress point	θ_{MN-LE} [°]	θ_{MC} [°]
7406	5.3	-21.6
8125	5.3	-22.2
8694	5.3	-16.3
8866	5.3	-29.6
11725	5.7	-19.6
12006	5.3	-29.8
14928	5.3	-15.2

Fig. 74 Position of stress points

5.7 Further studies – Influence of the Matsuoka-Nakai failure criterion

This chapter deals with analyses of a homogeneous slope with factors of safety from FoS = 1.1 up to FoS = 1.4. The following issues are addressed:

- Zone of plasticity
- Failure mechanism
- Size of slip surface
- Factor of safety - ΣM_{sf} vs. steps
- Stress paths

5.7.1 Geometry and material set

The dimension of the slope (Fig. 75) is based on the height with $H = c/(\gamma_{unsat} \cdot 0.05)$ and the parameters listed in Tab. 15 are used. Hence, a slope inclination of $\beta = 26.6°$ is modelled and the mesh is generated with 1004 15-noded triangles. More details about the input parameters associated with the individual material models, are given in Appendix J.

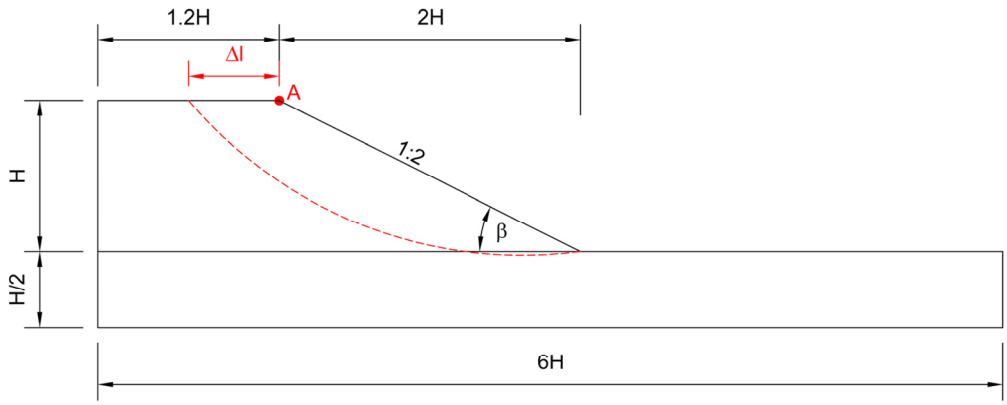

Fig. 75 Slope geometry – detailed analysis of a stable slope

Tab. 15 Parameters – detailed analysis of a stable slope

Parameter	Value	Unit
γ_{unsat}	16.0	[kN/m³]
c	8.00	[kN/m²]
ψ	0.00	[°]
ν	0.20	[-]
H	10.0	[m]

5.7.2 Investigations related to the failure mechanism

In the following, the zone of plasticity as well as the failure mechanism obtained after the φ-c-reduction are compared (for both failure criteria MC and MN). Therefore, several states of stability (values of FoS) are considered, which are controlled by a varying friction angle. The corresponding cohesion and dilatancy angle are kept constant with c = 8 kN/m² and $\psi = 0°$. Comparing Fig. 76 to Fig. 79 shows that the plastic points with MC are almost similar in all calculations, which is not the case if MN is used. With the Matsuoka-Nakai model the zone of plasticity reduces with increasing factors of safety. The slip plane is well-defined and intersects the foot of the slope in all cases. Due to a moderate slope inclination of 1:2 and a considerable cohesion it could be assumed, that no erratic ΣM_{sf} vs. step curve is computed. A closer look at the ΣM_{sf} vs. step curve of the model considering a MN failure criterion and a friction angle of $\varphi = 21.1°$ shows the opposite (see Fig. 80). The factor of safety at each step is also marked in Fig. 80. It has to be noted, that the change of the slip surface is associated with the rapid drop in the factor of safety. A numerical problem in the current version of the MN model.

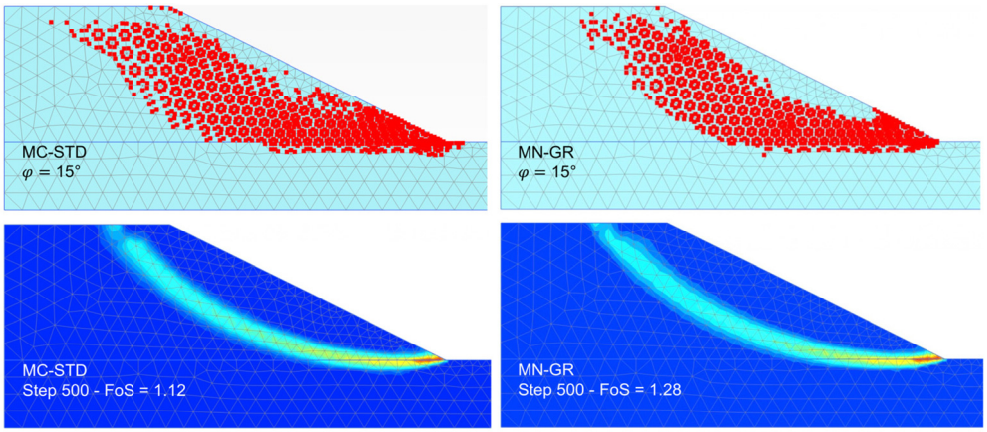

Fig. 76 Plasticity zone and incremental deviatoric strain at $\varphi = 15°$ with MC (left) and MN (right)

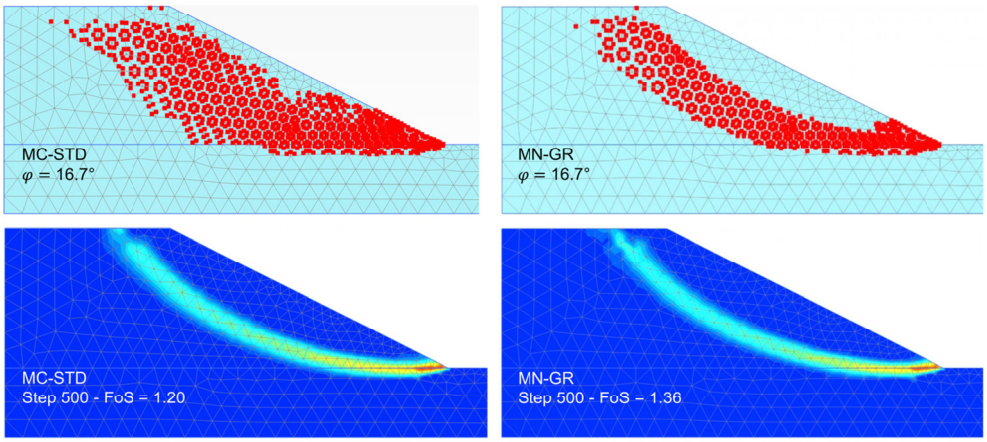

Fig. 77 Plasticity zone and incremental deviatoric strain at $\varphi = 16.7°$ with MC (left) and MN (right)

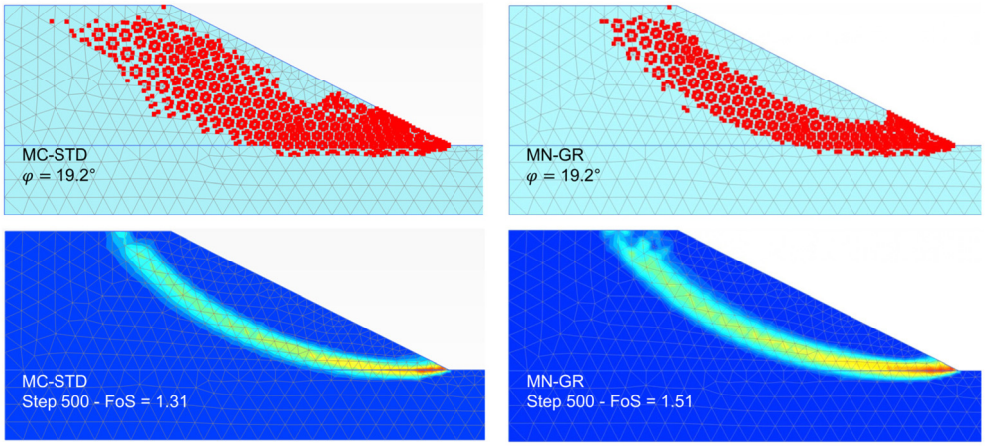

Fig. 78 Plasticity zone and incremental deviatoric strain at $\varphi = 19.2°$ with MC (left) and MN (right)

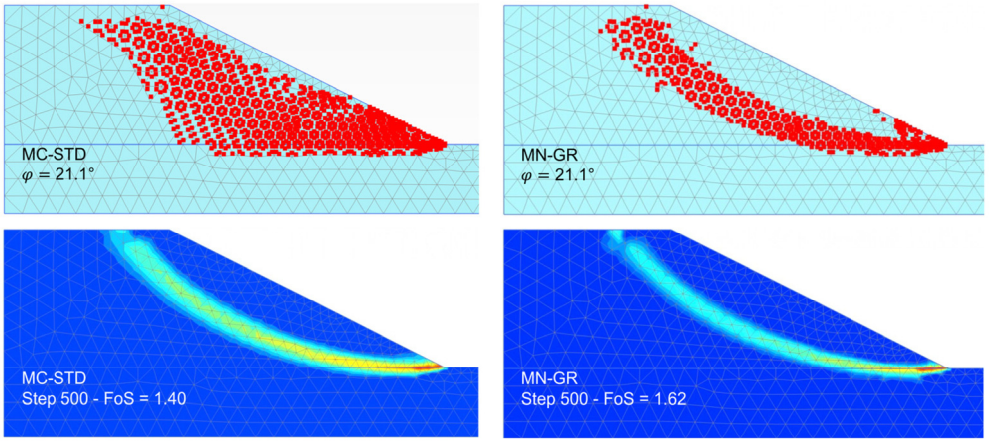

Fig. 79 Plasticity zone and incremental deviatoric strain at $\varphi = 21.1°$ with MC (left) and MN (right)

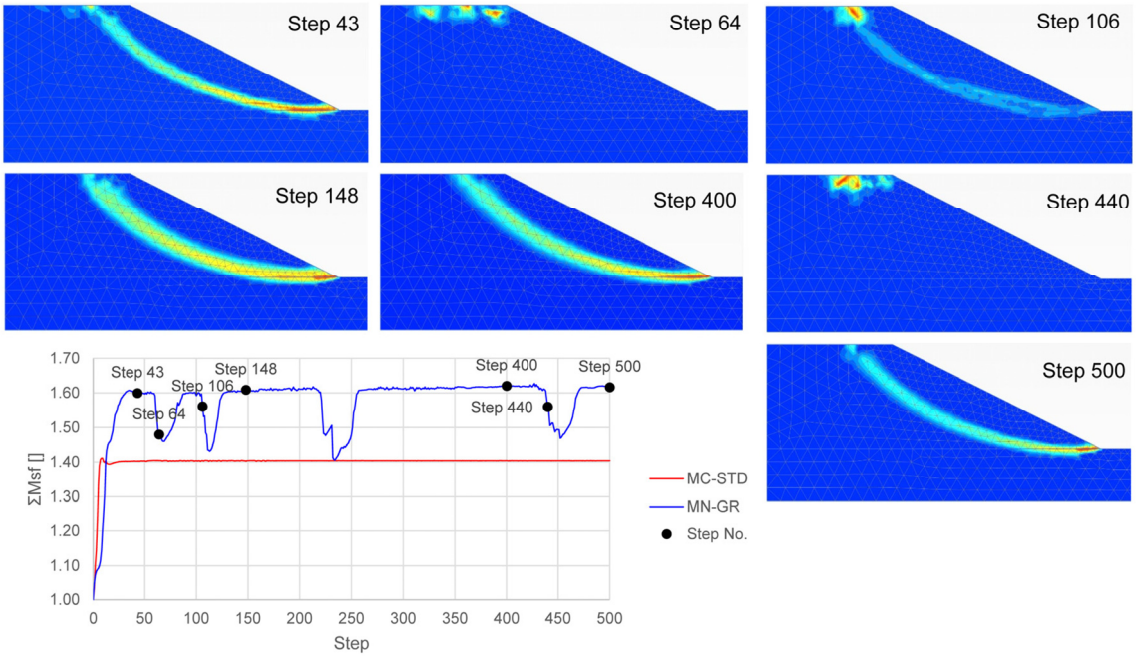

Fig. 80 FoS and incremental deviatoric strain for several steps with MN-GR and $\varphi = 21.1°$

The reason for a diverging FoS is based on either the failure mechanism or the failure criterion. For this reason, the size of the failure mechanism is compared. Therefore the distance Δl as indicated in Fig. 75 is worked out for different FEA. The measured distances listed in Tab. 16 do not diverge excessively, consequently the difference in FoS is only related to the different failure criteria.

Tab. 16 Measured distance of onset of failure at step 500 (c = 8 kN/m²)

Sample for φ	Δl_{MC}	Δl_{MN}	$100 \cdot (\Delta l_{MN} - \Delta l_{MC}) / \Delta l_{MN}$
[°]	[m]	[m]	[%]
15.0	4.21	5.17	18.6
16.7	3.74	3.74	0.0
19.2	3.74	3.74	0.0
21.1	3.28	3.74	12.3

5.7.3 Factor of safety - ΣM_{sf} vs. steps

The represented results in Fig. 81 are based on a friction angle of $\varphi = 19.2°$ and a cohesion of c = 8 kN/m². The FoS with a varying *incremental multiplier* M_{sf} and modified *tolerated error* ε_{tol} settings are demonstrated. The left side deals with the effect of M_{sf} for three different constitutive models (MC, HS and HSS), whereas the right side shows the effect of the tolerated error. As already indicated in chapter 5.5, various incremental multiplier settings result in similar values of FoS regardless of the material model. However, this does not hold for a change in the tolerated error. Although, the results computed with a tolerated error of 0.02, 0.01 and 0.001 seem to show a reasonable agreement, whereas the others do effect the factor of safety noticeably.

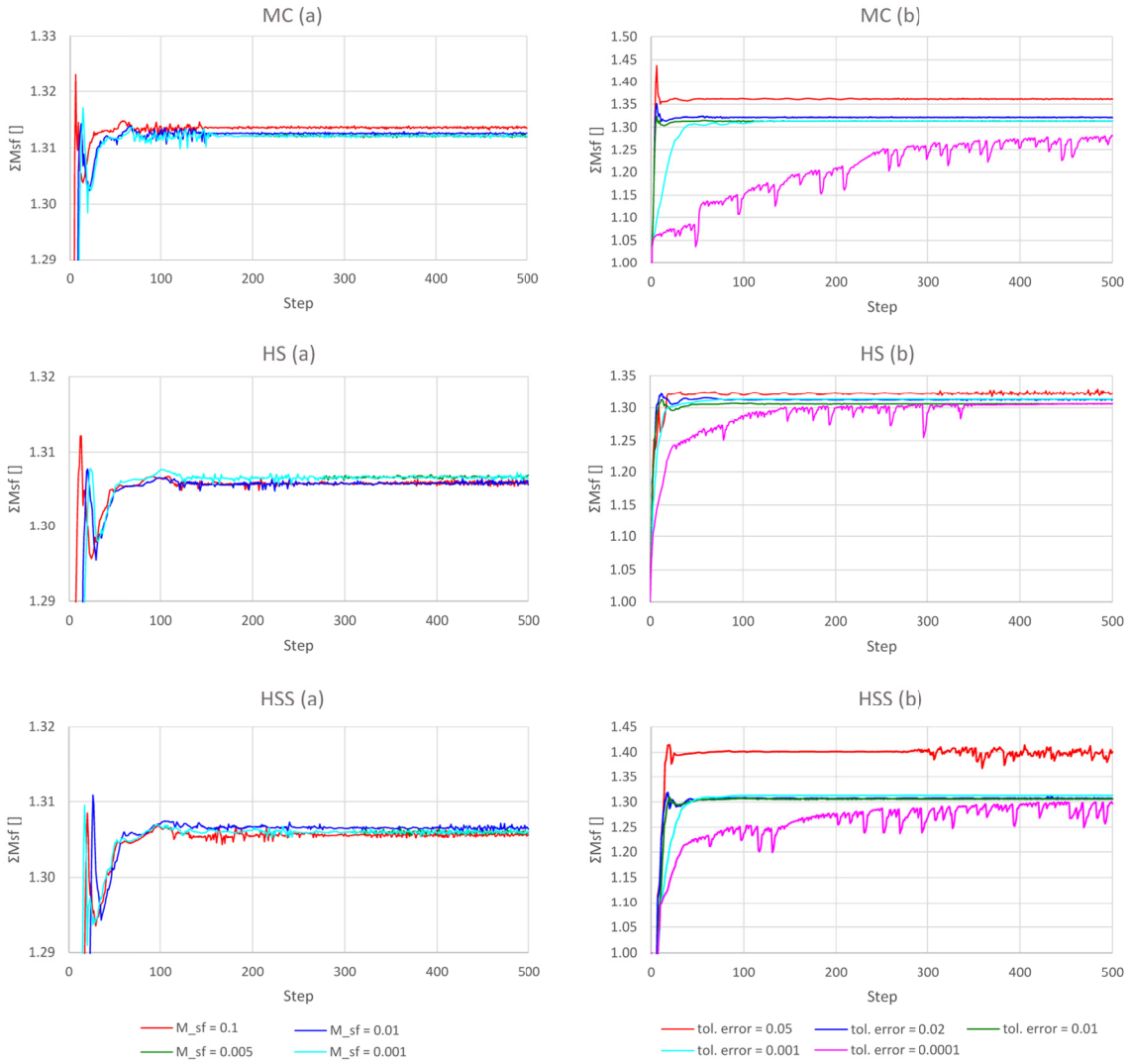

Fig. 81 Effect of M_{sf} (a) and tolerated error (b) on FoS when $\varphi = 19.2°$

The influence of the φ-c-reduction for this slope with $\beta = 26.6°$ is studied in regard to the dependency of the friction angle and the cohesion. Therefore, the difference in the factor of safety is calculated with:

$$\Delta FoS = (FoS_{MN} - FoS_{MC}) \cdot 100 \qquad (77)$$

The results plotted in Fig. 82 point out that the ΔFoS at a specific cohesion grows almost linear. Furthermore, it seems that with greater cohesion the difference of FoS increases. Additionally, the factor of safety for each failure criteria can be observed in Fig. 83.

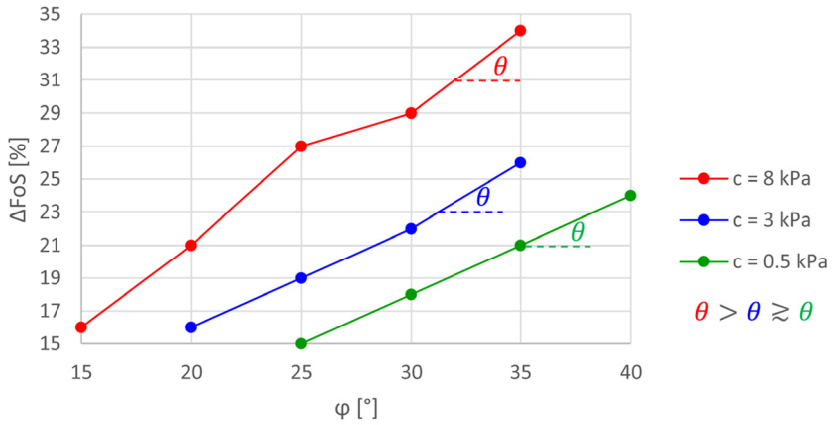

Fig. 82 ΔFoS dependent on φ and c

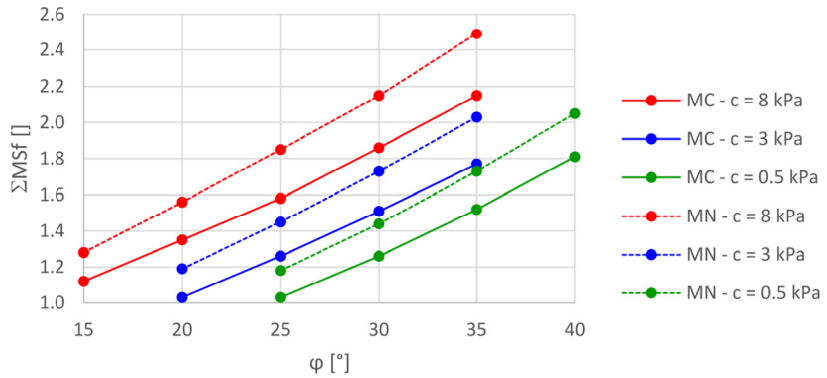

Fig. 83 FoS_{MC} and FoS_{MN} dependent on φ and c

5.7.4 Stress paths

Finally, the stress paths for the two different failure criteria are compared with each other. The examined stress point SP 927 is located in the slip surface of the slope presented in Fig. 79 and Fig. 80, namely with $\varphi = 21.1°$. There, a factor of safety with MC of FoS = 1.4 and with MN of FoS = 1.62 is obtained.

Tab. 17 and Tab. 18 indicate the stress state at several steps calculated with the material set MC-STD and MN-GR, respectively. The grey-shaded fields present the initial phase (*Gravity loading*). The fields with orange background relate to the *Safety phase* (by means of strength reduction). During the calculation the lode angle with MC-STD stays fairly constant with about θ = -25°. Whereas the lode angle with MN-GR tends towards zero. From the deviatoric plane in Fig. 84 it can be recognized that the lode angle starts to diverge strongly during the safety analysis. It should be noted, that the π-plane in red (dashed lines) indicates the material set MC-STD and the blue one (solid lines) corresponds to MN-GR.

The stress path with MC-STD shows a change in p' of approximately 5 kN/m². There, inspected stress point SP 927 do not reach the yield surface (MC) at the last calculation

step (step 500). But is elastic related to a distance of Δ(MC-Point) = 14.58 kN/m². However, the stress path obtained with MN-GR increases by further 19.5 kN/m² along the p' axis. At this approach the distance between the stress state at the considered calculation step (step 500) and the yield surface (MN) is given with Δ(MC-Point) = 21.12 kN/m². For the analysis follows, that the intermediate principal stress σ_2 at step 500 is about 43 % greater than with MC-STD.

Tab. 17 Stepwise stress state with MC-STD – SP 927

Step	σ_1	σ_2	σ_3	p'	q'	φ'	c'	θ
	[kN/m²]	[kN/m²]	[kN/m²]	[kN/m²]	[kN/m²]	[°]	[kPa]	[°]
Step 1	20.12	10.10	8.72	12.98	10.78	21.1	8.0	-23.66
Step 2	46.96	23.56	20.35	30.29	25.16	21.1	8.0	-23.66
Step 3	79.83	40.04	34.57	51.48	42.79	21.1	8.0	-23.65
Step 1	79.97	40.17	34.79	12.98	10.78	21.1	8.0	-23.75
Step 64	68.82	35.05	31.31	45.06	35.79	21.1	8.0	-24.81
Step 127	69.05	35.17	31.43	45.21	35.89	21.1	8.0	-24.83
Step 190	69.31	35.32	31.59	45.41	36.00	21.1	8.0	-24.86
Step 253	70.83	36.18	32.48	46.50	36.64	21.1	8.0	-24.98
Step 316	70.94	36.24	32.54	46.57	36.69	21.1	8.0	-25.00
Step 379	70.98	36.25	32.56	46.59	36.71	21.1	8.0	-25.00
Step 440	70.91	36.20	32.52	46.54	36.69	21.1	8.0	-25.01
Step 500	70.92	36.22	32.53	46.55	36.68	21.1	8.0	-24.99

Tab. 18 Stepwise stress state with MN-GR – SP 927

Step	σ_1	σ_2	σ_3	p'	q'	φ'	c'	θ
	[kN/m²]	[kN/m²]	[kN/m²]	[kN/m²]	[kN/m²]	[°]	[kPa]	[°]
Step 1	13.12	3.27	3.21	6.53	9.88	21.1	8.0	-29.73
Step 3	51.56	16.39	13.59	27.18	36.65	21.1	8.0	-26.20
Step 4	78.92	27.93	24.77	43.88	52.64	21.1	8.0	-27.02
Step 1	78.68	29.33	27.04	6.53	9.88	21.1	8.0	-27.74
Step 64	87.16	63.37	41.43	63.98	39.61	21.1	8.0	-1.34
Step 127	87.10	63.78	41.45	64.11	39.53	21.1	8.0	-0.71
Step 190	86.13	63.69	41.20	63.67	38.90	21.1	8.0	0.03
Step 253	86.21	63.79	41.46	63.82	38.76	21.1	8.0	-0.07
Step 316	86.03	63.55	41.15	63.57	38.87	21.1	8.0	-0.05
Step 379	85.77	63.40	41.06	63.41	38.72	21.1	8.0	-0.02
Step 440	86.11	63.68	41.25	63.68	38.85	21.1	8.0	0.00
Step 500	85.82	63.52	41.09	63.48	38.74	21.1	8.0	0.09

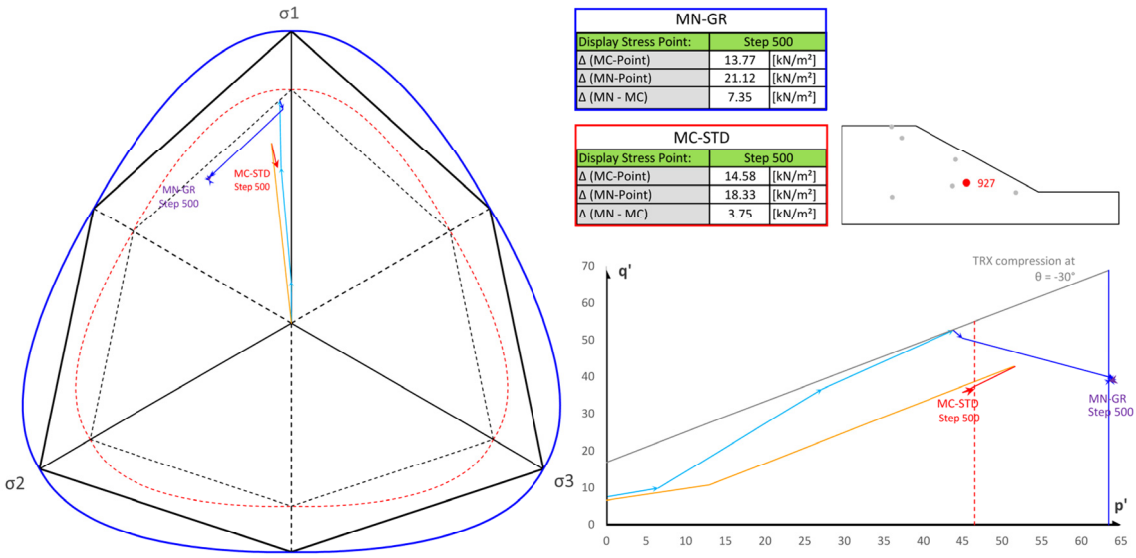

Fig. 84 π-plane (left) and p-q-space (right) with MN-GR and MC-STD – SP 11725

5.8 Adoption of the equivalent friction angle

It is of interest to formulate a possible advice for the prediction of the equivalent friction angle φ'_{mc}. The magnitude of the equivalent friction angle depends on the lode angle, the principal effective stresses and the cohesion. For this reason, the challenge is to determine a compatible lode angle. It is assumed for the moment, that the required lode angle can be derived from the zone of maximum deviatoric strain. This means, that the evaluated stress point should be located in a pronounced slip plane.

Besides, numerical simulations of a direct simple shear test (*SoilTest* tool in Plaxis 2D) have identified, that the lode angle at moderate to high initial stress states becomes zero, independent of the failure criterion. Although, this is not applicable for low stress states performed with MC. There, the lode angle tends to be -10°.

Based on these findings, the equivalent friction angle φ'_{mc} at $\theta = 0°$ obtained in a MN-LE calculation is used in a MC-STD model. Afterwards both FoS are set in relation according to Equ. (77). This procedure is carried out for several slopes as listed in Tab. 19. Although the results of the slopes (a) to (d) correlate quite well, the difference between the FoS is slightly greater once the dilatancy angle reduces to zero (highlighted in red). It should be noted, that the computation of MN is still needed in order to determine φ'_{mc}. Due to the fact that φ'_{mc} depends on θ, p' and c'. For future work, it would be beneficial to investigate an approach to determine the equivalent friction angle without the necessity of a FEA with the Matsuoka-Nakai failure criterion.

Tab. 19 Comparison of FoS for several slopes

							Before				After
Slope	β	φ	c	ψ	FOS_{MC}	FOS_{MN}	Δ FOS = (FOS_{MN} - FOS_{MC}) · 100	SP	φ_{MC} at θ = 0	FOS_{MC*} = f{φ_{MC}}	Δ FOS = (FOS_{MN} - FOS_{MC*}) · 100
	[°]	[°]	[kPa]	[°]	[-]	[-]	[%]	[-]	[°]	[-]	[%]
(a)	35.0	37.3	0.00	12.4	1.00	1.18	**17.60**	20209	41.34	1.18	**-0.30**
(b)	25.0	25.0	5.00	8.3	1.46	1.68	**21.20**	7346	29.21	1.68	**-0.80**
(c)	20.0	10.7	4.45	7.7	<1.00	1.00	-	8866	12.72	1.00	**0.21**
(d)	20.0	12.1	5.06	4.0	1.00	1.14	**13.70**	7561	14.41	1.13	**0.30**
(e)	26.6	33.0	0.00	0.0	1.31	1.49	**17.50**	957	36.87	1.50	**-1.80**
(f)	26.6	33.0	8.00	0.0	2.03	2.35	**31.90**	1215	39.03	2.40	**-4.80**
(g)	26.6	16.7	8.00	0.0	1.19	1.38	**18.20**	927	20.27	1.36	**1.30**

6 Conclusion and Outlook

Prior works have documented the effect of the failure criterion based on Matsuoka-Nakai compared to Mohr-Coulomb e.g. [5]. There it has been shown, that a higher mobilization of shear strength leads to a higher factor of safety. This thesis has mainly focused on cohesionless slopes and results are compared with analytical approaches. Various cohesionless slopes were analysed by means of a displacement finite-element method in order to determine the strength parameters at ultimate limit state. It was found that for small slope inclinations, the friction angle at failure based on Mohr-Coulomb fits quite well with the approach developed by Davis [3]. Nevertheless, for steeper slopes and decreased dilatancy angles these results are closer to the results obtained with the empirical equation considering the Matsuoka-Nakai failure criterion developed by Schranz et al. [5].

Another point of interest was to illustrate the development of the stress paths, not only for cohesionless soils but also for cohesive materials. The stress paths were generated based on results obtained with both failure criteria. Differences with respect to the lode angle, the failure mechanism, the size of the slip surface as well as the factor of safety are discussed. Due to the consideration of the intermediate principal stress it was expected, that when using a Matsuoka-Nakai failure criterion the stress path differs from the one obtained with Mohr-Coulomb. For simple homogeneous slopes it seems, that the lode angle in the slip surface tends to a value between 0° and 5°.

Finally, an advice was proposed to adopt the equivalent friction angle for the Mohr-Coulomb failure criterion (again for simple homogeneous slopes as discussed in this thesis). But this approach still requires a computation with the Matsuoka-Nakai failure criterion.

All discussed models in this thesis are computed in the two-dimensional space considering plane strain condition. Eventually, this is an assumption which might not be in accordance with reality. Therefore, the potential influence of different failure criteria on the factor of safety should also be investigated in three-dimensional finite-element analysis.

7 References

[1] F. Tschuchnigg, H. F. Schweiger, S. W. Sloan, A. V. Lyamin and I. Raissakis, “Comparison of finite-element limit analysis and strength reduction techniques,” *Géotechnique 65, No. 4,* pp. 249-257, 2015.

[2] F. Tschuchnigg and H. F. Schweiger, “Performance of strength reduction finite element techniques for slope stability problems,” in *Proceedings of 16th European conference on soil mechanics and geotechnical engineering "Geotechnical Engineering for Infrastructure and Development"*, Edinburgh, 2015.

[3] E. H. Davis, “Theories of plasticity and the failure of soil masses,” *Soil mechanics, selected topics (ed. I. K. Lee). Butterworth,* 1968.

[4] H. Matsuoka and T. Nakai, “Stress-deformation and strength characteristics of soil under three different prinipal stresses,” in *Proc., JSCE, No. 232, pp. 59-70*, 1974.

[5] F. Schranz and W. Fellin, “Stability of infinite slopes investigated with elastoplasticity and hypoplasticity,” *Geotechnik, Vol. 39, No. 3, pp. 184-194,* 2016.

[6] R. B. J. Brinkgreve, W. M. Swolfs and E. Engin, Plaxis 2D 2016 - User manual, Delft, Netherlands: Plaxis bv., 2016.

[7] R. Hill, The Mathematical Theory of Plasticity, Clarendon Press, 1998.

[8] H. F. Schweiger, *Ein Beitrag zur Anwendung der Finite-Elemente-Methode in der Geotechnik. Habilitation, Graz University of Technology,* 1995.

[9] B. De Saint Venant, *Journal de mathématiques pures et applicquées,* 1870.

[10] R. B. J. Brinkgreve, S. Kumarswamy and S. W. M., Plaxis 2D 2016 - Material Models Manual, Delft, Netherlands: Plaxis bv., 2016.

[11] M. Wehnert, “Ein Beitrag zur drainierten und undrainierten Analyse in der Geotechnik,” *Mitteilung 53 des Instituts für Geotechnik,* 2006.

[12] D. M. Potts and Z. L., Finite element analysis in geotechnical engineering: theory, London: Thomas Telford, 1999.

[13] A. N. Schofield and P. Wroth, Critical State Soil Mechanics, McGraw-Hill, 1968.

[14] H. Matsuoka and T. Nakai, “Relationship among Tresca, Mises, Mohr-Coulomb and Matsuoka-Nakai failure criteria,” *Soils and Foundations, Vol. 25, No. 4, pp. 123-128,* December 1985.

[15] D. V. Griffiths, “Failure criteria interpretation based on Mohr-Coulomb friction,” *J. Geotech. Engrg., Vol. 116, No. 6, pp. 986-999,* 1990.

[16] D. Griffiths and J. Huang, “Observations on the extended Matsuoka-Nakai failure criterion,” *Int. J. Numer. Anal. Meth. Geomech., No. 33, pp. 1889-1905,* June 2009.

[17] M. Satake, “Comment in Proc. U.S.-Japan Seminar on Continuum Mechanical and Statistical Approaches in the Mechanics of Granular Materials,” in *Gakujustu Bunken Fukyu-kai*, Tokyo, 1978.

[18] A. W. Bishop, “The strength of soils as engineering materials. 6th Rankine lecture,” *Géotechnique, Vol. 16, No. 9, pp. 91-130,* 1996.

[19] F. Schranz and W. Fellin, “On the stability of infinite slopes,” in *Proceedings of the 24th European Young Geotechnical Engineers Conference (EYGEC)*, Durham, UK, 2015.

[20] R. A. Jewell, “Direct shear tests on sand,” *Geotechnique, Vol. 39, No. 2, pp. 309-322,* 1989.

[21] P. W. Rowe, “The relation between the shear strength of sands in triaxial compression, plane strain and direct shear,” *Géotechnique, Vol. 19, No. 1, pp. 75-86,* 1969.

[22] C. Thornton and L. Zhang, “Numerical simulations of the direct shear test,” *chem. Eng. Technol.; Vol. 26, No. 26, pp. 153-156,* 2003.

[23] J. Atkinson, “GeotechnicalCAL,” [Online]. Available: http://environment.uwe.ac.uk/geocal/SoilMech/shear/shear.htm. [Accessed 01 12 2016].

[24] J. A. R. Ortigao, Soil Mechanics in the Light of Critical State Theories, Rotterdam: A. A. Balkema, 1995.

[25] K. L. Lee, “Triaxial compressive strength of saturated sands under seismic loading conditions,” *Phd thesis, University of California, Berkeley,* 1965.

[26] T. Schanz and P. Vermeer, “Angles of friction and dilatancy of sand,” *Géotechnique, Vol. 46, No. 1, pp. 145-151,* 1996.

[27] B. F. u. T. Lehrstuhl und Prüfamt für Grundbau, “Vorlesungsskript,” [Online]. Available: https://www.gb.bgu.tum.de/index.php?id=46&L=0. [Accessed 2017].

[28] T. Schanz, *Zur Modellierung des mechanischen Verhaltens von Reibungsmaterialien. Habilitation, Universität Stuttgart,* 1998.

[29] S. J. Polos, “The Steady State of Deformation,” *Journal of Geotechnical Engineering, 107 (GT5), pp. 553-562,* 1981.

[30] C. A., “Characteristics of cohesionless soils affecting the stability of earth fills,” *J. Boston Soc. Civil Engrs, in Contribution to Soil Mech. pp. 1925-1945,* 1936.

[31] A. W. Jenike, “Storage and flow of solids,” *123. Bulletin of the University of Utah, Vol. 53, No. 26,* 1964.

[32] F. Tschuchnigg, H. F. Schweiger and S. W. Sloan, “Slope stability analysis by means of finite element limit analysis and finite element strength reduction techniques. Part I: Numerical studies considering non-associated plasticity,” *Computers and Geotechnics, No. 70, pp. 169-177,* 2015.

[33] D. W. Airey, “Some observations on the interpretation of shearbox test results,” *Technical report CUED/D - SOILS/TR 196,* 1987.

[34] R. A. Jewell and C. P. Wroth, “Direct shear tests on reinforced sand,” *Geotechnique, Vol. 37, No. 1, pp. 53-68,* 1987.

[35] K. Fakharian and E. Evgin, “Simple Shear Versus Direct Shear Tests on Interface during Cyclic Loading,” in *Third International Conference on Recent Advances in Geotechnical Earthquake Engineering & Soil Dynamics*, St. Louis, Missouri, 1995.

[36] A. W. Bishop, G. E. Green, V. K. Garga, A. Andresen and J. D. Brown, “A new ring shear apparatus and its application to the measurement of residual strength,” *Géotechnique, Vol. 21, No. 4, pp. 273-328,* 1971.

[37] D. Kolymbas, Geotechnik - Bodenmechanik, Grundbau und Tunnelbau, Springer, 2011.

[38] D. W. Hight, A. Gens and M. J. Symes, “The development of a new hollow cylinder apparatus for investigating the effects of principal stress rotation in soils,” *Géotechnique, Vol. 33, No. 4, pp. 355-383,* 1983.

[39] D. W. Taylor, “Fundamentals of soil mechanics,” *Wiley, New York,* 1948.

[40] K. Georgiadis, D. M. Potts and L. Zdravkovic, “Modelling the shear strength of soils in the general stress space,” *Computers and Geotechnics, Vol. 31, No. 5, pp. 357-364,* July 2004.

[41] M. D. Bolton, “The strength and dilatancy of sands,” *Geotechnique, Vol. 36, No. 1, pp. 65-78,* 1986.

[42] W. Fellin, “The rediscovery of infinite slope model,” *Geomechanics and Tunnelling, Vol. 7, No. 4, pp. 299-305,* 2014.

[43] M. Mergili, W. Fellin, S. M. Moreiras and J. Stötter, “Simulation of debris flows in the central andes based on open source gis: possibilities, limitations, and parameter sensitivity.,” *Natural Hazards, Vol. 61, No. 3, pp. 1051-1081,* 2013.

[44] R. B. J. Brinkgreve, W. M. Swolfs and E. Engin, Plaxis 2D 2016 - Reference Manual, Delft, Netherlands: Plaxis bv., 2016.

[45] T. Benz, “Small-Strain Stiffness of Soils and its Numerical Consequences,” *Mitteilung 55 des Institutes für Geotechnik,* 2007.

[46] G. Houlsby, “A general failure criterion for frictional and cohesive materials,” *Soils and Foundations, Vol. 26, No. 2, pp. 97-101,* June 1986.

[47] H. Matsuoka, “On the significance of the "Spatial Mobilized Plane",” *Soils and Foundations, Vol. 16, No. 1,* March 1976.

[48] A. Laera and R. B. J. Brinkgreve, Plaxis 2015 - Site response analysis and liquefaction evaluation, Delft, Netherlands: Plaxis bv., 2015.

Appendix A

The problem (described in chapter 2.3.2) is mitigated, when the minus in Equ. (49) is substituted with a plus and then the whole term is multiplied with minus one, so that φ'_{mc} changes to:

$$\varphi'_{mc} = \frac{1}{2}\pi - 2\tan^{-1}\left(\frac{c' + \sqrt{c'^2 + \sigma'_1\sigma'_3}}{\sigma'_3}\right) \qquad (78)$$

Previously, the third effective stress σ'_3 of the current stress state has been taken into account in order to derive σ'_1 iteratively. Subsequently this approach has been modified by determining σ'_3 and σ'_1 at the triaxial compression state ($\sigma'_1 > \sigma'_2 = \sigma'_3$). Since p' can be computed with Equ.(19) at triaxial compression and the position of the deviatoric plane on the isotropic axis for a certain stress point is given by p', the corresponding effective stresses are determinable. There the deviatoric stress q' is defined by a_c (see Equ.(23)) which can be reformulated to:

$$\sigma'_3 = \frac{1}{2}\left(\frac{3(a_c - c_c)}{\tan\varphi'_c} - \sigma'_1\right) \qquad (79)$$

Where σ'_1 is solved for following formula when substituting σ'_3 with Equ. (79):

$$0 = 2\tan^{-1}\left(\frac{c' + \sqrt{c'^2 + \sigma'_1\sigma'_3}}{\sigma'_3}\right) - \frac{1}{2}\pi - \varphi' \qquad (80)$$

If the resulted value of σ'_1 is again employed in Equ. (79), the required σ'_3 can be taken into account for Equ. (44 - 46). Finally the first effective stress σ'_1 associated to the yield surface at any orientation ($-30° \leq \theta \leq +30°$) is computed as explained earlier.

Later investigations have shown difficulties in the generation of the yield surface at low stress states once a cohesive material is applied. Both approaches are tested with the aid of a numerical direct simple shear test in the *SoilTest* option in Plaxis 2D. Although the original approach according to Equ. (49) coincides in the triaxial compression and extension state, no stress state in between shows reasonable results. There the equivalent friction angle φ'_{mc} is far too small. Hence the developing stress path would exceed the yield surface, though this is unfeasible. The modified approach related to Equ. (78) gives unreliable results at small stress states. But on the contrary if Equ. (78)

is applied, the stress path obtained in the numerical DSS with an initial vertical stress of 30 kN/m² and 100 kN/m² hits the yield surface. It could be that the unexpected result is explainable by the computation of σ_1'. Therefore it is suggested by the author to investigate those uncertainties in future works.

Appendix B

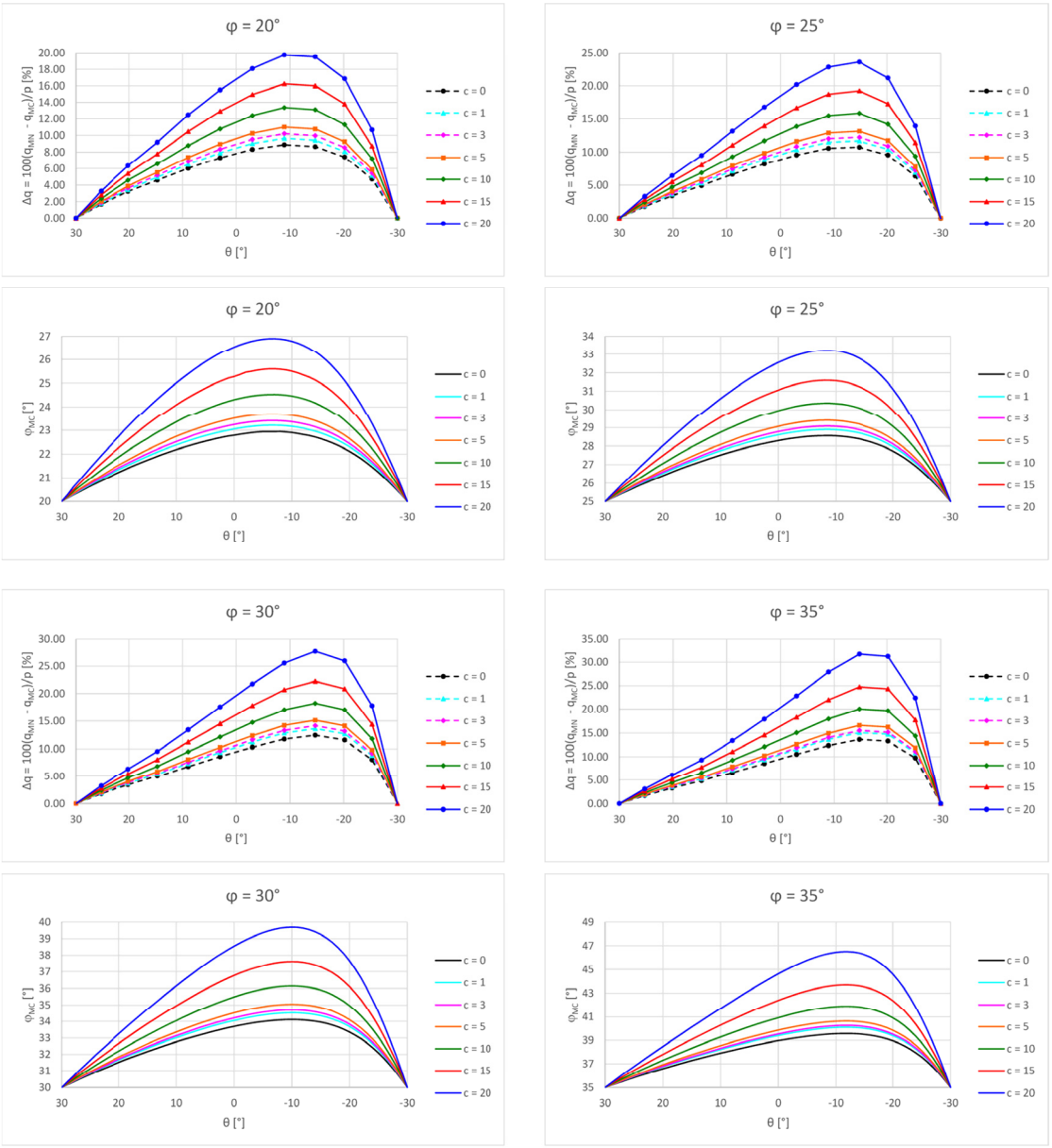

Fig. 85 Determination of Δq and φ'_{mc} for varying cohesion and friction angle

Appendix C

Tab. 20 Input parameters of corresponding constitutive models

Parameter	Symbol	Value	Unit
Applied to MC			
Young´s modulus	E'	4.00E+04	[kN/m²]
Oedometer modulus	E_{oed}	5.39E+04	[kN/m²]
Shear modulus	G	1.54E+04	[kN/m²]
Applied to MN			
Reference un- / reloading stiffness	E_{ur}^{ref}	5.39E+04	[kN/m²]
Reference secant stiffness in triaxial test	E_{50}^{ref}	1.80E+04	[kN/m²]
Power for stress-level dependency of stiffness	m	0.5	[-]
Reference stress for stiffness	p_{ref}	100	[kN/m²]
Failure ratio	R_f	0.9	[-]
Tensile strength	σ_t	0[1)]	[kN/m²]
Ratio of shear moduli	G_0/G_{ur}	1	[-]
Threshold shear strain	$\gamma_{0.7}$	1.30E-04	[-]
Skempton coefficient	B	0.98	[-]
Model Switch	Model SW	2	[-]
Applied to LE			
Young´s modulus	E'	4.00E+04	[kN/m²]

Parameter	Symbol	Value	Unit
Applied to HS			
Reference secant stiffness in triaxial test	E_{50}^{ref}	7.40E+05	[kN/m²]
Reference tangent stiffness for primary oedometer loading	E_{oed}^{ref}	7.40E+05	[kN/m²]
Reference un- / reloading stiffness	E_{ur}^{ref}	2.22E+06	[kN/m²]
Power for stress-level dependency of stiffness	m	0.5	[-]
Reference stress for stiffness	p_{ref}	100	[kN/m²]
Failure ratio	R_f	0.9	[-]
Tensile strength	σ_t	0	[kN/m²]
Poisson´s ratio for un- / reloading	ν_{ur}	0.2	[-]
Coefficient of lateral earth pressure for normally consolidated stress state	K_0^{nc}	$1-\sin\varphi'$	[-]
Applied to HSS			
Reference secant stiffness in triaxial test	E_{50}^{ref}	7.40E+05	[kN/m²]
Reference tangent stiffness for primary oedometer loading	E_{oed}^{ref}	7.40E+05	[kN/m²]
Reference un- / reloading stiffness	E_{ur}^{ref}	2.22E+06	[kN/m²]
Power for stress-level dependency of stiffness	m	0.5	[-]
Threshold shear strain	$\gamma_{0.7}$	1.50E-04	[-]
Reference shear modulus at very small strain	G_0^{ref}	2.78E+06	[kN/m²]
Reference stress for stiffness	p_{ref}	100	[kN/m²]
Failure ratio	R_f	0.9	[-]
Tensile strength	σ_t	0	[kN/m²]
Poisson´s ratio for un- / reloading	ν_{ur}	0.2	[-]
Coefficient of lateral earth pressure for normally consolidated stress state	K_0^{nc}	$1-\sin\varphi'$	[-]

[1)] Only valid for the first runs. After a sensitivity analysis this value was increased to 10E+6

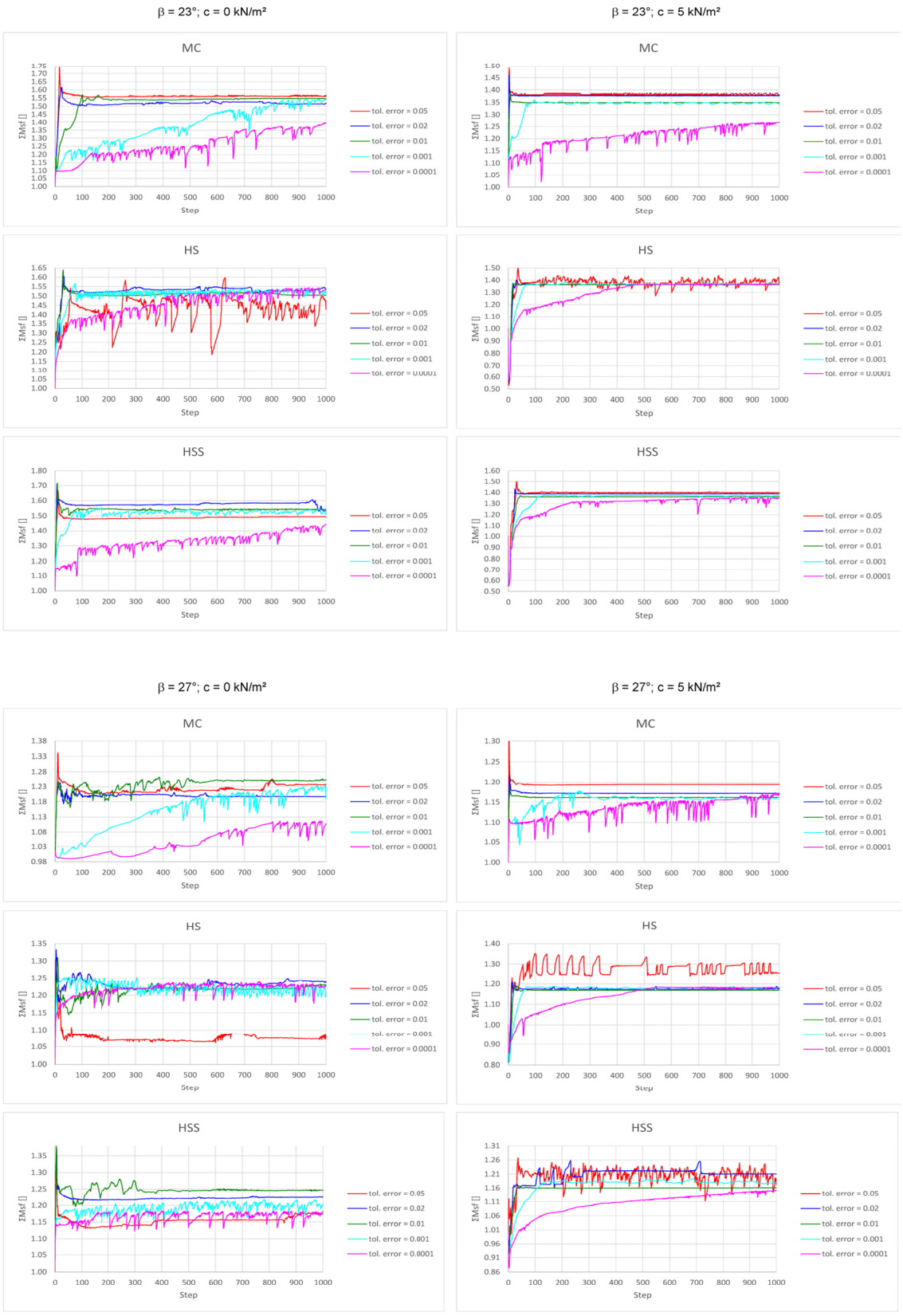

Fig. 86 Effect of tolerated error depending on the constitutive model, slope inclination and cohesion

Appendix D

Tab. 21 Limiting parameters of SRFEA

Material	Initial				SRFEA - MC									SRFEA - MN			100 · (MC-MN)/MC
					ψ = const.			ψ_{red} = $\tan^{-1}(\tan\psi_{input}/FOS)$			ψ_{red} = f { φ }			ψ_{red} = f { φ }			
	α	φ	ψ	FOS	φ	ψ	FOS	φ	ψ	FOS	φ	ψ	FOS	φ	ψ	FOS	Δ
	[°]	[°]	[°]	[-]	[°]	[°]	[-]	[°]	[°]	[-]	[°]	[°]	[-]	[°]	[°]	[-]	[%]
M_phi_20	20	20.0	20.0	1.01	20.0	20.0	1.01	20.0	20.0	1.01	20.0	20.0	1.01	-	-	-	-
M_phi_25	25	25.0	25.0	1.01	25.0	25.0	1.01	25.0	25.0	1.01	25.0	25.0	1.01	-	-	-	-
M_phi_30	30	30.0	30.0	1.01	30.0	30.0	1.01	30.0	30.0	1.01	30.0	30.0	1.01	-	-	-	-
M_phi_35	35	35.0	35.0	1.02	35.0	35.0	1.02	35.0	35.0	1.02	35.0	35.0	1.02	-	-	-	-
M_phi_40	40	40.0	40.0	1.02	40.0	40.0	1.02	40.0	40.0	1.02	40.0	40.0	1.02	-	-	-	-
M_phi_45	45	45.0	45.0	1.02	45.0	45.0	1.02	45.0	45.0	1.02	45.0	45.0	1.02	-	-	-	-
M_phi_50	50	50.0	50.0	1.02	50.0	50.0	1.02	50.0	50.0	1.02	50.0	50.0	1.02	-	-	-	-
M_phi-30_20	20	25.0	0.0	1.24	20.7	0.0	1.00	20.7	0.0	1.00	20.7	0.0	1.00	17.9	0.0	1.01	13.40
M_phi-30_25	25	30.0	0.0	1.13	27.1	0.0	1.02	27.1	0.0	1.02	27.1	0.0	1.02	23.3	0.0	1.02	13.94
M_phi-30_30	30	35.0	5.0	1.11	32.2	5.0	1.01	32.2	4.5	1.00	32.7	2.7	0.99	29.2	0.0	1.01	10.70
M_phi-30_35	35	40.0	10.0	1.10	37.4	10.0	1.00	37.4	9.1	0.99	37.9	7.9	1.00	35.5	5.5	1.00	6.41
M_phi-30_40	40	45.0	15.0	1.09	43.1	15.0	1.01	43.1	14.1	1.01	43.9	13.9	1.01	-	-	-	-
M_phi-30_45	45	50.0	20.0	1.07	48.7	20.0	1.01	48.7	19.1	1.00	49.0	19.0	1.00	-	-	-	-
M_phi-30_50	50	55.0	25.0	1.04	54.1	25.0	1.02	54.3	24.5	1.00	54.3	24.3	1.00	-	-	-	-
M_phi/3_20	20	25.0	8.3	1.29	19.9	8.3	1.00	19.9	6.5	0.996	20.20	6.7	1.01	18.0	6.00	1.02	10.89
M_phi/3_25	25	30.0	10.0	1.22	25.3	10.0	1.00	25.3	8.2	1.002	25.30	8.4	1.01	22.4	7.47	1.00	11.46
M_phi/3_30	30	35.0	11.7	1.17	31.0	11.7	1.00	31.0	10.0	1.003	30.90	10.3	1.00	27.5	9.18	1.00	10.87
M_phi/3_35	35	40.0	13.3	1.11	37.0	13.3	1.02	37.0	12.0	1.008	37.30	12.4	1.01	33.1	11.02	1.00	11.34
M_phi/3_40	40	45.0	15.0	1.09	43.1	15.0	1.00	43.1	14.1	1.009	43.42	14.5	1.02	39.0	13.00	1.00	10.18
M_phi/3_45	45	55.0	18.3	1.23	49.3	18.3	1.02	49.3	15.1	1.024	50.10	16.7	0.99	-	-	-	-
M_phi/3_50	50	65.0	21.7	1.47	55.6	21.7	1.01	59.7	17.7	1.005	57.93	19.3	1.01	-	-	-	-
M_phi/4_20	20	25.0	6.3	1.28	20.0	6.3	1.00	20.0	4.9	0.99	20.00	5.0	1.00	17.8	4.45	1.01	11.00
M_phi/4_25	25	30.0	7.5	1.20	25.7	7.5	1.02	25.7	6.3	1.01	25.50	6.4	1.01	22.7	5.68	1.01	10.98
M_phi/4_30	30	35.0	8.8	1.14	31.9	8.8	1.02	31.9	7.8	1.01	31.80	8.0	1.02	28.5	7.13	1.01	10.38
M_phi/4_35	35	40.0	10.0	1.10	37.4	10.0	1.00	37.4	9.1	0.99	37.50	9.4	1.01	34.2	8.55	1.01	8.80
M_phi/4_40	40	45.0	11.3	1.03	44.3	11.3	1.02	44.3	11.0	0.99	44.40	11.1	1.00	40.9	10.23	1.02	7.88
M_phi/4_45	45	55.0	13.8	1.11	51.9	13.8	1.01	52.9	12.3	0.99	53.18	13.3	1.01	-	-	-	-
M_phi/4_50	50	65.0	16.3	1.11	61.0	16.3	1.02	60.9	14.3	1.01	63.28	15.8	1.01	-	-	-	-
M_0_20	20	25.0	0.0	1.24	20.7	0.0	1.00	20.7	0.0	1.00	20.67	0.0	1.00	17.9	0.00	1.01	13.40
M_0_25	25	30.0	0.0	1.13	27.0	0.0	1.00	27.0	0.0	1.00	27.02	0.0	1.00	23.3	0.00	1.02	13.77
M_0_30	30	35.0	0.0	1.05	33.6	0.0	1.01	33.6	0.0	1.01	33.60	0.0	1.01	29.2	0.00	1.01	13.09
M_0_35	35	40.0	0.0	<1.00	42.3	0.0	1.00	42.3	0.0	1.00	42.31	0.0	1.00	-	-	-	-
M_0_40	40	45.0	0.0	-	51.1	0.0	1.02	51.1	0.0	1.02	51.10	0.0	1.02	-	-	-	-
M_0_45	45	55.0	0.0	-	-	-	-	-	-	-	-	-	-	-	-	-	-
M_0_50	50	66.0	0.0	-	-	-	-	-	-	-	-	-	-	-	-	-	-

Appendix E

Tab. 22 Parameter study - GHS

ψ = φ/3; β = 20°														
Parameter \ Trial		1	2	3	4	5	6	7	8	9	10	11	12	13
Plaxis Model		MC - GHS	MC - GHS	MC - GHS	MC - GHS	MC - GHS	MC - GHS	MC - GHS	MC - GHS	MC - GHS	MC - GHS	MC - GHS	MC - GHS	MC - GHS
Calc. Type		Gravity Loading	Gravity Loading	Gravity Loading	Gravity Loading	Gravity Loading	Gravity Loading	Gravity Loading	Gravity Loading	Gravity Loading	Gravity Loading	Gravity Loading	Gravity Loading	Gravity Loading
E_{50}	[kN/m²]	5.00E+01	5.00E+01	5.00E+01	5.00E+01	5.00E+01	5.00E+01	5.00E+01	5.00E+01	5.00E+01	5.00E+01	5.00E+01	5.00E+01	5.00E+01
E_{oed}	[kN/m²]	5.00E+01	5.00E+01	5.00E+01	5.00E+01	5.00E+01	5.00E+01	5.00E+01	5.00E+01	5.00E+01	5.00E+01	5.00E+01	5.00E+01	5.00E+01
E_{ur}^{ref}	[kN/m²]	1.50E+02	1.50E+02	1.50E+02	1.50E+02	1.50E+02	1.50E+02	1.50E+02	1.50E+02	1.50E+02	1.50E+02	1.50E+02	1.50E+02	1.50E+02
ν_{ur}	[-]	0.2	0.2	0.2	0.2	0.2	0.2	0.2	0.2	0.2	0.2	0.2	0.2	0.2
φ	[°]	35.4	35.4	35.4	35.4	35.4	35.4	35.4	35.4	35.4	35.4	35.4	35.4	35.4
c^{ref}	[kN/m²]	0	0	0	0	0	0	0	0	0	0	0	0	0
ψ	[°]	11.8	11.8	11.8	11.8	11.8	11.8	11.8	11.8	11.8	11.8	11.8	11.8	11.8
m	[-]	0.5	0.5	0.5	0.5	0.5	0.5	0.5	0.5	0.5	0.5	0.5	0.5	0.5
p_{ref}	[kN/m²]	100	100	100	100	100	100	100	100	100	100	100	100	100
R_f	[-]	0.9	0.9	0.9	0.9	0.9	0.9	0.9	0.9	0.9	0.9	0.9	0.9	0.9
σ_t	[kN/m²]	0.0	0.0	0.0	0.0	0.0	0.0	0.0	0.0	0.0	0.0	0.0	0.0	0.0
G_0^{ref}	[kN/m²]	1.88E+02	1.88E+02	1.88E+02	1.88E+02	1.88E+02	1.88E+02	1.88E+02	1.88E+02	1.88E+02	1.88E+02	1.88E+02	1.88E+02	1.88E+02
$\gamma_{0.7}$	[-]	1.50E-04	1.50E-04	1.50E-04	1.50E-04	1.50E-04	1.50E-04	1.50E-04	1.50E-04	1.50E-04	1.50E-04	1.50E-04	1.50E-04	1.50E-04
Failure	[-]	0	0	0	0	0	0	0	0	0	0	0	0	0
OCR	[-]	1	1	1	1	1	1	1	1	1	1	1	1	1
POP	[-]	0	0	0	0	0	0	0	0	0	0	0	0	0
K_0	[-]	0.4207	0.4207	0.4207	0.4207	0.4207	0.4207	0.4207	0.4207	0.4207	0.4207	0.4207	0.4207	0.4207
K_0^{nc}	[-]	0.4207	0.4207	0.4207	0.4207	0.4207	0.4207	0.4207	0.4207	0.4207	0.4207	0.4207	0.4207	0.4207
Sress d.Stiffness		0	0	0	0	1	1	1	2	2	2	2	2	2
Strain d. Stiffness		0	0	0	0	0	0	0	0	0	0	0	0	0
Plasticity Model		0	1	4	3	0	1	4	0	0	0	0	1	4
Stress d. Formula		0	0	0	0	0	0	0	0	1	2	3	0	0
M_{sf}	[-]	0.1	0.1	0.1	0.1	0.1	0.1	0.1	0.1	0.1	0.1	0.1	0.1	0.1
ε_{tol}	[-]	0.01	0.01	0.01	0.01	0.01	0.01	0.01	0.01	0.01	0.01	0.01	0.01	0.01
FOS	[-]	52.85	<< 1.00	1001.00	Safety Collapse	Initial Collapse	Initial Collapse	Safety Collapse	20.45	Safety Collapse	Safety Collapse	237.50	486.10	12240.00

failure (0:MC or 1:M-N)	0.000
OCR	1.000
POP	0.000
k_0	0.6547
k_0^{nc}	0.6547
ν_u	0.000
M (internal)	0.000
K_s/K_c (internal)	0.000
G_{50}^{ref} (internal)	0.000
Stress Dependent Stiffness	1.000
Strain Dependent Stiffness	0.000
Plasticity Model	1.000
Stress Dependency Formula	0.000

Choose material model:
0 = MC
1 = MN

Stress Dependent Stiffness:
0 = Stiffness stays constant
1 = Stiffness is constant during phase but based on the stresses at the beginning of the phase
2 = Updates ervery calculation step based on „Stress Dependency Formula“

Strain Dependent Stiffness:
0 = HS model
1 = HSS model

Plasticity Model:
1 = only MC failure criterion
2 = shear hardening + MC failure
3 = cap hardening + MC failure
4 = shear + cap hardening + MC failure (HSS)

Stress Dependency Formula:
0 = based on σ_3 and strength parameters
1 = based on σ_3 and pre-consolidation stress
2 = based on mean effective stress and pre-consolidation stress

Appendix F

M_phi_3_35 - c = 0.1								
Parameter \ Trial		1	2	3	4	5	6	7
Plaxis Model		MC-STD	MC-GR	MC-LE	MC-K0	MN-GR	MN-LE	MN-K0
Material Model		MC	MC	LE / MC	MC	MN	LE / MN	MN
Calc. Type		Gravity Loading	Gravity Loading	Gravity Loading	K0 + Nilstep	Gravity Loading	Gravity Loading	K0 + Nilstep
E'	[kN/m²]	4.00E+04	-	-	-	-	-	-
E_{oed}	[kN/m²]	5.39E+04	-	-	-	-	-	-
E_{ur}^{ref}	[kN/m²]	-	5.39E+04	5.39E+04	5.39E+04	5.39E+04	5.39E+04	5.39E+04
ν	[–]	0.3	0.3	0.3	0.3	0.3	0.3	0.3
φ	[°]	37.3	37.3	37.3	37.3	37.3	37.3	37.3
cref	[kN/m²]	0.1	0.1	0.1	0.1	0.1	0.1	0.1
ψ	[°]	12.4	12.4	12.4	12.4	12.4	12.4	12.4
m	[-]	-	0.5	0.5	0.5	0.5	0.5	0.5
p_{ref}	[kN/m²]	-	100	100	100	100	100	100
R_f	[-]	-	0.9	0.9	0.9	0.9	0.9	0.9
σ_t	[kN/m²]	0	0	0	0	0	0	0
E_{50}^{ref}	[kN/m²]	-	1.80E+04	1.80E+04	1.80E+04	1.80E+04	1.80E+04	1.80E+04
G_0/G_{ur}	[-]	-	1	1	1	1	1	1
$\gamma_{0.7}$	[-]	-	1.30E-04	1.30E-04	1.30E-04	1.30E-04	1.30E-04	1.30E-04
Model SW		-	1	1	1	2	2	2
Skempton		-	0.98	0.98	0.98	0.98	0.98	0.98
FoS	[-]	1.06	1.04	1.04	1.03	Initial Collapse	Safety Collapse	Nilstep Collapse

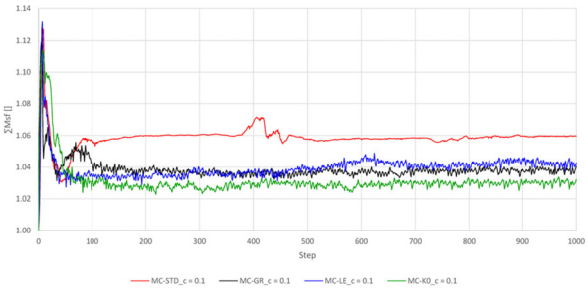

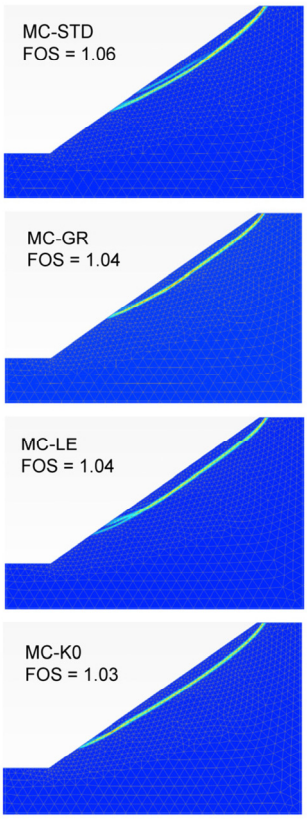

Fig. 87 Analysis of the user-defined material model with c = 0.1 kN/m²

M_phi_3_35 - c = 1.0								
Parameter \ Trial		1	2	3	4	5	6	7
Plaxis Model		MC-STD	MC-GR	MC-LE	MC-K0	MN-GR	MN-LE	MN-K0
Material Model		MC	MC	LE / MC	MC	MN	LE / MN	MN
Calc. Type		Gravity Loading	Gravity Loading	Gravity Loading	K0 + Nilstep	Gravity Loading	Gravity Loading	K0 + Nilstep
E'	[kN/m²]	4.00E+04	-	-	-	-	-	-
E_{oed}	[kN/m²]	5.39E+04	-	-	-	-	-	-
E_{ur}^{ref}	[kN/m²]	-	5.39E+04	5.39E+04	5.39E+04	5.39E+04	5.39E+04	5.39E+04
ν	[–]	0.3	0.3	0.3	0.3	0.3	0.3	0.3
φ	[°]	37.3	37.3	37.3	37.3	37.3	37.3	37.3
cref	[kN/m²]	1.0	1.0	1.0	1.0	1.0	1.0	1.0
ψ	[°]	12.4	12.4	12.4	12.4	12.4	12.4	12.4
m	[-]	-	0.5	0.5	0.5	0.5	0.5	0.5
p_{ref}	[kN/m²]	-	100	100	100	100	100	100
R_f	[-]	-	0.9	0.9	0.9	0.9	0.9	0.9
σ_t	[kN/m²]	0	0	0	0	0	0	0
E_{50}^{ref}	[kN/m²]	-	1.80E+04	1.80E+04	1.80E+04	1.80E+04	1.80E+04	1.80E+04
G_0/G_{ur}	[-]	-	1	1	1	1	1	1
$\gamma_{0.7}$	[-]	-	1.30E-04	1.30E-04	1.30E-04	1.30E-04	1.30E-04	1.30E-04
Model SW		-	1	1	1	2	2	2
Skempton		-	0.98	0.98	0.98	0.98	0.98	0.98
FoS	[-]	1.19	1.18	1.18	1.20	Initial Collapse	Safety Collapse	Nilstep Collapse

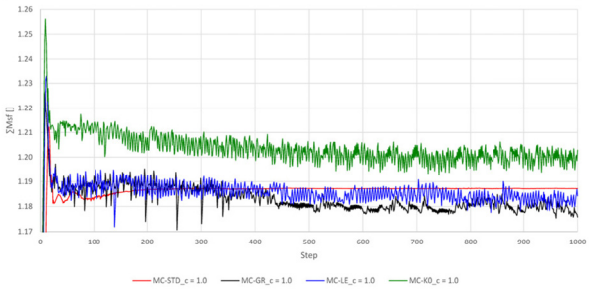

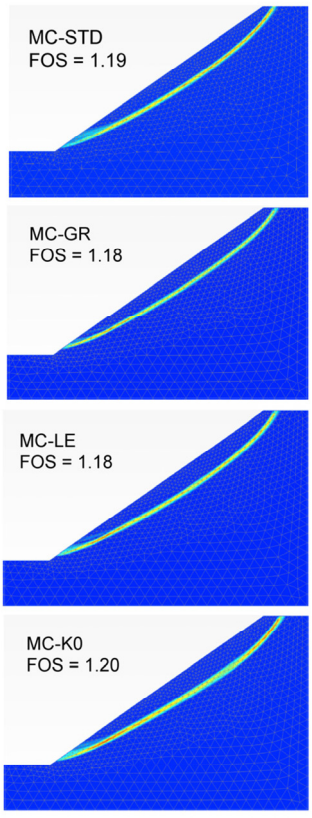

Fig. 88 Analysis of the user-defined material model with c = 1.0 kN/m²

M_phi_3_35 - c = 10								
Parameter \ Trial		1	2	3	4	5	6	7
Plaxis Model		MC STD	MC GR	MC LE	MC K0	MN GR	MN LE	MN K0
Material Model		MC	MC	LE / MC	MC	MN	LE / MN	MN
Calc. Type		Gravity Loading	Gravity Loading	Gravity Loading	K0 + Nilstep	Gravity Loading	Gravity Loading	K0 + Nilstep
E'	[kN/m²]	4.00E+04	-	-	-	-	-	-
E_{oed}	[kN/m²]	5.39E+04	-	-	-	-	-	-
E_{ur}^{ref}	[kN/m²]	-	5.39E+04	5.39E+04	5.39E+04	5.39E+04	5.39E+04	5.39E+04
ν	[–]	0.3	0.3	0.3	0.3	0.3	0.3	0.3
φ	[°]	37.3	37.3	37.3	37.3	37.3	37.3	37.3
cref	[kN/m²]	10.0	10.0	10.0	10.0	10.0	10.0	10.0
ψ	[°]	12.4	12.4	12.4	12.4	12.4	12.4	12.4
m	[-]	-	0.5	0.5	0.5	0.5	0.5	0.5
p_{ref}	[kN/m²]	-	100	100	100	100	100	100
R_f	[-]	-	0.9	0.9	0.9	0.9	0.9	0.9
σ_t	[kN/m²]	0	0	0	0	0	0	0
E_{50}^{ref}	[kN/m²]	-	1.80E+04	1.80E+04	1.80E+04	1.80E+04	1.80E+04	1.80E+04
G_0/G_{ur}	[-]	-	1	1	1	1	1	1
$\gamma_{0.7}$	[-]	-	1.30E-04	1.30E-04	1.30E-04	1.30E-04	1.30E-04	1.30E-04
Model SW		-	1	1	1	2	2	2
Skempton		-	0.98	0.98	0.98	0.98	0.98	0.98
FoS	[-]	1.90	1.89	1.88	1.89	Initial Collapse	Plastic Collapse	Nilstep Collapse

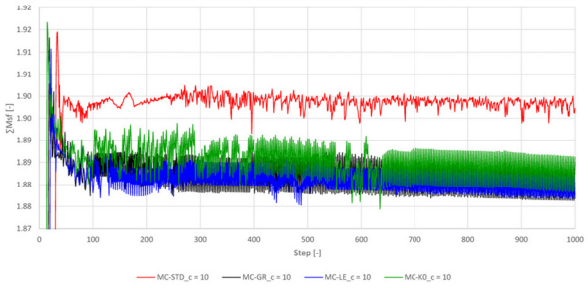

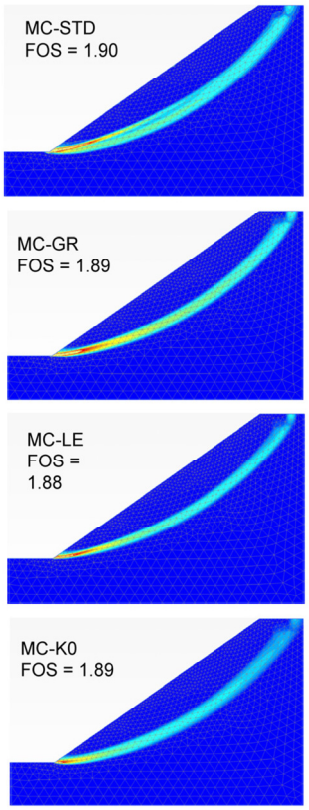

Fig. 89 Analysis of the user-defined material model with c = 10 kN/m²

Appendix G

Step	σ_1	σ_2	σ_3	p'	q'	φ'	c'	θ
	[kN/m²]	[kN/m²]	[kN/m²]	[kN/m²]	[kN/m²]	[°]	[kPa]	[°]
Step 3	27.89	17.67	13.67	19.74	12.70	10.7	4.45	-14.16
Step 7	26.52	16.82	13.00	18.78	12.07	10.7	4.45	-14.09
Step 14	24.34	15.01	11.80	17.05	11.28	10.7	4.45	-15.76
Step 1	22.84	12.99	10.75	15.53	11.14	10.7	4.45	-19.95
Step 127	23.70	14.02	7.05	14.93	14.48	10.7	4.45	-5.37
Step 253	24.28	17.28	7.59	16.38	14.52	10.7	4.45	5.30
Step 379	24.49	17.42	7.69	16.53	14.61	10.7	4.45	5.21
Step 505	24.49	17.42	7.74	16.55	14.56	10.7	4.45	5.13
Step 631	24.28	17.26	7.58	16.37	14.52	10.7	4.45	5.25
Step 754	24.07	17.11	7.45	16.21	14.46	10.7	4.45	5.37
Step 877	24.25	17.21	7.56	16.34	14.51	10.7	4.45	5.17
Step 1000	24.32	17.31	7.61	16.41	14.53	10.7	4.45	5.33

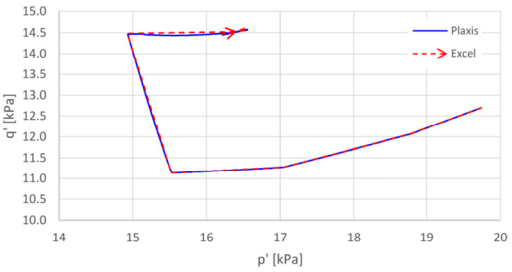

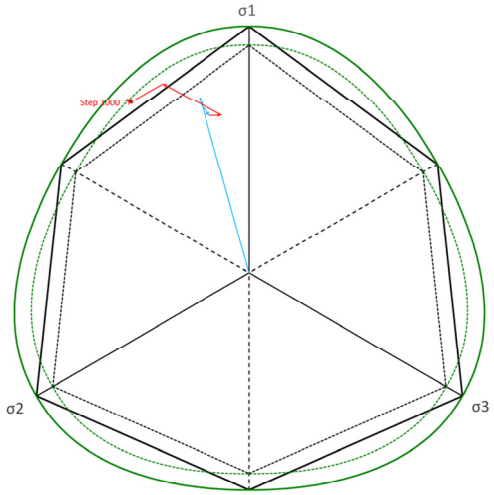

Display Stress Point:	Step 1000	
Δ (MC-Point)	-1.75	[kN/m²]
Δ (MN-Point)	0.16	[kN/m²]
Δ (MN - MC)	1.91	[kN/m²]

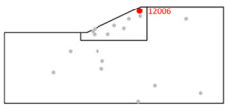

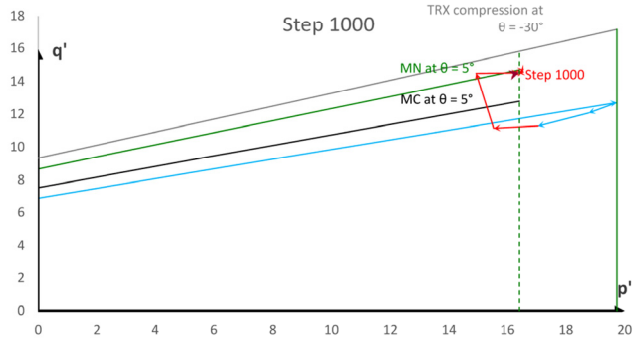

Fig. 90 Comparison with SoilTest – MN-LE (Example 2)

Step	σ_1	σ_2	σ_3	p'	q'	φ'	c'	θ
	[kN/m²]	[kN/m²]	[kN/m²]	[kN/m²]	[kN/m²]	[°]	[kPa]	[°]
Step 1	76.26	45.00	45.00	55.42	31.26	10.7	4.45	-30.00
Step 2	76.26	47.84	45.00	56.37	29.94	10.7	4.45	-25.28
Step 3	76.26	50.68	45.00	57.31	28.84	10.7	4.45	-20.17
Step 4	76.26	53.53	45.00	58.26	27.99	10.7	4.45	-14.70
Step 5	76.26	56.37	45.00	59.21	27.41	10.7	4.45	-8.95
Step 6	76.26	59.21	45.00	60.16	27.11	10.7	4.45	-3.00
Step 7	76.26	62.05	45.00	61.10	27.11	10.7	4.45	3.01
Step 8	76.26	64.89	45.00	62.05	27.41	10.7	4.45	8.95
Step 9	76.26	67.74	45.00	63.00	27.99	10.7	4.45	14.71
Step 10	76.26	70.58	45.00	63.95	28.84	10.7	4.45	20.18
Step 11	76.26	73.42	45.00	64.89	29.94	10.7	4.45	25.29
Step 12	76.26	76.26	45.00	65.84	31.26	10.7	4.45	30.00

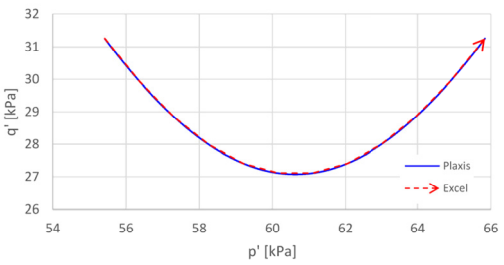

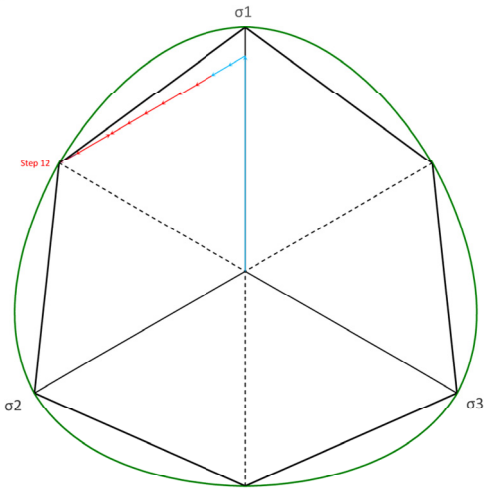

Display Stress Point:	Step 12	
Δ (MC-Point)	0.00	[kN/m²]
Δ (MN-Point)	0.02	[kN/m²]
Δ (MN - MC)	0.02	[kN/m²]

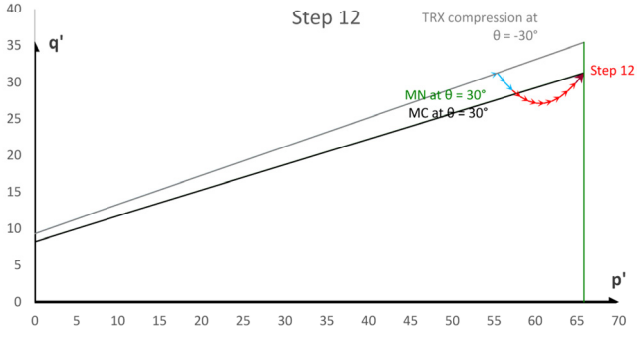

Fig. 91 Comparison with SoilTest – arbitrary stress path

Appendix H

- **SP 16986**

Step	σ_1 [kN/m²]	σ_2 [kN/m²]	σ_3 [kN/m²]	p' [kN/m²]	q' [kN/m²]	φ' [°]	c' [kPa]	θ [°]
Step 5	4.91	1.91	1.46	2.76	3.25	37.3	0.00	-23.1
Step 8	12.37	4.81	3.67	6.95	8.19	37.3	0.00	-23.1
Step 11	35.97	14.00	10.68	20.22	23.80	37.3	0.00	-23.1
Step 1	36.09	14.02	10.65	20.26	23.94	37.3	0.00	-23.0
Step 127	33.71	12.92	9.34	18.66	22.79	37.3	0.00	-22.2
Step 253	33.42	12.76	9.13	18.44	22.69	37.3	0.00	-22.0
Step 379	36.49	13.69	9.13	19.77	25.39	37.3	0.00	-21.1
Step 505	36.75	13.78	9.19	19.91	25.57	37.3	0.00	-21.1
Step 631	36.50	13.68	9.10	19.76	25.42	37.3	0.00	-21.0
Step 754	35.54	13.33	8.91	19.26	24.72	37.3	0.00	-21.1
Step 877	33.51	12.56	8.34	18.14	23.34	37.3	0.00	-21.0
Step 1000	32.59	12.21	8.12	17.64	22.70	37.3	0.00	-21.0

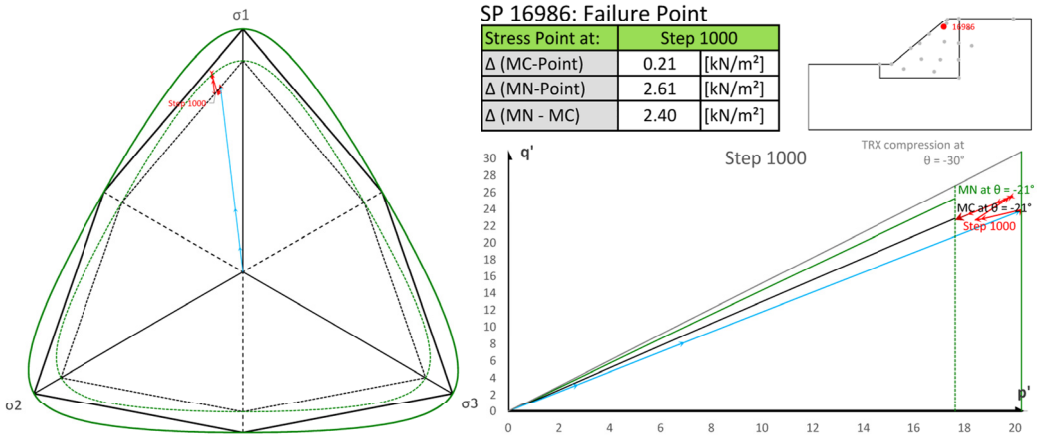

Fig. 92 MC-STD: stress path of SP 16986

Step	σ_1 [kN/m²]	σ_2 [kN/m²]	σ_3 [kN/m²]	p' [kN/m²]	q' [kN/m²]	φ' [°]	c' [kPa]	θ [°]
Step 4	32.76	13.38	11.83	19.32	20.19	37.3	0.00	-26.2
Step 11	33.75	13.55	11.43	19.58	21.34	37.3	0.00	-25.1
Step 26	36.37	14.11	10.65	20.38	24.18	37.3	0.00	-22.9
Step 1	36.51	14.14	10.61	20.42	24.33	37.3	0.00	-22.8
Step 127	32.59	12.51	9.11	18.07	21.98	37.3	0.00	-22.3
Step 253	31.99	12.30	9.00	17.76	21.53	37.3	0.00	-22.4
Step 379	32.93	12.49	8.71	18.04	22.57	37.3	0.00	-21.7
Step 505	34.38	13.00	8.94	18.77	23.67	37.3	0.00	-21.5
Step 631	35.05	13.36	9.48	19.30	23.87	37.3	0.00	-21.9
Step 754	34.98	13.46	9.88	19.44	23.52	37.3	0.00	-22.4
Step 877	35.09	13.77	10.82	19.89	22.94	37.3	0.00	-23.6
Step 1000	35.36	13.95	11.15	20.15	22.94	37.3	0.00	-23.9

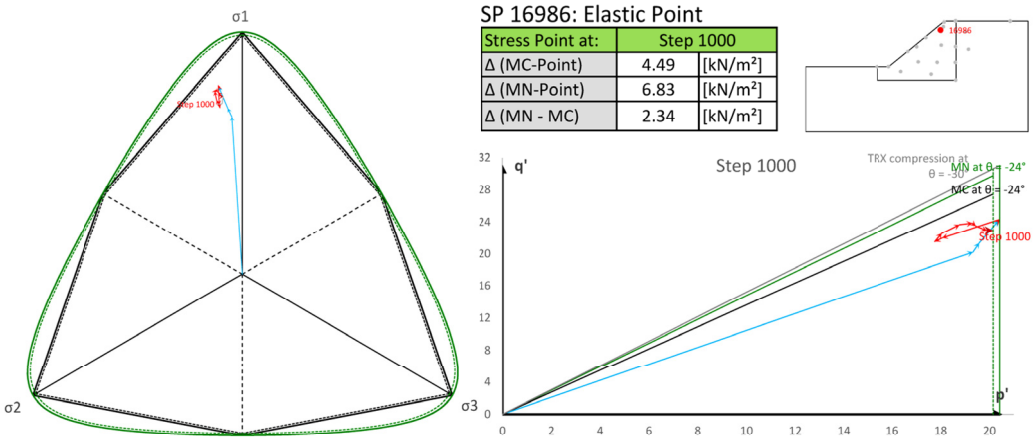

Fig. 93 MC-LE: stress path of SP 16986

Step	σ_1	σ_2	σ_3	p'	q'	φ'	c'	θ
	[kN/m²]	[kN/m²]	[kN/m²]	[kN/m²]	[kN/m²]	[°]	[kPa]	[°]
Step 5	32.62	13.35	11.89	19.29	20.04	37.3	0.00	-26.4
Step 8	33.38	13.52	11.68	19.53	20.84	37.3	0.00	-25.6
Step 11	35.15	13.92	11.25	20.10	22.69	37.3	0.00	-24.1
Step 1	35.22	13.93	11.23	20.13	22.76	37.3	0.00	-24.1
Step 127	37.51	14.17	9.37	20.35	26.07	37.3	0.00	-20.8
Step 253	36.00	16.73	8.79	20.51	24.23	37.3	0.00	-13.5
Step 379	35.97	16.97	8.76	20.57	24.17	37.3	0.00	-12.9
Step 505	35.51	18.15	8.79	20.82	23.48	37.3	0.00	-9.8
Step 631	35.51	18.16	8.79	20.82	23.48	37.3	0.00	-9.8
Step 754	35.34	18.44	8.73	20.84	23.32	37.3	0.00	-8.9
Step 877	35.34	18.78	8.73	20.95	23.28	37.3	0.00	-8.0
Step 1000	35.44	19.13	8.71	21.09	23.33	37.3	0.00	-7.3

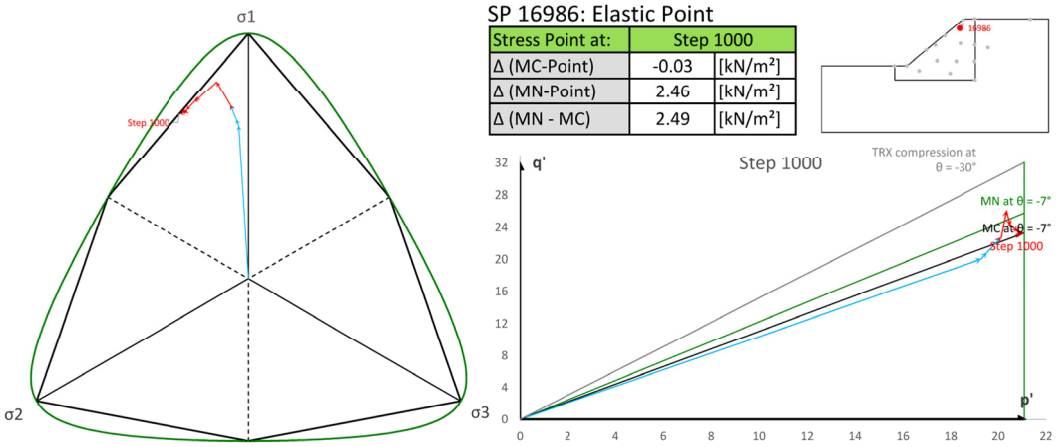

Fig. 94 MN-LE-M1: stress path of SP 16986

Step	σ_1	σ_2	σ_3	p'	q'	φ'	c'	θ
	[kN/m²]	[kN/m²]	[kN/m²]	[kN/m²]	[kN/m²]	[°]	[kPa]	[°]
Step 3	32.67	13.36	11.87	19.30	20.10	33.1	0.00	-26.3
Step 11	34.10	13.63	11.35	19.69	21.70	33.1	0.00	-24.8
Step 25	36.93	14.24	10.54	20.57	24.75	33.1	0.00	-22.6
Step 1	36.99	14.30	10.51	20.60	24.79	33.1	0.00	-22.4
Step 127	39.26	15.46	10.09	21.60	26.89	33.1	0.00	-20.0
Step 253	39.94	15.92	10.93	22.26	26.86	33.1	0.00	-20.7
Step 379	40.13	16.04	11.13	22.43	26.89	33.1	0.00	-20.9
Step 505	40.27	16.07	11.10	22.48	27.03	33.1	0.00	-20.8
Step 631	40.36	16.12	11.18	22.55	27.06	33.1	0.00	-20.9
Step 754	40.39	16.12	11.17	22.56	27.08	33.1	0.00	-20.9
Step 877	40.46	16.14	11.14	22.58	27.18	33.1	0.00	-20.8
Step 1000	40.54	16.18	11.21	22.65	27.19	33.1	0.00	-20.9

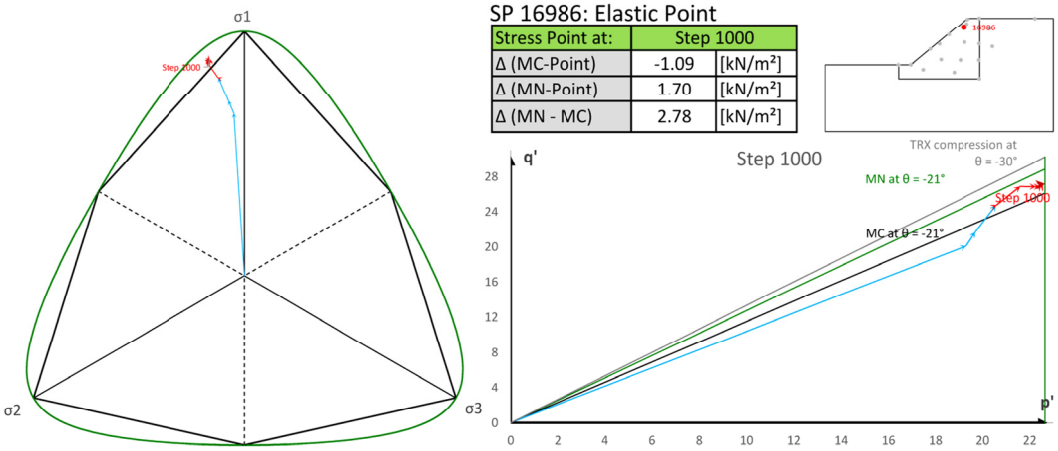

Fig. 95 MN-LE-M2: stress path of SP 16986

- **SP 17756**

Step	σ_1 [kN/m²]	σ_2 [kN/m²]	σ_3 [kN/m²]	p' [kN/m²]	q' [kN/m²]	φ' [°]	c' [kPa]	θ [°]
Step 5	3.39	1.39	1.24	2.00	2.07	37.3	0.00	-26.5
Step 8	8.53	3.50	3.13	5.05	5.23	37.3	0.00	-26.5
Step 11	24.80	10.17	9.09	14.69	15.20	37.3	0.00	-26.5
Step 1	24.83	10.17	9.06	14.68	15.24	37.3	0.00	-26.4
Step 127	27.47	10.72	8.27	15.48	18.10	37.3	0.00	-23.3
Step 253	28.37	10.64	7.11	15.37	19.73	37.3	0.00	-21.1
Step 379	30.07	11.27	7.49	16.28	20.94	37.3	0.00	-21.0
Step 505	29.29	10.98	7.30	15.85	20.40	37.3	0.00	-21.0
Step 631	29.09	10.90	7.25	15.75	20.26	37.3	0.00	-21.0
Step 754	29.42	11.03	7.33	15.93	20.49	37.3	0.00	-21.0
Step 877	29.66	11.11	7.39	16.05	20.67	37.3	0.00	-21.0
Step 1000	29.57	11.08	7.37	16.01	20.60	37.3	0.00	-21.0

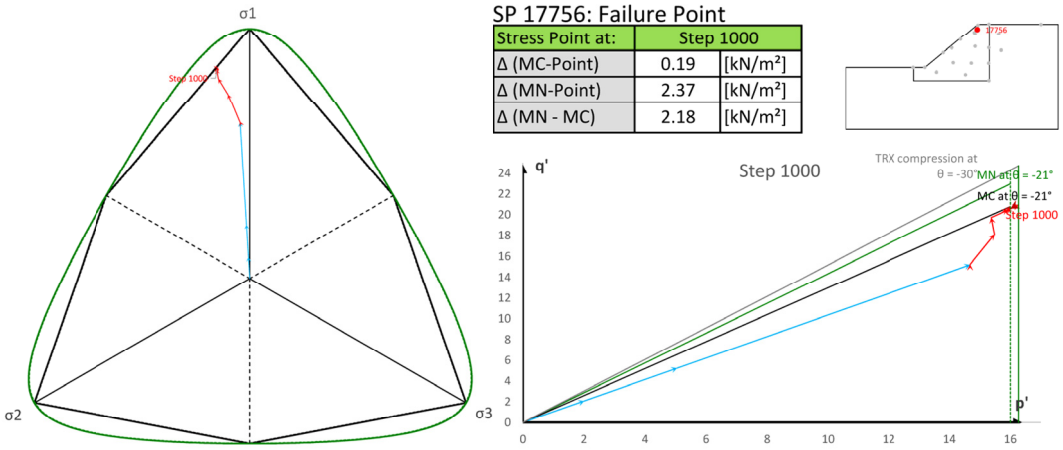

Fig. 96 MC-STD: stress path of SP 17756

Step	σ_1 [kN/m²]	σ_2 [kN/m²]	σ_3 [kN/m²]	p' [kN/m²]	q' [kN/m²]	φ' [°]	c' [kPa]	θ [°]
Step 4	25.03	10.51	10.01	15.18	14.78	37.3	0.00	-28.3
Step 11	24.61	10.27	9.63	14.83	14.67	37.3	0.00	-27.8
Step 26	25.29	10.30	9.06	14.88	15.65	37.3	0.00	-26.0
Step 1	25.34	10.31	9.03	14.89	15.71	37.3	0.00	-25.9
Step 127	28.12	10.79	7.85	15.59	18.97	37.3	0.00	-22.3
Step 253	26.79	10.15	7.05	14.66	18.39	37.3	0.00	-21.6
Step 379	27.44	10.28	6.82	14.85	19.13	37.3	0.00	-21.0
Step 505	27.04	10.12	6.70	14.62	18.86	37.3	0.00	-21.0
Step 631	26.70	10.03	6.74	14.49	18.54	37.3	0.00	-21.1
Step 754	26.27	10.04	7.20	14.50	17.82	37.3	0.00	-22.1
Step 877	25.26	9.71	7.12	14.03	16.99	37.3	0.00	-22.4
Step 1000	24.69	9.44	6.80	13.64	16.72	37.3	0.00	-22.1

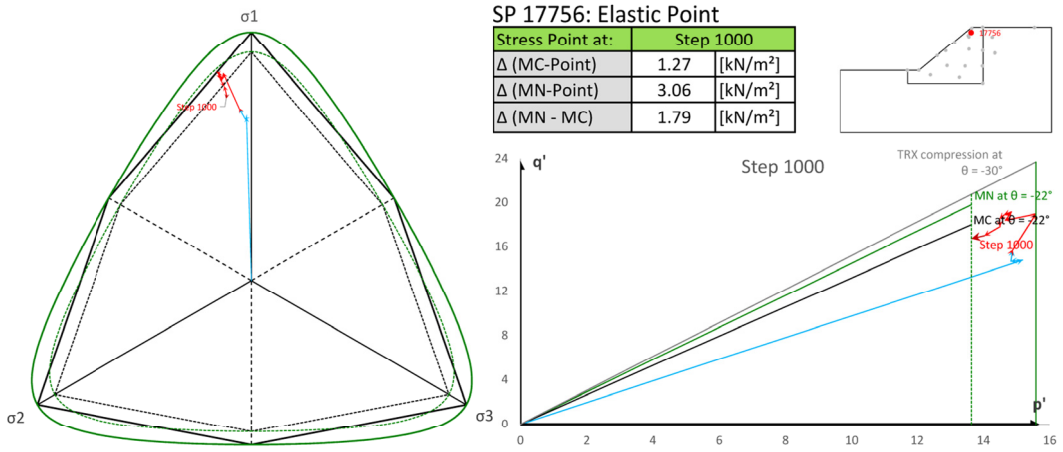

Fig. 97 MC-LE: stress path of SP 17756

Step	σ_1	σ_2	σ_3	p'	q'	φ'	c'	θ
	[kN/m²]	[kN/m²]	[kN/m²]	[kN/m²]	[kN/m²]	[°]	[kPa]	[°]
Step 5	25.14	10.55	10.04	15.24	14.84	37.3	0.00	-28.3
Step 8	24.89	10.42	9.85	15.05	14.77	37.3	0.00	-28.1
Step 11	25.12	10.38	9.50	15.00	15.19	37.3	0.00	-27.1
Step 1	25.14	10.39	9.49	15.01	15.22	37.3	0.00	-27.1
Step 127	26.65	10.46	8.21	15.10	17.43	37.3	0.00	-23.6
Step 253	27.50	10.57	7.75	15.27	18.50	37.3	0.00	-22.4
Step 379	27.72	10.65	7.79	15.39	18.67	37.3	0.00	-22.4
Step 505	28.00	10.68	7.58	15.42	19.06	37.3	0.00	-21.9
Step 631	28.19	10.71	7.51	15.47	19.28	37.3	0.00	-21.7
Step 754	28.35	10.73	7.43	15.50	19.48	37.3	0.00	-21.5
Step 877	28.45	10.82	7.36	15.54	19.59	37.3	0.00	-21.2
Step 1000	28.65	10.91	7.31	15.62	19.79	37.3	0.00	-20.9

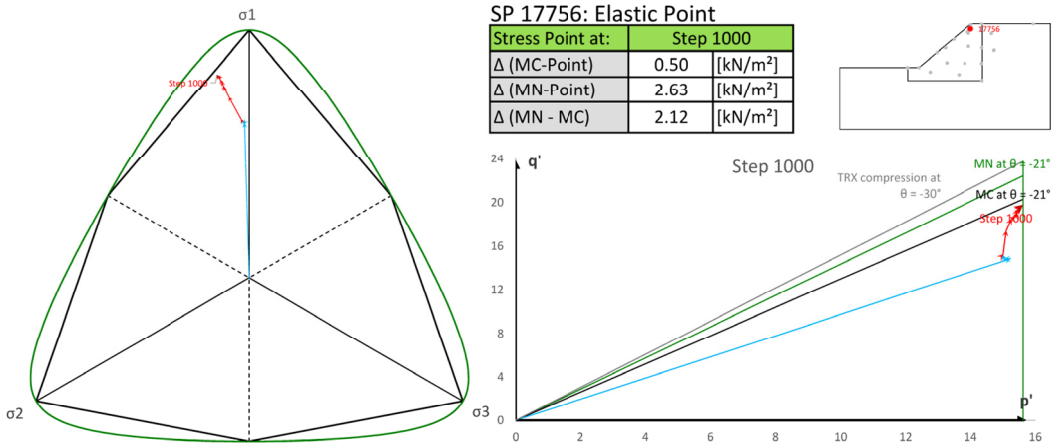

Fig. 98 MN-LE-M1: stress path of SP 17756

Step	σ_1	σ_2	σ_3	p'	q'	φ'	c'	θ
	[kN/m²]	[kN/m²]	[kN/m²]	[kN/m²]	[kN/m²]	[°]	[kPa]	[°]
Step 3	25.10	10.54	10.04	15.23	14.82	33.1	0.00	-28.3
Step 11	24.67	10.27	9.57	14.84	14.76	33.1	0.00	-27.6
Step 25	25.63	10.38	8.95	14.99	16.02	33.1	0.00	-25.6
Step 1	25.73	10.40	8.94	15.02	16.11	33.1	0.00	-25.5
Step 127	26.61	10.55	8.57	15.25	17.13	33.1	0.00	-24.2
Step 253	26.86	10.56	8.34	15.25	17.52	33.1	0.00	-23.7
Step 379	27.07	10.59	8.23	15.30	17.78	33.1	0.00	-23.4
Step 505	27.45	10.72	8.30	15.49	18.06	33.1	0.00	-23.3
Step 631	27.82	10.86	8.39	15.69	18.32	33.1	0.00	-23.3
Step 754	28.00	10.96	8.55	15.84	18.36	33.1	0.00	-23.5
Step 877	28.15	11.04	8.64	15.94	18.43	33.1	0.00	-23.5
Step 1000	28.33	11.09	8.64	16.02	18.59	33.1	0.00	-23.4

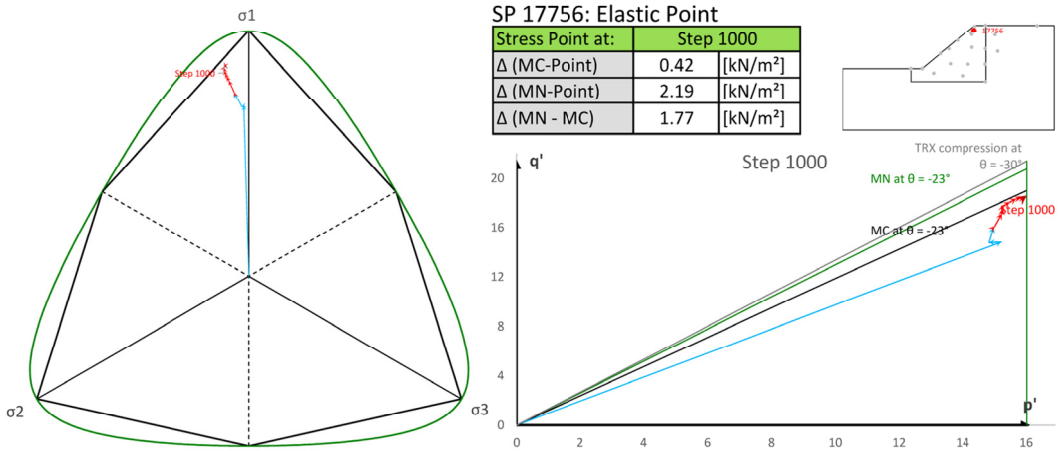

Fig. 99 MN-LE-M2: stress path of SP 17756

- **SP 22267**

Step	σ_1	σ_2	σ_3	p'	q'	φ'	c'	θ
	[kN/m²]	[kN/m²]	[kN/m²]	[kN/m²]	[kN/m²]	[°]	[kPa]	[°]
Step 5	0.43	0.16	0.11	0.23	0.30	37.3	0.00	-20.9
Step 8	1.03	0.38	0.25	0.55	0.72	37.3	0.00	-20.9
Step 11	2.93	1.10	0.72	1.58	2.05	37.3	0.00	-20.9
Step 1	3.01	1.13	0.74	1.63	2.10	37.3	0.00	-20.9
Step 127	1.97	0.74	0.49	1.07	1.37	37.3	0.00	-21.0
Step 253	2.43	0.91	0.61	1.32	1.69	37.3	0.00	-21.1
Step 379	2.70	1.01	0.67	1.46	1.88	37.3	0.00	-21.0
Step 505	2.54	0.95	0.63	1.38	1.77	37.3	0.00	-21.0
Step 631	2.66	1.00	0.66	1.44	1.85	37.3	0.00	-21.0
Step 754	2.37	0.89	0.59	1.28	1.65	37.3	0.00	-21.1
Step 877	2.83	1.06	0.70	1.53	1.97	37.3	0.00	-21.0
Step 1000	2.39	0.89	0.60	1.29	1.66	37.3	0.00	-21.0

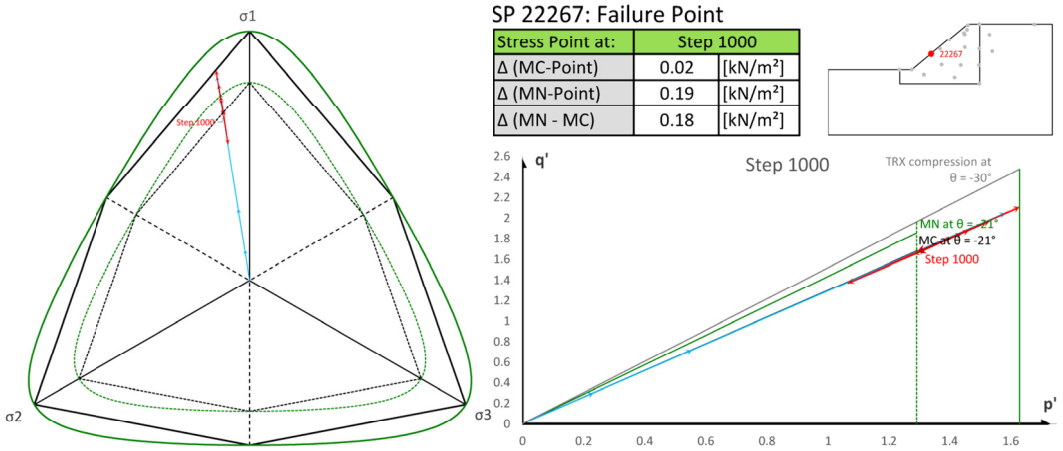

Fig. 100 MC-STD: stress path of SP 22267

Step	σ_1	σ_2	σ_3	p'	q'	φ'	c'	θ
	[kN/m²]	[kN/m²]	[kN/m²]	[kN/m²]	[kN/m²]	[°]	[kPa]	[°]
Step 4	35.08	13.11	8.61	18.93	24.54	37.3	0.00	-20.9
Step 11	21.19	7.92	5.20	11.44	14.82	37.3	0.00	-20.9
Step 26	2.87	1.07	0.70	1.55	2.01	37.3	0.00	-20.8
Step 1	2.87	1.07	0.71	1.55	2.00	37.3	0.00	-20.9
Step 127	2.19	0.82	0.55	1.19	1.53	37.3	0.00	-21.0
Step 253	1.84	0.69	0.46	1.00	1.29	37.3	0.00	-21.0
Step 379	2.26	0.85	0.56	1.22	1.57	37.3	0.00	-21.1
Step 505	2.29	0.86	0.57	1.24	1.60	37.3	0.00	-20.9
Step 631	2.32	0.87	0.57	1.25	1.62	37.3	0.00	-20.9
Step 754	2.32	0.87	0.58	1.26	1.62	37.3	0.00	-21.0
Step 877	2.34	0.88	0.58	1.27	1.63	37.3	0.00	-21.0
Step 1000	2.34	0.88	0.58	1.27	1.63	37.3	0.00	-21.0

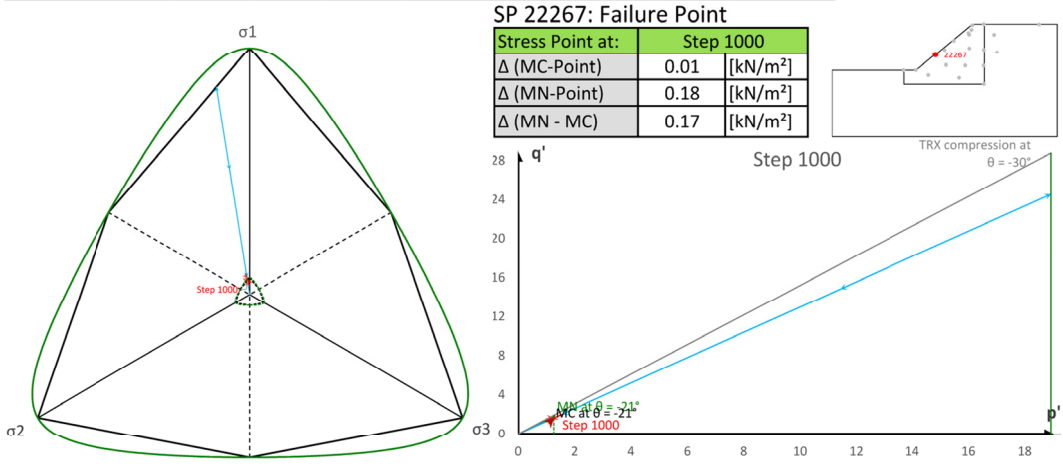

Fig. 101 MC-LE: stress path of SP 22267

Step	σ_1	σ_2	σ_3	p'	q'	φ'	c'	θ
	[kN/m²]	[kN/m²]	[kN/m²]	[kN/m²]	[kN/m²]	[°]	[kPa]	[°]
Step 5	36.94	17.37	6.85	20.39	26.45	37.3	0.00	-9.9
Step 8	21.62	15.10	4.42	13.71	15.04	37.3	0.00	8.0
Step 11	3.09	2.84	0.72	2.22	2.26	37.3	0.00	24.5
Step 1	2.99	2.74	0.70	2.14	2.17	37.3	0.00	24.2
Step 127	2.04	1.96	0.58	1.53	1.43	37.3	0.00	27.2
Step 253	2.33	1.80	0.61	1.58	1.53	37.3	0.00	12.6
Step 379	2.50	1.82	0.63	1.65	1.63	37.3	0.00	8.9
Step 505	2.46	1.81	0.64	1.64	1.59	37.3	0.00	9.4
Step 631	2.52	1.82	0.64	1.66	1.64	37.3	0.00	8.6
Step 754	2.39	1.78	0.62	1.60	1.56	37.3	0.00	10.0
Step 877	2.53	1.84	0.65	1.67	1.65	37.3	0.00	8.9
Step 1000	2.42	1.79	0.63	1.61	1.58	37.3	0.00	9.7

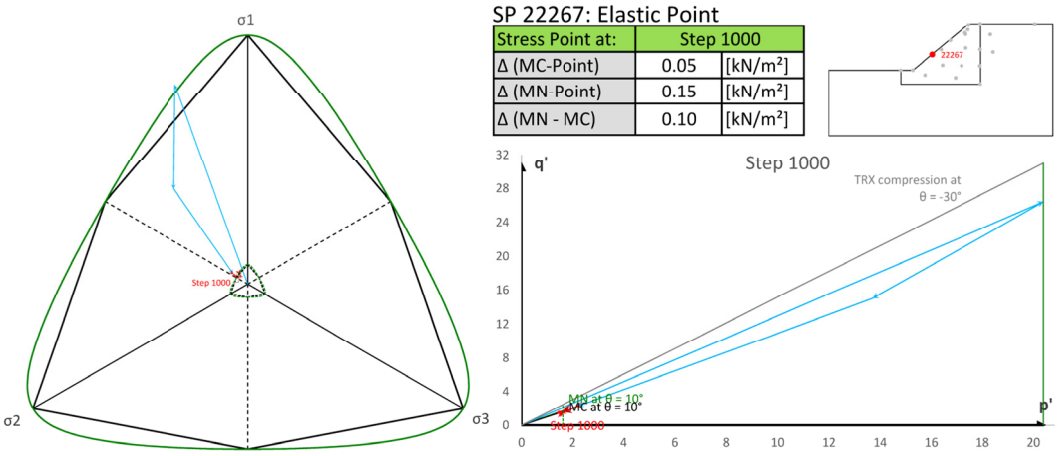

Fig. 102 MN-LE-M1: stress path of SP 22267

Step	σ_1	σ_2	σ_3	p'	q'	φ'	c'	θ
	[kN/m²]	[kN/m²]	[kN/m²]	[kN/m²]	[kN/m²]	[°]	[kPa]	[°]
Step 3	35.54	17.95	8.20	20.56	24.00	33.1	0.00	-9.4
Step 11	15.49	12.35	4.03	10.62	10.25	33.1	0.00	14.6
Step 25	2.34	2.02	0.64	1.67	1.57	33.1	0.00	20.0
Step 1	2.15	1.80	0.58	1.51	1.43	33.1	0.00	17.7
Step 127	2.32	1.81	0.62	1.58	1.52	33.1	0.00	13.0
Step 253	2.30	1.80	0.61	1.57	1.50	33.1	0.00	13.3
Step 379	2.31	1.80	0.61	1.57	1.51	33.1	0.00	12.9
Step 505	2.36	1.81	0.61	1.60	1.55	33.1	0.00	12.2
Step 631	2.40	1.79	0.63	1.61	1.56	33.1	0.00	10.3
Step 754	2.40	1.79	0.63	1.61	1.56	33.1	0.00	10.3
Step 877	2.51	1.80	0.64	1.65	1.64	33.1	0.00	8.1
Step 1000	2.64	1.87	0.66	1.72	1.73	33.1	0.00	7.4

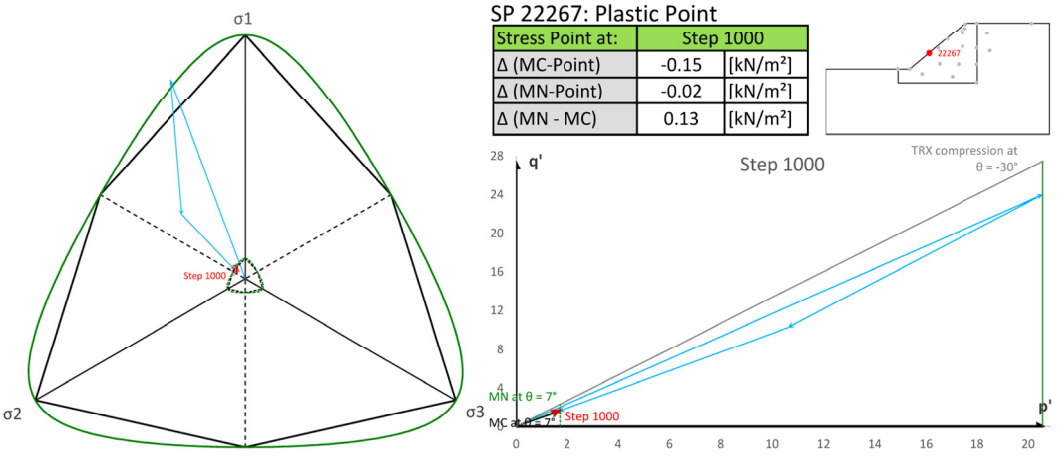

Fig. 103 MN-LE-M1: stress path of SP 22267

- **Comparison of the lode angle**

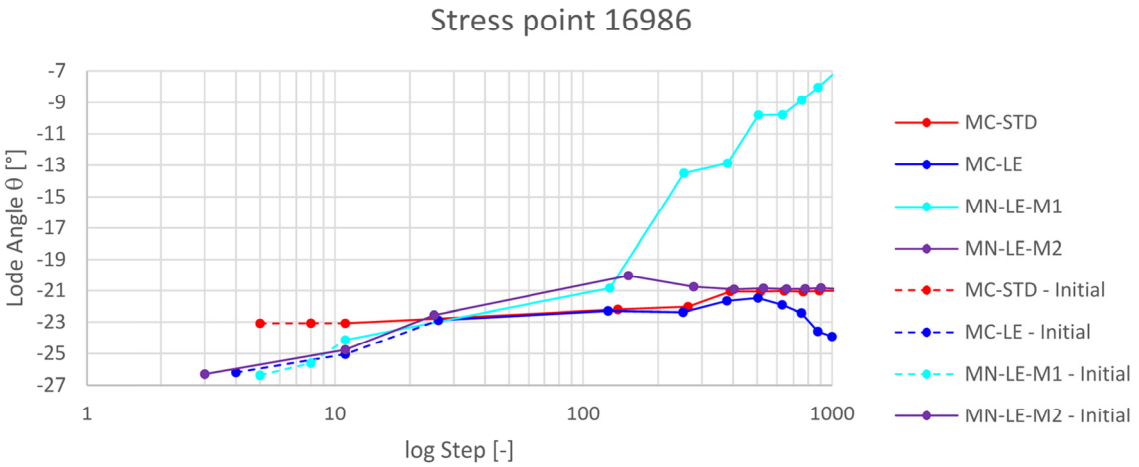

Fig. 104 SP 16986 - lode angle over steps in logarithmic scale

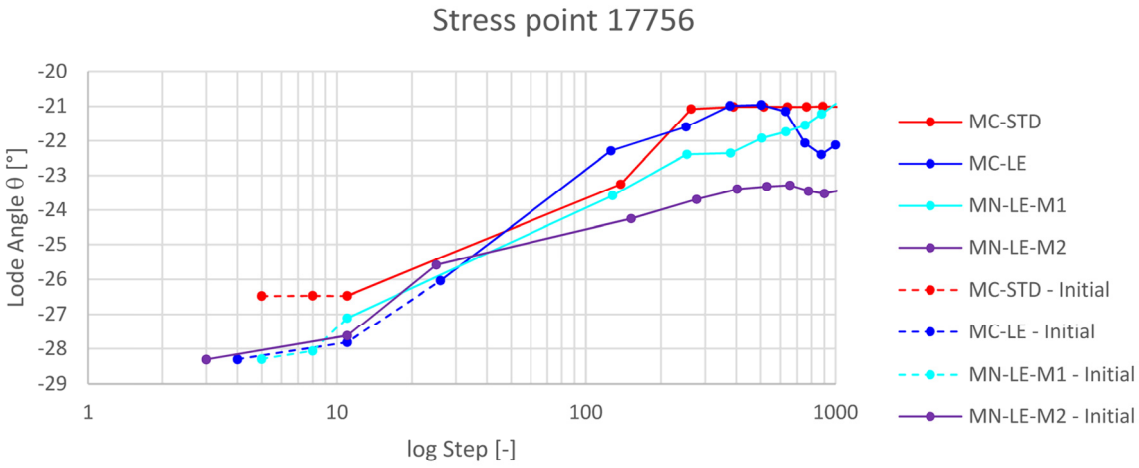

Fig. 105 SP 17756 - lode angle over steps in logarithmic scale

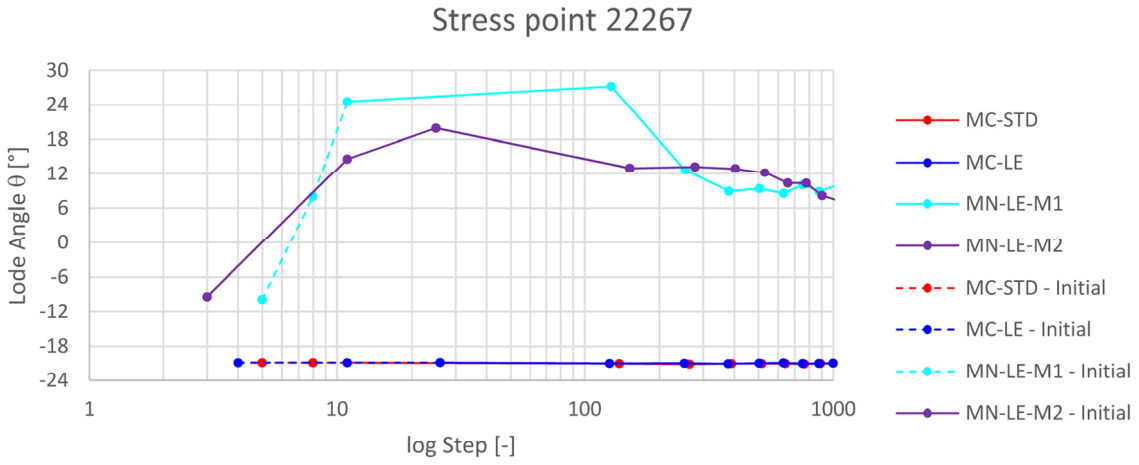

Fig. 106 SP 22267 - lode angle over steps in logarithmic scale

Appendix I

- **SP 7406**

Step	σ_1	σ_2	σ_3	p'	q'	φ'	c'	θ
	[kN/m²]	[kN/m²]	[kN/m²]	[kN/m²]	[kN/m²]	[°]	[kPa]	[°]
Step 3	11.87	5.18	5.12	7.39	6.73	12.1	5.06	-29.5
Step 7	66.37	37.84	35.17	46.46	29.95	12.1	5.06	-25.6
Step 14	102.45	58.74	58.74	73.31	43.71	12.1	5.06	-30.0
Step 1	101.48	60.52	59.19	73.73	41.64	12.1	5.06	-28.4
Step 127	111.44	65.43	64.55	80.47	46.46	12.1	5.06	-29.1
Step 253	82.43	51.05	45.61	59.70	34.42	12.1	5.06	-22.1
Step 379	82.45	51.06	45.62	59.71	34.43	12.1	5.06	-22.1
Step 505	82.42	51.10	45.61	59.71	34.40	12.1	5.06	-22.0
Step 631	82.42	51.17	45.61	59.73	34.37	12.1	5.06	-21.9
Step 754	82.39	51.22	45.58	59.73	34.34	12.1	5.06	-21.8
Step 877	82.44	51.32	45.62	59.80	34.32	12.1	5.06	-21.7
Step 1000	82.35	51.34	45.56	59.75	34.27	12.1	5.06	-21.6

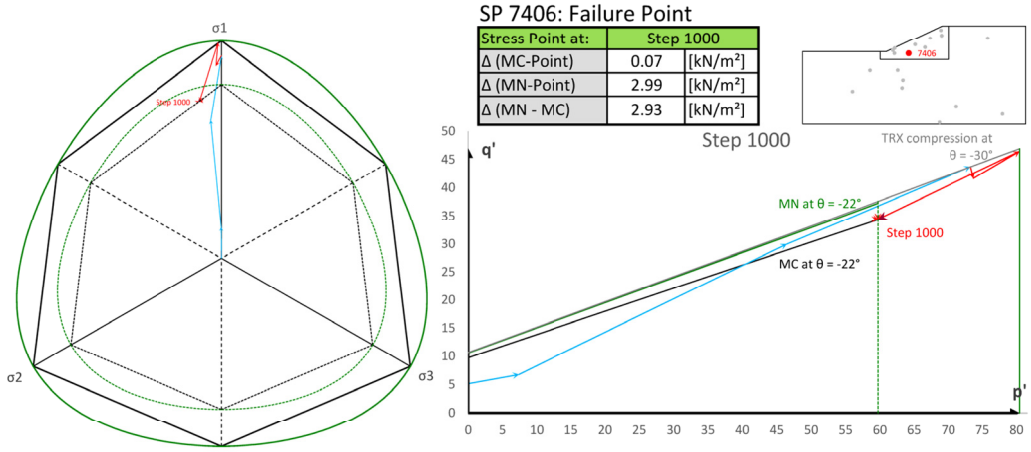

Fig. 107 MC-STD: stress path of SP 7406

Step	σ_1	σ_2	σ_3	p'	q'	φ'	c'	θ
	[kN/m²]	[kN/m²]	[kN/m²]	[kN/m²]	[kN/m²]	[°]	[kPa]	[°]
Step 3	84.24	50.91	50.06	61.74	33.76	10.7	4.45	-28.76
Step 7	93.21	58.55	54.97	68.91	36.58	10.7	4.45	-25.14
Step 14	101.66	70.02	57.88	76.52	39.15	10.7	4.45	-14.41
Step 1	102.15	75.41	57.69	78.42	38.77	10.7	4.45	-6.68
Step 127	99.91	81.85	56.87	79.55	37.44	10.7	4.45	5.31
Step 253	102.62	84.15	58.59	81.79	38.30	10.7	4.45	5.31
Step 379	102.95	84.40	58.73	82.02	38.46	10.7	4.45	5.31
Step 505	102.04	83.73	58.28	81.35	38.06	10.7	4.45	5.39
Step 631	102.45	83.99	58.46	81.64	38.26	10.7	4.45	5.29
Step 754	102.03	83.64	58.18	81.29	38.14	10.7	4.45	5.31
Step 877	101.86	83.49	58.09	81.15	38.07	10.7	4.45	5.30
Step 1000	102.31	83.88	58.37	81.52	38.22	10.7	4.45	5.31

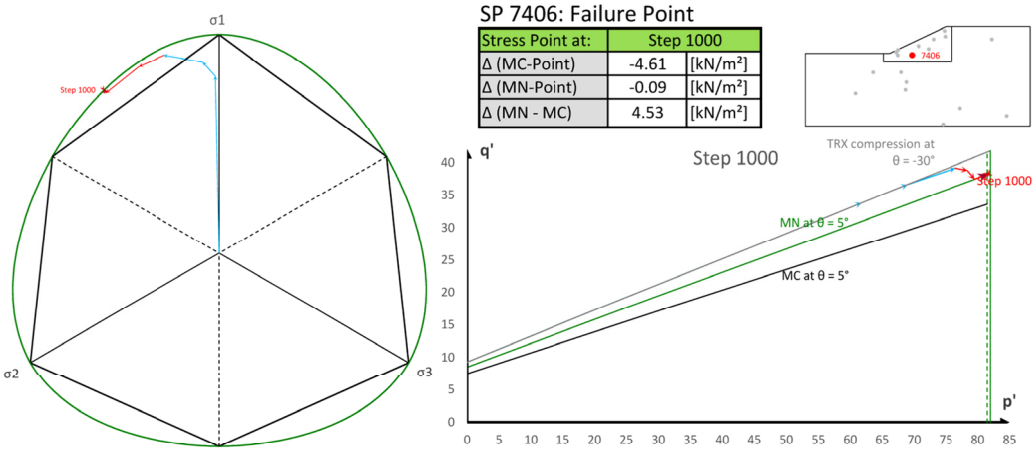

Fig. 108 MN-LE: stress path of SP 7406

- **SP 8866**

Step	σ_1	σ_2	σ_3	p'	q'	φ'	c'	θ
	[kN/m²]	[kN/m²]	[kN/m²]	[kN/m²]	[kN/m²]	[°]	[kPa]	[°]
Step 3	13.12	5.42	4.94	7.82	7.95	12.1	5.06	-27.0
Step 7	69.68	37.33	37.33	48.11	32.34	12.1	5.06	-30.0
Step 14	105.12	60.48	60.48	75.36	44.64	12.1	5.06	0.0
Step 1	103.51	61.99	60.53	75.34	42.26	12.1	5.06	-28.3
Step 127	172.56	104.63	104.44	127.21	68.02	12.1	5.06	-29.9
Step 253	172.55	104.63	104.44	127.21	68.02	12.1	5.06	-29.9
Step 379	172.56	104.64	104.44	127.21	68.02	12.1	5.06	-29.9
Step 505	172.57	104.69	104.45	127.23	68.01	12.1	5.06	-29.8
Step 631	172.51	104.71	104.41	127.21	67.95	12.1	5.06	-29.8
Step 754	172.53	104.78	104.41	127.24	67.93	12.1	5.06	-29.7
Step 877	172.57	104.88	104.46	127.30	67.91	12.1	5.06	-29.7
Step 1000	172.46	104.89	104.38	127.25	67.83	12.1	5.06	-29.6

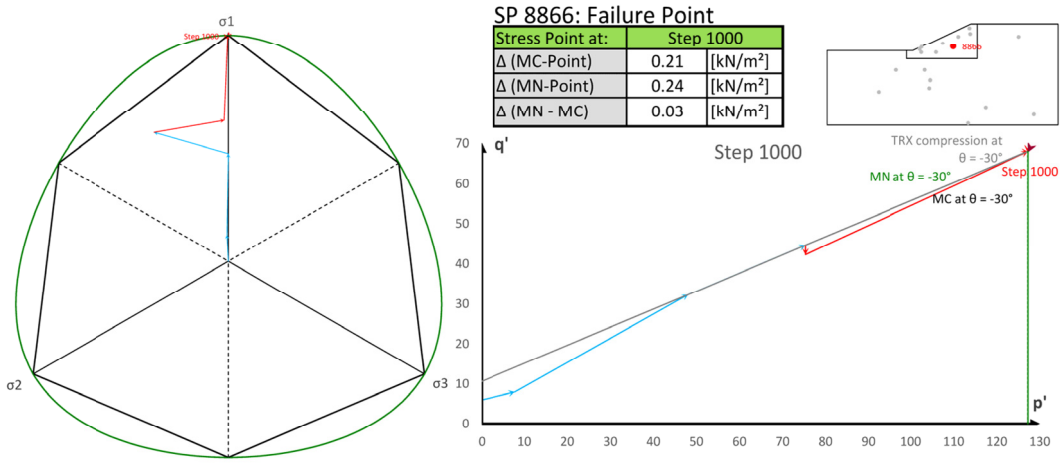

Fig. 109 MC-STD: stress path of SP 8866

Step	σ_1	σ_2	σ_3	p'	q'	φ'	c'	θ
	[kN/m²]	[kN/m²]	[kN/m²]	[kN/m²]	[kN/m²]	[°]	[kPa]	[°]
Step 3	89.27	55.66	52.44	65.79	35.33	10.7	4.45	-25.47
Step 7	96.05	63.20	55.32	71.52	37.42	10.7	4.45	-19.49
Step 14	101.97	71.90	57.86	77.24	39.04	10.7	4.45	-11.85
Step 1	102.40	75.96	58.06	78.81	38.64	10.7	4.45	-6.34
Step 127	102.92	84.42	58.83	82.05	38.35	10.7	4.45	5.31
Step 253	104.18	85.47	59.60	83.08	38.77	10.7	4.45	5.30
Step 379	105.21	86.32	60.20	83.91	39.15	10.7	4.45	5.30
Step 505	105.70	86.82	60.66	84.39	39.18	10.7	4.45	5.32
Step 631	105.52	86.61	60.46	84.20	39.19	10.7	4.45	5.29
Step 754	105.28	86.40	60.29	83.99	39.12	10.7	4.45	5.31
Step 877	106.31	87.26	60.98	84.85	39.42	10.7	4.45	5.26
Step 1000	105.98	87.01	60.76	84.59	39.33	10.7	4.45	5.31

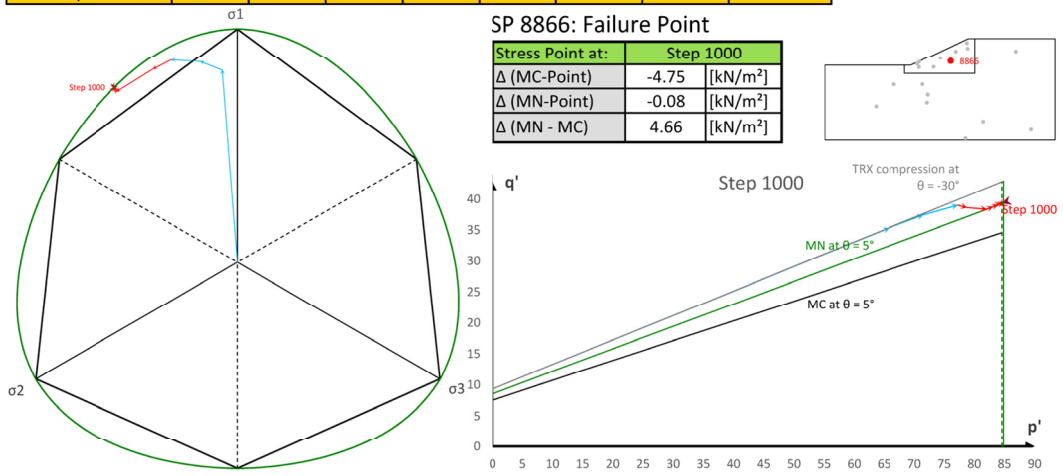

Fig. 110 MN-LE: stress path of SP 8866

Appendix J

Tab. 23 Input parameters of corresponding constitutive models

Parameter	Symbol	Value	Unit
Applied to MC			
Young´s modulus	E'	1.00E+06	[kN/m²]
Oedometer modulus	E_{oed}	1.61E+06	[kN/m²]
Shear modulus	G	3.70E+05	[kN/m²]
Applied to MN			
Reference un- / reloading stiffness	E_{ur}^{ref}	2.22E+06	[kN/m²]
Reference secant stiffness in triaxial test	E_{50}^{ref}	7.40E+05	[kN/m²]
Power for stress-level dependency of stiffness	m	0.5	[-]
Reference stress for stiffness	p_{ref}	100	[kN/m²]
Failure ratio	R_f	0.9	[-]
Tensile strength	σ_t	0	[kN/m²]
Ratio of shear moduli	G_0/G_{ur}	1	[-]
Threshold shear strain	$\gamma_{0.7}$	1.50E-04	[-]
Skempton coefficient	B	0.98	[-]
Model Switch	Model SW	2	[-]

Parameter	Symbol	Value	Unit
Applied to HS			
Reference secant stiffness in triaxial test	E_{50}^{ref}	7.40E+05	[kN/m²]
Reference tangent stiffness for primary oedometer loading	E_{oed}^{ref}	7.40E+05	[kN/m²]
Reference un- / reloading stiffness	E_{ur}^{ref}	2.22E+06	[kN/m²]
Power for stress-level dependency of stiffness	m	0.5	[-]
Reference stress for stiffness	p_{ref}	100	[kN/m²]
Failure ratio	R_f	0.9	[-]
Tensile strength	σ_t	0	[kN/m²]
Poisson´s ratio for un- / reloading	ν_{ur}	0.2	[-]
Coefficient of lateral earth pressure for normally consolidated stress state	K_0^{nc}	$1-\sin\varphi'$	[-]
Applied to HSS			
Reference secant stiffness in triaxial test	E_{50}^{ref}	7.40E+05	[kN/m²]
Reference tangent stiffness for primary oedometer loading	E_{oed}^{ref}	7.40E+05	[kN/m²]
Reference un- / reloading stiffness	E_{ur}^{ref}	2.22E+06	[kN/m²]
Power for stress-level dependency of stiffness	m	0.5	[-]
Threshold shear strain	$\gamma_{0.7}$	1.50E-04	[-]
Reference shear modulus at very small strain	G_0^{ref}	2.78E+06	[kN/m²]
Reference stress for stiffness	p_{ref}	100	[kN/m²]
Failure ratio	R_f	0.9	[-]
Tensile strength	σ_t	0	[kN/m²]
Poisson´s ratio for un- / reloading	ν_{ur}	0.2	[-]
Coefficient of lateral earth pressure for normally consolidated stress state	K_0^{nc}	$1-\sin\varphi'$	[-]